Physics – Uspekhi **57** (8) 735 – 770 (2014)

REVIEWS OF TOPICAL PROBLEMS PACS numbers: 97.10.Ex, 97.10.Ld, 97.60.Jd

Atmospheres and radiating surfaces of neutron stars

A Y Potekhin

DOI: 10.3367/UFNe.0184.201408a.0793

Contents

Abstract. The early 21st century is witnessing a breakthrough in the study of the thermal radiation of neutron stars. Observations with modern space telescopes have provided a wealth of valuable information, which, when properly interpreted, can elucidate the physics of superdense matter in the interior of these stars. This interpretation is underlain by the theory of formation of the neutron star thermal spectra, which is in turn based on plasma physics and on the understanding of radiative processes in stellar photospheres. In this paper, the current status of the theory is reviewed, with particular emphasis on neutron stars with strong magnetic fields. In addition to the conventional deep (semi-infinite) atmospheres, radiative condensed surfaces of neutron stars and 'thin' (finite) atmospheres are considered.

A Y Potekhin Ioffe Physical-Technical Institute,
ul. Politekhnicheskaya 26, 194021 Saint Petersburg, Russian Federation
Tel./Fax +7 (812) 292 71 80. E-mail: palex@astro.ioffe.ru
Centre de Recherche Astrophysique de Lyon (CNRS, UMR 5574);
École Normale Supérieure de Lyon;
Université de Lyon, Université Lyon 1;
Observatoire de Lyon,
9 avenue Charles André, 69230 Saint-Genis-Laval, France;
Central Astronomical Observatory of RAS at Pulkovo,
Pulkovskoe shosse 65, 196140 Saint Petersburg, Russian Federation

Received 19 September 2013, revised 10 November 2013
Uspekhi Fizicheskikh Nauk **184** (8) 793 – 832 (2014)
DOI: 10.3367/UFNr.0184.201408a.0793
Translated by A Y Potekhin; edited by A M Semikhatov

1. Introduction

Neutron stars are the most compact of all stars ever observed: with a typical mass $M \sim (1-2)\,M_\odot$, where $M_\odot = 2 \times 10^{33}$ g is the solar mass, their radius is $R \approx 10-13$ km. The mean density of such a star is $\sim 10^{15}$ g cm^{-3}, i.e., a few times the typical density of a heavy atomic nucleus $\rho_0 = 2.8 \times 10^{14}$ g cm^{-3}. The density at the neutron star center can exceed ρ_0 by an order of magnitude. Such matter cannot be obtained in laboratory, and its properties remain to be clarified. Even its composition is not completely known, because neutron stars, despite their name, consist not only of neutrons. There are a variety of theoretical models to describe neutron-star matter (see [1] and the references therein), and a choice in favor of one of them requires an analysis and interpretation of relevant observational data. Therefore, observational manifestations of neutron stars can be used for verification of theoretical models of matter under extreme conditions [2]. Conversely, the progress in studying

the extreme conditions of matter provides prerequisites for constructing neutron-star models and a proper interpretation of their observations. A more general review of these problems is given in [3]. In this paper, we focus on one of them, the formation of the thermal electromagnetic radiation of neutron stars.

Neutron stars are divided into accreting and isolated ones. The former accrete matter from outside, while accretion onto the latter is negligible. There are also transiently accreting neutron stars (X-ray transients), whose active periods (with accretion) alternate with quiescent periods, during which the accretion almost stops. The bulk of radiation from accreting neutron stars is due to the matter being accreted, which forms a circumstellar disk, accretion flows, and a hot boundary layer on the surface. By contrast, a significant part of the radiation from isolated neutron stars, as well as from transients in quiescence, appears to originate on the surface or in the atmosphere. To interpret this radiation, it is important to know the properties of the envelopes that contribute to the spectrum formation. On the other hand, a comparison of theoretical predictions with observations can be used to deduce these properties and to verify theoretical models of the dense magnetized plasmas that constitute the envelopes.

We consider the outermost envelopes of the neutron stars — their atmospheres. A stellar atmosphere is the plasma layer in which the electromagnetic spectrum is formed and from which the radiation escapes into space without significant losses. The spectrum contains valuable information on the chemical composition and temperature of the surface, the intensity and geometry of the magnetic field, and the stellar mass and radius.

In most cases, the density in the atmosphere grows with the depth gradually, without a jump, but stars with a very low temperature or a superstrong magnetic field can have a solid or liquid surface. The formation of the spectrum in the presence of such a surface is also discussed in this paper.

2. Basic characteristics of neutron stars

2.1 Masses and radii

The relation between the mass M and the radius R of a star is given by a solution of the hydrostatic equilibrium equation for a given equation of state (EOS), that is, the dependence of the pressure P on the density ρ and the temperature T, along with the thermal balance equation. The pressure in neutron star interiors is mainly produced by highly degenerate fermions with a Fermi energy $\epsilon_F \gg k_B T$ (k_B is the Boltzmann constant); therefore, we can neglect the T-dependence in calculations of $R(M)$. For the central regions of typical neutron stars, where $\rho \gtrsim \rho_0$, the EOS and even the composition of matter are not well known because of the lack of a precise relativistic many-body theory of strongly interacting particles. Instead of an exact theory, there exist many approximate models, which give a range of theoretical EOSs and, accordingly, $R(M)$ relations (see, e.g., Ch. 6 of [1]).

For a star to be hydrostatically stable, the density at the stellar center has to increase with increasing the mass M. This condition is satisfied in a certain interval $M_{\min} < M < M_{\max}$. The minimum neutron star mass is established rather well, $M_{\min} \approx 0.1\,M_\odot$ [4]. The maximum mass until recently was allowed to lie in a wide range $(1.5-2.5)\,M_\odot$ by competing theories (see, e.g., Table 6.1 in Ref. [1]), but the discoveries of neutron stars with masses $M = 1.97 \pm 0.04\,M_\odot$ [5] and $M = 2.01 \pm 0.04\,M_\odot$ [6] showed that $M_{\max} \gtrsim 2\,M_\odot$.

Simulations of the formation of neutron stars [7, 8] show that M typically exceeds $M_\odot$, the most typical values being in the range $(1.2-1.6)\,M_\odot$. Observations generally agree with these conclusions. The masses of several pulsars in double compact-star systems are known with a high accuracy (1%) due to measurements of the General Relativity (GR) effects on their orbital parameters. All of them lie in the interval from $1.3\,M_\odot$ to $2.0\,M_\odot$ [5, 6, 9]. The masses of other neutron stars that have been measured with an accuracy better than 10% cover the range $M_\odot \lesssim M \lesssim 2\,M_\odot$ [1, 10].

If the radius R and the mass M were known precisely for at least one neutron star, this would probably allow selecting one of the nuclear matter EOSs as the most realistic one. However, the current accuracy of measurements of neutron star radii leaves much to be desired.

2.2 Magnetic fields

Most of the known neutron stars have strong magnetic fields, unattainable in terrestrial laboratories. Gnedin and Sunyaev [11] pointed out that the spectra of such stars can contain a resonant electron cyclotron line. Its detection allows obtaining the magnetic field B by measuring the cyclotron frequency $\omega_c = eB/(m_e c)$, where m_e and $(-e)$ are the electron mass and charge, and c is the speed of light in the vacuum (here and hereafter, we use the Gaussian system of units). The discovery of a cyclotron line in the spectrum of the X-ray pulsar in the binary system Hercules X-1 [12] gave a striking confirmation of this idea. About 20 accreting X-ray pulsars are currently known to reveal an electron cyclotron line and sometimes several of its harmonics at energies of tens of keV, corresponding to $B \approx (1-4) \times 10^{12}$ G (see, e.g., [13–16]).

An alternative interpretation of the observed lines was suggested in [17]. It assumes an anisotropic distribution of electron velocities in a collisionless shock wave with a large Lorentz factor (the ratio of the total electron energy to $m_e c^2 = 511$ keV), $\gamma_r \approx 40$. The radiation frequency of such electrons strongly increases because of the relativistic Doppler effect, which allows explaining the observed position of the line by a much weaker field than in the conventional interpretation. It was noted in Ref. [18] that the small width of the lines (from one to several keV [13]) is difficult to accommodate in this model. It also leaves unexplained why the position of the line is usually almost constant. For example, the measured cyclotron energy of the accreting X-ray pulsar A 0535+26 remains virtually constant, while its luminosity changes by two orders of magnitude [19].

On the other hand, most X-ray pulsars do exhibit a dependence, albeit a weak one, of the observed line frequency on luminosity [20]. To explain this dependence, a model was suggested in [21], assuming that the cyclotron lines are formed by reflection from the stellar surface, irradiated by the accretion column. When luminosity increases, the bulk of reflection occurs at lower magnetic latitudes, where the field is weaker than at a pole, and therefore the cyclotron frequency decreases. This model, however, does not explain cases where the observed frequency increases with luminosity and, as noted in [22], it does not reproduce X-ray pulses at large luminosities.

A quantitative description of all observed dependences of the cyclotron frequency on luminosity is developed in Ref. [20], based on a physical model of cyclotron-line formation in an accretion column. The height of the region

above the surface, where the lines are formed, $h \sim (10^{-3}-10^{-1})\,R$, correlates with the luminosity, the correlation being positive or negative depending on the luminosity value. The line is centered at the frequency $\omega_c/(1+h/R)^3$, where ω_c is the cyclotron frequency at the base of the accretion column. In [22], variations of the polar cap diameter and the beam pattern were additionally taken into account, which has allowed explaining variations in the width and depth of the observed lines, in addition to their frequencies.

When cyclotron features are not identified in the spectrum, we have to resort to indirect estimates of the magnetic field. For isolated pulsars, the most widely used estimate is based on the expression

$$B \approx 3.2\times 10^{19}\, C\,\sqrt{\mathcal{P}\dot{\mathcal{P}}}\ \text{G}\,, \tag{1}$$

where $\mathcal{P}$ is the period in seconds, $\dot{\mathcal{P}}$ is its time derivative, and C is a coefficient that depends on stellar parameters. For a rotating magnetic dipole in the vacuum [23], $C = R_6^{-3}\,(\sin\alpha)^{-1}\sqrt{I_{45}}$, where $R_6 \equiv R/(10^6\ \text{cm})$, I_{45} is the moment of inertia in units of 10^{45} g cm^2, and α is the angle between the magnetic and rotational axes. In this case, Eqn (1) gives the magnetic field strength at the equator. If $M \approx (1-2)\,M_\odot$, then $R_6 \approx 1.0-1.3$ and $I_{45} \approx 1-3$ (see [1]). For estimates, one usually sets $C = 1$ in Eqn (1) (e.g., [24]).

A real pulsar differs significantly from a rotating magnetic dipole because its magnetosphere is filled with the plasma carrying electric charges and currents (see reviews [25–28] and recent papers [29–31]). According to the model by Beskin et al. [32, 33], the magnetodipole radiation is absent beyond the magnetosphere, while the slowdown of rotation is due to the current energy losses. However, the relation between B and $\mathcal{P}\dot{\mathcal{P}}$ remains similar. The results of numerical simulations of plasma behavior in the pulsar magnetosphere can be approximately described by Eqn (1) with $C \approx 0.8 R_6^{-3}\,(1+\sin^2\alpha)^{-1/2}\sqrt{I_{45}}$ [34]. As shown in [28], this result does not contradict the model in [32, 33].

The magnetic fields of ordinary radio pulsars are distributed near $B \sim 10^{12}$ G [35], 'recycled' millisecond pulsars have $B \sim (10^8-10^{10})$ G [35–37], and the fields of magnetars greatly exceed 10^{13} G [38, 39]. According to the most popular point of view, anomalous X-ray pulsars (AXPs) and soft gamma repeaters (SGRs) [38–42] are magnetars. For these objects, estimate (1) most often (although not always) gives $B \sim 10^{14}$ G, but in order to explain their energy balance, magnetic fields reaching $B \sim 10^{16}-10^{17}$ G in the core at the birth of the star are considered (see [43] and the references therein). Numerical calculations [44] show that magnetorotational instability in the envelope of a supernova, which is a progenitor of a neutron star, can give rise to nonstationary magnetic fields exceeding 10^{15} G. It is assumed that in addition to the poloidal magnetic field on the surface, magnetars can have a much stronger toroidal magnetic field embedded in deeper layers [45, 46]. Indeed, for a characteristic poloidal component $B_{\rm pol}$ of a neutron-star magnetic field to be stable, a toroidal component $B_{\rm tor}$ must be present such that, by the order of magnitude, $B_{\rm pol} \lesssim B_{\rm tor} \lesssim 10^{16}\ \text{G}\sqrt{B_{\rm pol}/(10^{13}\ \text{G})}$ [47]. Meanwhile, there is increasing evidence for the absence of a clear distinction between AXPs and SGRs [48], as well as between these objects and other neutron stars [41, 42, 49]. The paradoxical name 'low-field magnetar' has even appeared, applied to the AXPs and SGRs with $B \ll 10^{14}$ G (see, e.g., [50, 51] and the references therein).

For the majority of isolated neutron stars, the magnetic field estimate in (1) agrees with other data (e.g., with the observed properties of the bow shock nebula in the vicinity of a star [52]). But for AXPs and SGRs, we cannot exclude alternative models that do not involve superstrong fields but assume weak accretion on a young neutron star with $B \sim 10^{12}$ G from the circumstellar disk, which could remain after the supernova burst [53–56]. There is also a 'drift model', which suggests that the observed AXP and SGR periods are equal not to the rotation periods but to periods of drift waves, which affect the magnetic-line curvature and the direction of radiation in the outer parts of the magnetospheres of neutron stars with $B \sim 10^{12}$ G [57, 58]. Another model suggests that the AXPs and SGRs are not neutron stars at all, but rather massive ($M > M_\odot$), rapidly rotating white dwarfs with $B \sim 10^8-10^9$ G (see [59] and the references therein).

The measured neutron-star magnetic fields are enormous by terrestrial scales, but still far below the theoretical upper limit. An order-of-magnitude estimate of this limit can be obtained by equating the gravitational energy of the star to its electromagnetic energy [60]. For neutron stars, such an estimate gives the limit field $B_{\max} \sim 10^{18}-10^{19}$ G [61]. Numerical simulations of hydrostatic equilibrium of magnetized neutron stars show that $B_{\max} \lesssim 10^{18}$ G [65]. Still stronger magnetic fields imply such intense electric currents that their interaction would disrupt the star. We note in passing that the highest magnetic field that can be accommodated in quantum electrodynamics (QED) is, by the order of magnitude, $[m_e^2 c^3/(e\hbar)]\,\exp(\pi^{3/2}/\sqrt{\alpha_f}) \approx 10^{42}$ G [66], where $\alpha_f = e^2/(\hbar c) \approx 1/137$ is the fine structure constant and $\hbar$ is the Planck constant divided by 2π.

We see below that magnetic fields $B \gtrsim 10^{11}$ G strongly affect the most important characteristics of neutron-star envelopes. These effects are particularly pronounced on radiating surfaces and in atmospheres, which are the main subject of this review.

2.3 General relativity effects

The significance of GR effects for a star is quantified by the compactness parameter

$$x_g = \frac{r_g}{R}\,, \tag{2}$$

where

$$r_g = \frac{2GM}{c^2} \approx 2.95\,\frac{M}{M_\odot}\ \text{km} \tag{3}$$

is the Schwarzschild radius and G is the gravitational constant. The compactness parameter of a typical neutron star lies between 1/5 and 1/2, which is not small (for comparison, the Sun has $x_g = 4.24\times 10^{-6}$). Hence, the GR effects are not negligible. Two important consequences follow: first, the quantitative theory of neutron stars must be relativistic; second, observations of neutron stars open up a unique opportunity for measuring GR effects and verifying GR predictions.

In GR, the acceleration of gravity at the stellar surface is given by

$$g = \frac{GM}{R^2\sqrt{1-x_g}} = \frac{1.328\times 10^{14}}{\sqrt{1-x_g}}\,\frac{M/M_\odot}{R_6^2}\ \text{cm s}^{-2}\,. \tag{4}$$

Stellar hydrostatic equilibrium is governed by the Tolman–Oppenheimer–Volkoff equation (corrections due to the

rotation and magnetic fields are negligible for the majority of neutron stars):

$$\frac{\mathrm{d}P}{\mathrm{d}r} = -\left(1+\frac{P}{\rho c^2}\right)\left(1+\frac{4\pi r^3 P}{M_r c^2}\right)\left(1-\frac{2GM_r}{rc^2}\right)^{-1/2}, \quad (5)$$

where r is the radial coordinate measured from the stellar center and M_r is the mass inside a sphere of radius r.

The photon frequency, equal to ω in the local inertial reference frame, undergoes a redshift to a smaller frequency ω_∞ in the reference frame of a remote observer. Therefore, a thermal spectrum with an effective temperature $T_{\rm eff}$, when measured by a remote observer, corresponds to a lower effective temperature

$$T_{\rm eff}^\infty = \frac{T_{\rm eff}}{1+z_{\rm g}}, \quad (6)$$

where

$$z_{\rm g} \equiv \frac{\omega}{\omega_\infty} - 1 = (1-x_{\rm g})^{-1/2} - 1 \quad (7)$$

is the redshift parameter. Here and hereafter, the symbol ∞ indicates that the given quantity is measured at a large distance from the star and can differ from its value near the surface.

Along with the radius R, which is determined by the equatorial length $2\pi R$ in the local reference frame, the *apparent radius* for a remote observer is often defined as

$$R_\infty = R(1+z_{\rm g}). \quad (8)$$

With decreasing R, $z_{\rm g}$ increases, and therefore the apparent radius has a minimum, $\min R_\infty \approx 12-14$ km ([1], Ch. 6).

The apparent photon luminosity $L_{\rm ph}^\infty$ and the luminosity in the stellar reference frame $L_{\rm ph}$ are determined by the Stefan–Boltzmann law

$$L_{\rm ph}^\infty = 4\pi\sigma_{\rm SB} R_\infty^2 (T_{\rm eff}^\infty)^4, \quad L_{\rm ph} = 4\pi\sigma_{\rm SB} R^2 T_{\rm eff}^4, \quad (9)$$

with $\sigma_{\rm SB} = \pi^2 k_{\rm B}^4/(60\hbar^3 c^2)$. According to (6)–(8), these two quantities are related as

$$L_{\rm ph}^\infty = (1-x_{\rm g})\, L_{\rm ph} = \frac{L_{\rm ph}}{(1+z_{\rm g})^2}. \quad (10)$$

In the absence of perfect spherical symmetry, it is convenient to define the local effective surface temperature $T_{\rm s}$ by the relation

$$F_{\rm ph}(\theta,\varphi) = \sigma_{\rm SB} T_{\rm s}^4, \quad (11)$$

where $F_{\rm ph}$ is the local radial flux density at the surface point, determined by the polar angle (θ) and the azimuth (φ) in a spherical coordinate system. Then

$$L_{\rm ph} = \int_0^\pi \sin\theta\,\mathrm{d}\theta \int_0^{2\pi} \mathrm{d}\varphi F_{\rm ph}(\theta,\varphi). \quad (12)$$

The same relation connects the apparent luminosity $L_{\rm ph}^\infty$ (10) with the apparent flux $F_{\rm ph}^\infty = \sigma_{\rm SB}(T_{\rm s}^\infty)^4$ in a remote system, in accordance with the relation $T_{\rm s}^\infty = T_{\rm s}/(1+z_{\rm g})$, analogous to (6).

Expressions (6), (8), and (10) agree with the notion of light ray bending and time dilation near a massive body. If the angle between the wave vector $\mathbf{k}$ and the normal to the surface $\mathbf{n}$ at the emission point is θ_k, the observer receives a photon whose wave vector $\mathbf{k}'$ makes an angle $\theta > \theta_k$ with $\mathbf{n}$ (Fig. 1). The rigorous theory of the influence of light bending near a star on its observed spectrum has been developed in [67] and was reformulated in a convenient form in [68, 69]. The simple approximation [70]

$$\cos\theta_k = x_{\rm g} + (1-x_{\rm g})\cos\theta \quad (13)$$

is applicable at $x_{\rm g} < 0.5$ with an error within a few percent. For $\cos\theta_k < x_{\rm g}$, Eqn (13) gives $\theta > \pi/2$, as if the observer looked behind the neutron-star horizon. In particular, for a star with a dipole magnetic field and a sufficiently large inclination angle $\theta_{\rm m}$ of the dipole moment vector $\mathbf{m}$ to the line of site, the observer can see the two opposite magnetic poles at once. Clearly, such effects should be taken into

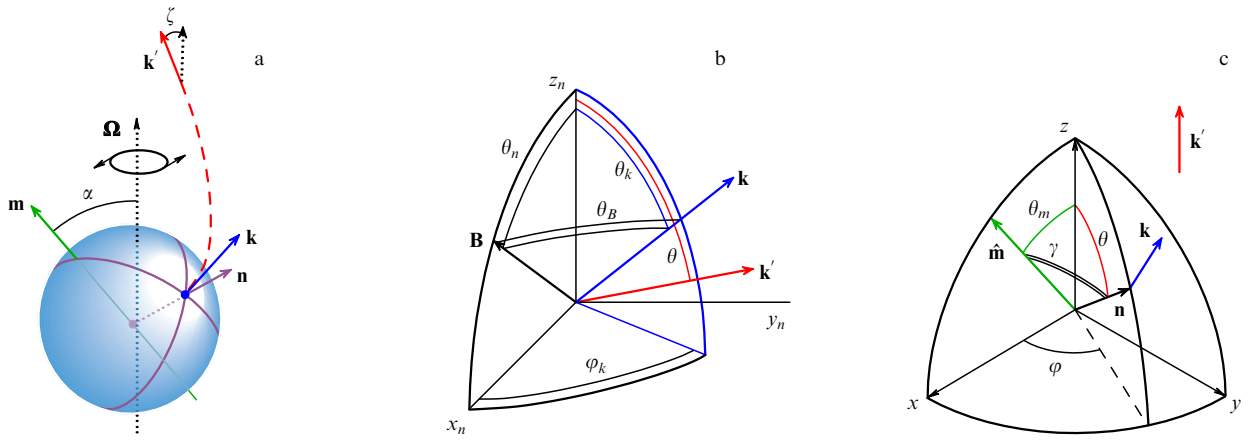

Figure 1. (Color online.) (a) Illustration of the gravitational light bending near a neutron star: $\mathbf{n}$ is the normal to the surface at a radiating point, $\mathbf{k}$ is the wave vector of an emitted ray in the local reference frame, and $\mathbf{k}'$ is the wave vector in the observer's reference frame. In addition, the stellar rotation vector $\mathbf{\Omega}$ and magnetic moment $\mathbf{m}$ are shown. The angles formed by the rotation axis with the magnetic moment (α) and with the line of sight (ζ) are indicated. (b) Wave vectors $\mathbf{k}$, $\mathbf{k}'$ and the magnetic field vector $\mathbf{B}$ in the local reference frame $(x_n y_n z_n)$ with the z axis along $\mathbf{n}$ and the x axis along the projection of $\mathbf{B}$ on the surface; θ_n is the angle between $\mathbf{B}$ and $\mathbf{n}$, θ_k and θ are the angles between the wave vectors and the normal, θ_B is the angle between the ray and the magnetic field, and φ_k is the azimuth. (c) Vectors $\mathbf{n}$, $\mathbf{k}$, $\mathbf{k}'$, and $\hat{\mathbf{m}} \equiv \mathbf{m}/|\mathbf{m}|$ in the coordinate system (xyz) with the z axis along the line of sight and the x axis along the projection of $\mathbf{m}$ on the picture plane; θ_m is the angle between $\mathbf{m}$ and the line of sight, γ is the angle between $\mathbf{n}$ and $\mathbf{m}$, and φ is the azimuth.

account when comparing theoretical neutron-star radiation models with observations.

Let I_ω be the specific intensity per unit circular frequency (if I_ν is the specific intensity per unit frequency, then $I_\omega = I_\nu/(2\pi)$; see [71]). The contribution to the observed radiation flux density from a small piece of the surface $\mathrm{d}\mathcal{A}$ in the circular frequency interval $[\omega, \omega + \mathrm{d}\omega]$ is [72, 73]

$$\mathrm{d}F^\infty_{\omega_\infty} = I_\omega(\mathbf{k})\,\cos\theta_k \left|\frac{\mathrm{d}\cos\theta_k}{\mathrm{d}\cos\theta}\right| \frac{\mathrm{d}\mathcal{A}}{D^2}\,(1-x_\mathrm{g})\,\mathrm{d}\omega\,, \qquad (14)$$

where $\mathrm{d}\omega = (1+z_\mathrm{g})\,\mathrm{d}\omega_\infty$. Here and hereafter, we assume that the rotational velocity of the patch $\mathrm{d}\mathcal{A}$ is much less than the speed of light. If this condition is not satisfied, the right-hand side of Eqn (14) should be multiplied by $(\cos\tilde{\theta}_k/\cos\theta_k)^4$, where $\tilde{\theta}_k$ is the angle between the surface normal and the wave vector in the reference frame comoving with the patch $\mathrm{d}\mathcal{A}$ at the moment of radiation [72, 73]. For a spherical star, Eqns (13) and (14) give

$$F^\infty_{\omega_\infty} = (1-x_\mathrm{g})^{3/2}\,\frac{R^2}{D^2}\int I_\omega(\mathbf{k};\theta,\varphi)\,\cos\theta_k\sin\theta\,\mathrm{d}\theta\,\mathrm{d}\varphi\,, \quad (15)$$

where the integration is restricted by the condition $\cos\theta_k > 0$.

The magnetic field is also distorted due to the spatial curvature in GR. For uniform and dipole fields, this distortion was described by Ginzburg and Ozernoi [74]. For a dipole field, the magnetic vector is

$$\mathbf{B} = B_\mathrm{p}\,(\mathbf{n}\,\hat{\mathbf{m}})\,\mathbf{n} + B_\mathrm{eq}\left[(\mathbf{n}\,\hat{\mathbf{m}})\,\mathbf{n} - \hat{\mathbf{m}}\right], \qquad (16)$$

where $\hat{\mathbf{m}} = \mathbf{m}/|\mathbf{m}|$ is the magnetic axis direction, B_eq and B_p are the equatorial and polar field strengths, and their ratio is equal to

$$\frac{B_\mathrm{eq}}{B_\mathrm{p}} = \frac{x_\mathrm{g}^2/2 - (1-x_\mathrm{g})\,\ln(1-x_\mathrm{g}) - x_\mathrm{g}}{[\ln(1-x_\mathrm{g}) + x_\mathrm{g} + x_\mathrm{g}^2/2]\,\sqrt{1-x_\mathrm{g}}}\,. \qquad (17)$$

In the limit of flat geometry ($x_\mathrm{g} \to 0$), $B_\mathrm{eq} \to B_\mathrm{p}/2$, but in general, $B_\mathrm{eq}/B_\mathrm{p} > 1/2 + x_\mathrm{g}/8$.

Muslimov and Tsygan [75] obtained expansions of the components of a poloidal magnetic field vector **B** with respect to the scalar spherical harmonics near a static neutron star beyond the dipole approximation. Equations (16) and (17) are a particular case of this expansion. Petri [76] developed a technique of expansion of electromagnetic fields around a rotating magnetized star with respect to vector spherical harmonics, which allows finding the solution of the Maxwell equations in GR for an arbitrary multipole component of the magnetic field. In this case, the solutions for a nonrotating star in GR [75] and for a rotating dipole in flat geometry [23] are reproduced as particular cases.

2.4 Measuring masses and radii by the thermal spectrum

Information on the mass and radius of a neutron star can be obtained from its thermal spectrum. We first consider the perfect blackbody radiation, whose spectrum is described by the Planck function [1]

$$\mathcal{B}_{\omega,T} = \frac{\hbar\omega^3}{4\pi^3 c^2}\,\frac{1}{\exp\left[\hbar\omega/(k_\mathrm{B}T)\right]-1}\,, \qquad (18)$$

[1] $\mathcal{B}_{\omega,T}$ is the specific intensity of nonpolarized blackbody radiation related to the circular frequency (see [71]).

and neglect interstellar absorption and the nonuniformity of the surface temperature distribution. The position of the spectral maximum $\hbar\omega_\mathrm{max} = 2.8k_\mathrm{B}T$ defines the effective temperature T^∞_eff, and the measured intensity gives the total flux density F_bol that reaches the observer. If the star is located at a distance D, its apparent photon luminosity is $L^\infty_\mathrm{ph} = 4\pi D^2 F_\mathrm{bol}$, and Eqn (9) yields R_∞.

In reality, a comparison of theoretical and measured spectra depends on a larger number of parameters. First, the spectrum is modified by absorption in the interstellar matter. The effect of the interstellar gas on the X-ray part of the spectrum is approximately described by the factor $\exp\left[-(N_\mathrm{H}/10^{21}\ \mathrm{cm}^{-2})\,(\hbar\omega/0.16\ \mathrm{keV})^{-8/3}\right]$, where N_H is the hydrogen column density on the line of sight [77]. Thus, we can find N_H from the analysis of the spectrum. If D is unknown, we can try to evaluate it assuming a typical interstellar gas density for the given galaxy region and using D as a fitting parameter.

Second, the temperature distribution can be nonuniform over the stellar surface. For example, in contrast to the cold poles of Earth, pulsars have heated regions near their magnetic poles, 'hot polar caps'. The polar caps of accreting neutron stars with strong magnetic fields are heated by matter flow from a companion star through the accretion disk and accretion column (see [78, 79] and the references therein). The polar caps of isolated pulsars and magnetars are heated by the current of charged particles created in the magnetosphere and accelerated by the electric field along the magnetic field lines (see reviews [25, 28, 80], papers [81, 82], and the references therein). The thermal spectrum of such neutron stars is sometimes represented as consisting of two components, one related to the heated region and the other to the rest of the surface, each with its own value of the effective temperature and effective apparent radius of the emitting area (see, e.g., [83]). Moreover, the variable strength and direction of the magnetic field over the surface affect the thermal conductivity of the envelope. Hence, the temperature T_s of a cooling neutron star outside the polar regions is also nonuniform (see, e.g., [84, 85]).

Finally, a star is not a perfect blackbody; therefore, its radiation spectrum differs from the Planck function. Spectral modeling is a complex task, which includes solving equations of hydrostatic equilibrium, energy balance, and radiative transfer (below, we consider it in more detail). Coefficients of these equations depend on the chemical composition of the atmosphere, the effective temperature, gravity, and the magnetic field. Different assumptions about the chemical composition, M, R, T_eff, and B values, and the distributions of T_s and **B** over the surface result in different model spectra. Comparing these spectra with the observed spectrum yields an evaluation of acceptable values of the parameters. With the known shape of the spectrum, we can calculate F_bol and evaluate R_∞ using Eqn (9). Identification of spectral features can provide z_g. A simultaneous evaluation of z_g and R_∞ allows calculating M from Eqns (2), (3), (7), and (8). This method of mass and radius evaluation requires a reliable theoretical description of the envelopes affecting the surface temperature and radiation spectrum.

2.5 Neutron-star envelopes

It is not only the superdense core of a neutron star but also the envelopes that are mostly under conditions unavailable in the laboratory. By terrestrial standards, they are characterized by superhigh pressures, densities, temperatures, and magnetic

fields. The envelopes differ by their composition, phase state, and role in the evolution and properties of the star.

In the deepest envelopes, just above the core of a neutron star, matter forms a neutron liquid with immersed atomic nuclei and electrons. In these layers, the neutrons and electrons are strongly degenerate, and the nuclei are neutron-rich, that is, their neutron number can be several times larger than the proton number, such that only the huge pressure keeps such nuclei together. Electrostatic interaction of the nuclei is so strong that they are arranged in a crystalline lattice, which forms the solid stellar crust. There can be a mantle between the crust and the core (although not all modern models of dense nuclear matter predict its existence). Atomic nuclei in the mantle take exotic shapes of extended cylinders or planes [86]. Such matter behaves like liquid crystals [87].

The neutron-star crust is divided into inner and outer parts. The outer crust is characterized by the absence of free neutrons. The boundary lies at the critical neutron-drip density $\rho_{\rm nd}$. According to current estimates [88], $\rho_{\rm nd} = 4.3 \times 10^{11}$ g cm^{-3}. With decreasing the ion density $n_{\rm i}$, their electrostatic interaction weakens, and finally a Coulomb liquid, instead of the crystal, becomes thermodynamically stable. The position of the melting boundary, which can be called the bottom of the neutron-star ocean, depends on the temperature and chemical composition of the envelope. If all the ions in the Coulomb liquid have the same charge Ze and mass $m_{\rm i} = Am_{\rm u}$, where $m_{\rm u} = 1.66 \times 10^{-24}$ g is the atomic mass unit, and if the magnetic field is not too strong, then the ion dynamics are determined only by the Coulomb coupling constant $\Gamma_{\rm Coul}$, which is the typical electrostatic-to-thermal energy ratio for the ions:

$$\Gamma_{\rm Coul} = \frac{(Ze)^2}{a_{\rm i} k_{\rm B} T} = \frac{22.75\, Z^2}{T_6} \left(\frac{\rho_6}{A}\right)^{1/3}, \qquad (19)$$

where $a_{\rm i} = (4\pi n_{\rm i}/3)^{-1/3}$, $T_6 \equiv T/(10^6\ {\rm K})$, and $\rho_6 \equiv \rho/(10^6\ {\rm g\ cm^{-3}})$. Given the strong degeneracy, the electrons are often considered as a uniform negatively charged background. In this model, the melting occurs at $\Gamma_{\rm Coul} = 175$ [89]. However, the ion–electron interaction and the quantizing magnetic field can shift the melting point by tens of percent [89, 90].

The strong gravity results in rapid separation of the chemical elements [91–95]. The results in Refs [93–95] can be combined to find that the characteristic sedimentation time for impurity ions with masses and charge numbers A' and Z' (that is, the time at which the ions pass the pressure scale height $P/(\rho g)$) in the neutron-star ocean is

$$t_{\rm sed} \approx \frac{46\, Z^{2.9} (Z')^{0.3} A^{-1.8}}{A' - AZ'/Z + \Delta_T + \Delta_{\rm C}} \frac{\rho_6^{1.3}}{g_{14}^2 T_6^{0.3}}\ {\rm days}, \qquad (20)$$

where $g_{14} \equiv g/(10^{14}\ {\rm cm\ s^{-2}}) \sim 1-3$, Δ_T is a thermal correction to the ideal degenerate plasma model [92, 94], and $\Delta_{\rm C}$ is an electrostatic (Coulomb) correction [94, 95]. The Coulomb correction $\Delta_{\rm C} \sim 10^{-3} - 10^{-2}$ dominates in strongly degenerate neutron-star envelopes (at $\rho \gtrsim 10^3$ g cm^{-3}), and at smaller densities $\Delta_T \gtrsim \Delta_{\rm C}$. Ions with larger A/Z ratios settle faster, while among ions with the same A/Z, the heavier ones settle down [92, 94, 95]. It follows from (20) that $t_{\rm sed}$ is small compared with the known neutron-star ages; therefore, neutron-star envelopes consist of chemically pure layers separated by transition bands of diffusive mixing.

Especially important is the thermal blanketing envelope that governs the flux density $F_{\rm ph}$ radiated by a cooling star with a given internal temperature $T_{\rm int}$. The density $F_{\rm ph}$ is mainly regulated by the thermal conductivity in the 'sensitivity strip' [96, 97], which plays the role of a 'bottleneck' for heat leakage. The position of this strip depends on the stellar parameters M, R, and $T_{\rm int}$, the magnetic field, and the chemical composition of the envelope. Because the heat transport across the magnetic field is hampered, the depth of the sensitivity strip can be different at different places on a star with a strong magnetic field: it lies deeper at those places where the magnetic field is more inclined to the surface [98]. As a rule, the sensitivity strip embraces the deepest layer of the ocean and the upper part of the crust and lies in the range $\rho \sim 10^5 - 10^9$ g cm^{-3}.

2.6 Atmosphere

With decreasing density, the ion electrostatic energy and the electron Fermi energy eventually become smaller than the kinetic ion energy. Then the degenerate Coulomb liquid gives way to a nondegenerate gas. The outer gaseous envelope of a star constitutes the atmosphere. In this paper, we consider models of quasistationary atmospheres. They describe stellar radiation only in the absence of intense accretion, since otherwise it is formed mainly by an accretion disk or by flows of infalling matter.

It is important that the sensitivity strip mentioned in Section 2.5 always lies at large optical depths. Hence, radiative transfer in the atmosphere barely affects the full thermal flux, and the spectrum can therefore be modeled with the $F_{\rm ph}$ and $T_{\rm s}$, determined from a simplified model of heat transport in the atmosphere. Usually, such a model is based on the Eddington approximation (see, e.g., [99]). Shibanov et al. [100] verified the high accuracy of this approximation for determining the full thermal flux from neutron stars with strong magnetic fields.

Atmospheres of ordinary stars are divided into the lower part, called the photosphere, where radiative transfer dominates, and the upper atmosphere, whose temperature is determined by processes other than the radiative transfer. The upper atmosphere of neutron stars is usually thought to be absent or negligible. Therefore, one does not discriminate between the notions of atmosphere and photosphere for neutron stars. In this respect, we note that vacuum polarization in superstrong magnetic fields (see Section 6.3) makes the magnetosphere birefringent, and hence the magnetosphere, being thermally decoupled from the radiation propagating from the star to the observer, can still affect this radiation. Thus, the magnetosphere can play the role of an upper atmosphere of a magnetar.

The geometric depth of the atmosphere is several millimeters in relatively cold neutron stars and centimeters in relatively hot ones. These scales can be easily obtained from a simple estimate: as is the case for ordinary stars, the typical depth of a neutron-star photosphere, by the order of magnitude, does not much exceed the barometric height scale, the latter being $k_{\rm B}T/(m_{\rm i}g) \approx (0.83/A)\,(T_6/g_{14})$ cm. The ratio of the photosphere depth to the neutron-star radius is only $\sim 10^{-6}$ (for comparison, for ordinary stars, this ratio is $\sim 10^{-3}$), which allows calculating local spectra with the surface curvature neglected.

The presence of atoms, molecules, and ions with bound states significantly changes the electromagnetic absorption coefficients in the atmosphere, thereby affecting the observed

spectra. A question arises as to whether the processes of particle creation and acceleration near the surface of pulsars allow a partially ionized atmosphere to exist. According to canonical pulsar models [24–26], the magnetosphere is divided into regions of open and closed field lines, the closed-line region being filled by charged particles, such that the electric field of the magnetosphere charge in the comoving (rotating) reference frame cancels the electric field arising from the rotation of the magnetized star. The photosphere that lies below this part of the magnetosphere is stationary and electroneutral.

By contrast, there is a strong electric field near the surface in the open-line region. This field accelerates the charged particles almost to the speed of light. It is not obvious that these processes do not affect the photosphere; therefore, quantitative estimates are needed. We define the column density

$$y_{\rm col} = \int_r^\infty (1+z_{\rm g})\,\rho(r)\,{\rm d}r\,, \tag{21}$$

where the factor $(1+z_{\rm g})$ takes the relativistic scale change in the gravitational field into account. According to [101], in the absence of a strong magnetic field, ultrarelativistic electrons lose their energy mostly to bremsstrahlung at the depth where $y_{\rm col}\sim 60$ g cm^{-2}. As noted in [102], such a column density is orders of magnitude larger than the typical density of a nonmagnetic neutron-star photosphere. Therefore, the effect of accelerated particles reduces to an additional deep heating.

The situation changes in a strong magnetic field. Electron oscillations driven by the electromagnetic wave are suppressed in the directions perpendicular to the magnetic field, which decreases the coefficients of electromagnetic wave absorption and scattering by the electrons and atoms (Section 6.5). As a result, the strong magnetic field 'clarifies' the plasma, that is, the same mean (Rosseland [103, 104]) optical depth $\tau_{\rm R}$ is reached at a larger density. For a typical neutron star with $B\gtrsim 10^{11}$ G, the condition $\tau_{\rm R}=3/2$ that is required in order to have $T(r)=T_{\rm eff}$ in the Eddington approximation is fulfilled at the density [105]

$$\rho \approx B_{12}\ \ {\rm g\,cm^{-3}}\,, \tag{22}$$

where $B_{12}\equiv B/(10^{12}$ G). Thus, the density of the layer where the spectrum is formed increases as B increases. At the same time, the main mechanism of electron and positron deceleration changes, which is related to Landau quantization (Section 5.1). In a strong magnetic field, the most effective deceleration mechanism is the magneto-Coulomb interaction, which makes any charged particles colliding with plasma ions jump to excited Landau levels with subsequent de-excitation through synchrotron radiation [106]. The magneto-Coulomb deceleration length is inversely proportional to B. The characteristic depth of the magneto-Coulomb deceleration of ultrarelativistic electrons in the neutron-star atmosphere can be estimated as [106]

$$y_{\rm col} \approx \left(\frac{\gamma_{\rm r}}{700}\,Z^2\,A^{-3}\,B_{12}^{-2}\right)^{0.43} T_6\ \ {\rm g\,cm^{-2}}\,, \tag{23}$$

where $\gamma_{\rm r}\sim 10^3-10^8$ is the Lorentz factor. We can easily see from (22) and (23) that at $B\gtrsim 3\times 10^{12}$ G, the electrons are decelerated by emitting high-energy photons in an optically thin layer. In this case, the magneto-Coulomb radiation constitutes a nonthermal supplement to the thermal photospheric spectrum of the polar cap.

In intermediate magnetic fields 10^{11} G $\lesssim B\lesssim 3\times 10^{12}$ G, the braking of accelerated particles occurs in the photosphere. Such polar caps require special photosphere models where the equations of ionization, energy, and radiative balance would take the braking of charged particles into account.

Photospheres can have different chemical compositions. Before the early 1990s, it was commonly believed that the outer layers of a neutron star consist of iron, because it is the most stable chemical element remaining after the supernova burst that gave birth to the neutron star [107]. Nevertheless, the outer envelopes of an isolated neutron star may contain hydrogen and helium because of accretion of interstellar matter [108, 109]. Even if the star is in the ejector regime [110], that is, its rotating magnetosphere throws out the infalling plasma, a small fraction of the plasma still leaks to the surface (see [78] and the references therein). Because of the rapid separation of ions in a strong gravitational field (Section 2.5), the accreted atmosphere can consist entirely of hydrogen. In the absence of a magnetic field, hydrogen completely fills the photosphere if its column density exceeds $y_{\rm col}\gtrsim 0.1$ g cm^{-2}. In the field $B\sim 10^{14}$ G, this happens at $y_{\rm col}\gtrsim 10^3$ g cm^{-2}. Even in that case, an accreting mass $\sim 10^{-17}M_\odot$ would suffice. But if the accretion occurred at the early stage of stellar life, when its surface temperature was higher than a few MK, hydrogen could diffuse into deeper and hotter regions, where it would be burnt in thermonuclear reactions [111], leaving helium on the surface [112]. The same might happen to helium [111], and then carbon would be left on the surface [94, 113]. In addition, a mechanism of spallation of heavy chemical elements into lighter ones operates in pulsars due to collisions of the accelerated particles in the open field line regions, which produces lithium, beryllium, and boron isotopes [114]. Therefore, only an analysis of observations can elucidate the chemical composition of the neutron star atmosphere.

A Coulomb liquid can turn into the gaseous phase abruptly. This possibility arises in the situation of a first-order phase transition between condensed matter and nondegenerate plasma (see Section 5.10). Then the gaseous layer may be optically thin, in which case a neutron star is called naked [115], because its spectrum is formed on a solid or liquid surface uncovered by an atmosphere.

Although many researchers have studied neutron-star atmospheres for dozens of years, many unsolved problems still persist, especially when strong magnetic fields and incomplete ionization are present. The state of the art of these studies is considered below.

3. Neutron stars with thermal spectra

In general, a neutron-star spectrum includes contributions caused by different processes in addition to the thermal emission: for example, processes in pulsar magnetospheres, pulsar nebulae, and accretion disks. A small part of such spectra allow separating the thermal component from the other contributions (see [116] for a review). Fortunately, their number is constantly increasing. We list their main classes.

3.1 X-ray transients

The X-ray binary systems where a neutron star accretes matter from a less massive star (a Main Sequence star or a white dwarf) are called low-mass X-ray binaries (LMXBs). In

some LMXBs, periods of intense accretion alternate with longer (usually months, and sometimes years) 'periods of quiescence', when accretion stops and the remaining X-ray radiation comes from the heated surface of the neutron star. During the last decade, such soft X-ray transients (SXTs) in quiescence (qLMXBs) were yielding an ever increasing amount of valuable information on neutron stars.

Compression of the crust under the weight of newly accreted matter results in deep crustal heating, driven by exothermic nuclear transformations [117, 118]. These transformations occur in a nonequilibrium layer, whose formation was first studied by Bisnovatyi-Kogan and Chechetkin [119]. In a review by the same authors [120], this problem is exposed in more detail with applications to different real objects. For a given theoretical model of a neutron star, one can calculate the heating curve [121], that is, the dependence of the equilibrium accretion-free effective temperature T_0 on the accretion rate averaged over a large preceding period of time. Comparing the heating curves with a measured T_0 value, one can draw conclusions on the parameters of a given neutron star and properties of its matter. From such an analysis, restrictions on the mass and composition of the core of the neutron star in SXT SAX J1808.4–3658 [121] have been obtained. In [122, 123], the possibility of constraining the critical temperatures of proton and neutron superfluidities in the stellar core was demonstrated. The prospects of applying such an analysis to various classes of X-ray transients are discussed in [124].

SXTs that have recently moved into the quiescence mode allow probing the state of the neutron-star crust by the decrease in $T_{\rm eff}$. It was suggested in [125] that during this decrease, radiation is fed by the heat that was deposited in the crust in the preceding active period. In 2001, SXT KS 1731–260, which was discovered in 1989 by Sunyaev's group [126], turned from the active state into quiescence [127]. Subsequent observations have provided the cooling rate of the surface of the neutron star in this SXT. In 2007, Shternin et al. [128] analyzed the 5-year cooling of KS 1731–260 and obtained constraints on the heat conductivity in the neutron-star crust. In particular, they showed that the hypothesis on an amorphous state of the crust [129] is incompatible with the observed cooling rate, which means that the crust has a regular crystalline structure.

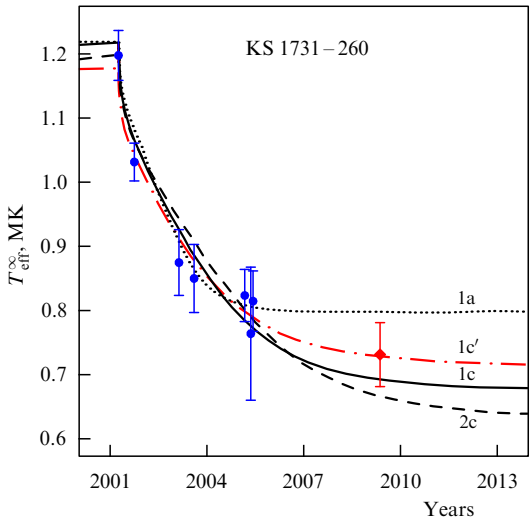

Figure 2. (Color online.) Theoretical cooling curves for different neutron-star models compared with observations of KS 1731–260. The observational data are from Table 1 in [131]. The blue dots correspond to the observations used in [128], and the red diamond is the new observation. The 1σ error bars are plotted. For the cooling curves, we use the numerical data and notation from Ref. [128]: 1a — $M = 1.6M_\odot$, $T_0 = 0.8$ MK, $E_{44} = 2.6$; 1c — $M = 1.6M_\odot$, $T_0 = 0.67$ MK, $E_{44} = 2.4$; 2c — $M = 1.4M_\odot$, $T_0 = 0.63$ MK, $E_{44} = 2.4$. Model 1a, unlike the other three models, assumes an accreted envelope and a moderate (in terms of [128]) neutron superfluidity in the crust. The curve marked 1c′ was not shown in [128]. It corresponds to $M = 1.65M_\odot$, $T_0 = 0.7$ MK, $E_{44} = 2$.

Figure 2 shows theoretical cooling curves compared to observations of KS 1731–260. The theoretical models differ in assumptions on the neutron-star mass, the composition of its heat-blanketing envelope, neutron superfluidity in the crust, the heat $E_{\rm tot}$ deposited in the crust in the preceding accretion period ($E_{44} \equiv E_{\rm tot}/10^{44}$ erg), and the effective equilibrium temperature T_0. Models 1a, 1c, and 2c were among others described and discussed in [128]. At that time, when only the first seven observations were available, it was believed that the thermal relaxation of the crust had completed, and $T_0 = 8 \times 10^5$ MK [130], which corresponds to curve 1a in Fig. 2. Shternin et al. [128] were the first to call this paradigm into question. They demonstrated that the available observations could be described by curves 1c ($T_0 = 6.7 \times 10^5$ K) and 2c ($T_0 = 6.3 \times 10^5$ K) as well. In 2009, new observations of KS 1731–260 were performed, which confirmed that the cooling continues [131]. The whole set of observations is best described by model 1c′ (the dotted-dashed line in Fig. 2), which only slightly differs from model 1c and assumes $T_0 = 7 \times 10^5$ MK.

In 2008, the cooling curve of SXT MXB 1659–29 was constructed for the crustal thermal relaxation stage, which had been observed for 6 years [132]. This curve generally agreed with the theory. In 2012, however, the spectrum suddenly changed, as if the temperature abruptly dropped [133]. Nonetheless, the spectral evolution driven by the cooling must have already reached an equilibrium. The observed change in the spectrum can be explained by a change in the line-of-sight hydrogen column density. The cause of this change remains unclear. Indications of variations of $N_{\rm H}$ were also found in the cooling of qLMXB EXO 0748–676 [134].

Several other qLMXBs have recently moved into quiescence and show signs of thermal relaxation of the neutron-star crust. A luminosity decline was even seen during a single 8-hour observation of SXT XTE J1709–267 after the end of the active phase of accretion [135]. Analyses of observations of some qLMXBs (XTE J1701–462 [136, 137], EXO 0748–676 [138]) confirm the conclusions in [128] on the crystalline structure of the crust and give additional information on the heating and composition of the crust of accreting neutron stars [135, 138, 139]. In Section 4.5, we discuss the interpretation of the observed qLMXB spectra that underlies this analysis.

Transiently accreting X-ray pulsars Aql X-1, SAX J1808.4–3658, and IGR J00291 + 5734 reveal similar properties, but the analysis of their spectral evolution is strongly impeded by the possible presence of a nonthermal component and hot polar caps (see [140, 141] and the references therein). Their X-ray luminosities in quiescence vary nonmonotonically, as do those of qLMXBs Cen X-4 [142] and EXO 1745–248 [143]. The thermal flux variations that do not conform to the thermal relaxation scenario may be caused by an accretion on the neutron star, which slows down but does not stop in quiescence [138, 141, 144].

3.2 Radio pulsars

There are several normal pulsars whose spectra clearly reveal a thermal component: they are the relatively young ($t_* \lesssim 10^5$ years of age) pulsars J1119–6127, B1706–44, and Vela, and the middle-aged ($t_* \sim 10^6$ years) pulsars B0656+14, B1055−52, and Geminga. The spectra of the last three objects, dubbed the Three Musketeers [145], are described by a three-component model, which includes a power-law spectrum of magnetospheric origin, a thermal spectrum of hot polar caps, and a thermal spectrum of the rest of the surface [116]. In most studies, the thermal components of pulsar spectra are interpreted with the blackbody model, and less often with a model of a fully ionized H atmosphere with a predefined surface gravity. We see in what follows that both are physically ungrounded. Only recently, in Ref. [146], was the X-ray radiation of PSR J1119–6127 interpreted using an H-atmosphere model taking the incomplete ionization into account. This result is described in Section 8.4.

A convenient characteristic of the slowdown of pulsar rotation is the loss rate of the rotational kinetic energy $\dot{E}_{\rm rot} = -I\Omega\dot{\Omega}$ of a standard rotor with the moment of inertia $I = 10^{45}$ g cm^2, typical of neutron stars, where $\Omega = 2\pi/\mathcal{P}$ is the angular frequency of rotation and $\dot{\Omega}$ is its time derivative (see [147]). As follows from observations, the spectra of millisecond pulsars with $\dot{E}_{\rm rot} > 10^{35}$ erg s^{-1} are mainly nonthermal. However, the millisecond pulsars PSR J0030+0451, J0437−4715, J1024–0719, and J2124–3358, with $\dot{E}_{\rm rot} \lesssim 10^{34}$ erg s^{-1}, show a thermal spectral component in the nonthermal background. In Section 4.6, we consider the interpretation of this thermal component based on photosphere models.

3.3 Bursters

Accreting neutron stars in close binary systems that produce X-ray bursts with intervals from hours to days are called bursters. The theory of bursters was formulated in [148] (see also review [149]).

During intervals between the bursts, a burster's atmosphere does not essentially differ from that of a cooling neutron star. In such periods, the bulk of the observed X-ray radiation arises from a transformation of the gravitational energy of the accreting matter into thermal energy. The matter, mostly consisting of hydrogen and helium, piles up on the surface and sooner or later (usually in several hours or days) reaches such densities and temperatures that a thermonuclear burst is triggered, which is observed from Earth as a type-I X-ray burst.[2] Some type-I bursts last over a minute and are called long X-ray bursts. They arise in periods when the accretion rate is not high, such that the luminosity $L_{\rm ph}$ before the burst does not exceed several percent of the Eddington limit $L_{\rm Edd}$ (see Section 4.2). In this case, the inner part of the accretion disk is a hot flow ($k_{\rm B}T \sim 20-30$ keV) of matter with the optical thickness about unity. It hardly affects or screens the burst [151]. As we see in Section 4.3, the observed spectrum of a burster, its evolution during a long burst, and the subsequent relaxation are successfully interpreted with nonmagnetic atmosphere models.

But if the accretion rate is higher, such that $L_{\rm ph} \gtrsim 0.1 L_{\rm Edd}$, the accretion disk is relatively cool and optically thick down to the neutron-star surface. In this case, the disk can strongly shield the burst and reprocess its radiation [152, 153], while a boundary spreading layer is formed on the surface. The theory of such a layer is developed in [154, 155]. The spreading layer spoils the spectrum such that its usual decomposition becomes ambiguous and has to be modified, as described in [156, 157].

3.4 Radio quiet neutron stars

The discovery of radio quiet[3] neutron stars, whose X-ray spectra are apparently purely thermal, has become an important milestone in astrophysics. Radio quiet neutron stars include central compact objects in supernova remnants (CCOs) [160, 161] and X-ray dim isolated neutron stars (XDINSs) [39, 40, 161–163].

Exactly seven XDINSs have been discovered since 2001, and they are dubbed the Magnificent Seven [39]. Observations have provided stringent upper limits ($\lesssim 0.1$ mJy) on their radio emission [164]. XDINSs have longer periods (> 3 s) than the majority of pulsars, and their magnetic field estimations by Eqn (1) typically give rather high values $B \sim (10^{13}-10^{14})$ G [40, 165]. It is possible that XDINSs are descendants of magnetars [40, 41, 163].

About ten CCOs are known to date [161, 166]. Pulsations have been found in the radiation of three of them. The periods of these pulsations are rather small (0.1 s to 0.42 s) and very stable. This indicates that CCOs have a relatively weak magnetic field $B \sim 10^{11}$ G, in contrast to XDINSs. For this reason they are sometimes called 'antimagnetars' [161, 166, 167]. The large amplitudes of the pulsations of some CCOs indicate a strongly nonuniform surface temperature distribution. To explain it, some authors have hypothesized that a superstrong magnetic field might be hidden in the neutron-star crust [168].

The X-ray source 1RXS J141256.0+792204, which was discovered in 2008 and dubbed Calvera, was initially considered as a possible eighth object with the properties of the Magnificent Seven [169]. However, subsequent observations suggested that its properties are closer to those of CCOs. In 2013, observations of Calvera from the *Chandra* orbital observatory provided the period derivative $\dot{\mathcal{P}}$ [170]. According to Eqn (1), its value corresponds to $B \approx 4.4 \times 10^{11}$ G. The authors of [170] characterize Calvera as an 'orphaned CCO' whose magnetic field is emerging through supernova debris. Calvera is also unique in that it is the only energetic pulsar that emits virtually no radio or gamma radiation, which places constraints on models of particle acceleration in magnetospheres [170].

3.5 Neutron stars with absorption lines in their thermal spectra

CCO 1E 1207.4–5209 was the first neutron star whose thermal spectrum was found to have features resembling two broad absorption lines [171]. The third and fourth spectral lines were reported in [172], but their statistical significance was called into question [173]. It is possible that the complex shape of CCO PSR J0821–4300 may also be due to an absorption line [167].

[2] Some binaries show type-II X-ray bursts, which recur more frequently than type-I bursts, typically every several minutes or seconds. They may be caused by gravitational instabilities of accreting matter, rather than by thermonuclear reactions [150].

[3] This term is not absolutely precise because some of these objects have revealed radio emission [158, 159].

Features that are possibly related to resonant absorption are also found in the spectra of four XDINSs: RX J0720.4–3125 [174, 175], RX J1308.6+2127 (RBS1223) [176], 1RXS J214303.7+065419 (RBS1774) [177–179], and RX J1605.3+3249 [180]. Possible absorption features were also reported in the spectra of two more XDINSs, RX J0806.4–4123 and RX J0420.0–5022 [181], but a confident identification is hampered by uncertainties related to ambiguous spectral background subtraction [165]. Only the Walter star RX J1856.5−3754, which was the first of the Magnificent Seven to be discovered [182], has a smooth spectrum without any features in the X-ray range [183].

An absorption line was recently found in the spectrum of SGR 0418+5729 in [184]. Its energy varies from < 1 keV to ~ 4 keV with the rotational phase. The authors interpret this as a proton cyclotron line associated with a highly nonuniform magnetic field distribution between $\sim 2\times 10^{14}$ G and $\sim 10^{15}$ G, and explain the discrepancy with the estimate $B \approx 6\times 10^{12}$ G according to Eqn (1) [51] by the absence of a large-scale dipolar component of the superstrong magnetic field (which can be contained in spot, for example). They reject the electron-cyclotron interpretation on the grounds that it would imply $B \approx (1-5)\times 10^{11}$ G, again at odds with the estimate [51]. We note that the last contradiction can be resolved in models [53–56] that involve a residual accretion torque (Section 1). Nor is there a discrepancy if the line has a magnetospheric rather than photospheric origin. Similar puzzling lines had been previously observed in gamma-ray bursts of magnetars [48, 185, 186].

Unlike the radio quiet neutron stars, the spectra of ordinary pulsars were until recently successfully described by a combination of smooth thermal and nonthermal spectral models. The first exception is the radio pulsar PSR J1740+1000, whose X-ray spectrum is found to have absorption features [187]. This discovery fills the gap between the spectra of pulsars and radio quiet neutron stars and shows that similar spectral features can be pertinent to different neutron-star classes.

Currently, there is no unambiguous or incontestable theoretical interpretation of the features in neutron-star spectra. There have been relatively successful attempts to interpret the spectra of some of them. In Section 8, we consider interpretations that are based on magnetic neutron-star atmosphere models.

4. Nonmagnetic atmospheres

4.1. Which atmosphere can be treated as nonmagnetic?

The main results of atmosphere modeling are the outgoing radiation spectra. In [188], the conditions were formulated that allow calculating a neutron-star spectrum without taking the magnetic field into account. In the theory of stellar atmospheres, the interaction of electromagnetic radiation with matter is conventionally described with the use of opacities $\varkappa$, that is, absorption and scattering cross sections per unit mass of the medium. The opacities of fully ionized atmospheres do not depend on the magnetic field at frequencies ω that are much larger than the electron cyclotron frequency $\omega_c = eB/(m_e c)$, which corresponds to the energy $\hbar\omega_c \approx 11.577\, B_{12}$ keV. On this ground, it was concluded in [188] that for the energies $\hbar\omega \sim (1-10)\, k_B T$, which correspond to the maximum of a thermal spectrum, the magnetic-field effects on opacities can be neglected if

$$B \ll \frac{m_e c}{\hbar e}\, k_B T \sim 10^{10}\, T_6 \text{ G}. \tag{24}$$

Strictly speaking, estimate (24) is not absolute. If the atmosphere contains an appreciable fraction of atoms or ions in bound states, then even a weak magnetic field changes the opacities by spectral line splitting (the Zeeman and Paschen–Back effects). Furthermore, the magnetic field polarizes radiation in plasmas [189]. The Faraday and Hanle effects, which are related to polarization, serve as useful tools in studying of stellar atmospheres and magnetic fields, especially the Sun (see [190] for a review). But the bulk of neutron-star thermal radiation is emitted in X-rays, whose polarimetry is only beginning to develop, and therefore such fine effects for neutron stars are often ignored.

A magnetic field drastically affects the opacities of partially ionized photosphere if the electron cyclotron frequency $\hbar\omega_c$ is comparable to or larger than the electron binding energies E_b. Because of the high density of neutron-star photospheres, highly excited states, which have relatively large sizes and low binding energies, do not survive (the disappearance of bound states with increasing density is called pressure ionization). For low-lying electron levels of atoms and positive atomic ions in the absence of a strong magnetic field, the binding energy can be estimated as $E_b \sim (Z+1)^2$ Ry, where Z is the charge of the ion and $\text{Ry} = m_e e^4/(2\hbar^2) = 13.605$ eV is the Rydberg constant in energy units. Consequently, the condition $\hbar\omega_c \ll E_b$ is fulfilled at

$$B \ll \frac{B_0\,(Z+1)^2}{2}, \tag{25}$$

where

$$B_0 = \frac{m_e^2\, c\, e^3}{\hbar^3} = 2.3505\times 10^9 \text{ G} \tag{26}$$

is the atomic unit of the magnetic field. Conditions (24) and (25) are fulfilled for most millisecond pulsars and accreting neutron stars.

4.2 Radiative transfer

The nonmagnetic photosphere of a neutron star does not essentially differ from photospheres of ordinary stars. However, quantitative differences can give rise to specific problems: for instance, the strong gravity results in high density, and hence the plasma nonideality that is usually neglected in stellar atmospheres can become significant. Nevertheless, the spectrum that is formed in a nonmagnetic neutron-star photosphere can be calculated using the conventional methods that are described in the classical monograph by Mihalas [104]. For stationary neutron-star atmospheres, thanks to their small thickness, the approximation of a plane-parallel locally uniform layer is quite accurate. The local uniformity means that the specific intensity at a given point of the surface can be calculated neglecting the nonuniformity of the flux distribution over the surface, that is, the nonuniformity of T_s.

Almost all models of neutron-star photospheres assume radiative and local thermodynamic equilibrium (LTE; see [191] for a discussion of this and alternative approximations). Under these conditions, it suffices to solve a system of three basic equations: those of radiative transfer, hydrostatic equilibrium, and energy balance.

The first equation can be written in a plane-parallel layer as (see, e.g., [192])

$$\cos\theta_k \frac{\mathrm{d}I_\omega(\hat{\mathbf{k}})}{\mathrm{d}y_{\mathrm{col}}} = \varkappa_\omega I_\omega - \int_{(4\pi)} \varkappa_\omega^{\mathrm{s}}(\hat{\mathbf{k}}', \hat{\mathbf{k}})\, I_\omega(\hat{\mathbf{k}}')\, \mathrm{d}\hat{\mathbf{k}}' - \varkappa_\omega^{\mathrm{a}} \mathcal{B}_{\omega,T}\,, \quad (27)$$

where $\hat{\mathbf{k}}$ is the unit vector along $\mathbf{k}$,

$$\varkappa_\omega = \varkappa_\omega^{\mathrm{a}} + \int_{(4\pi)} \varkappa_\omega^{\mathrm{s}}(\hat{\mathbf{k}}', \hat{\mathbf{k}})\, \frac{\mathrm{d}\hat{\mathbf{k}}'}{4\pi}$$

is the total opacity, $\varkappa_\omega^{\mathrm{a}}$ and $\varkappa_\omega^{\mathrm{s}}(\hat{\mathbf{k}}', \hat{\mathbf{k}})$ are its respective components due to the true absorption and the scattering that changes the ray direction from $\hat{\mathbf{k}}'$ to $\hat{\mathbf{k}}$, and $\mathrm{d}\hat{\mathbf{k}}' = \sin\theta_{k'}\, \mathrm{d}\theta_{k'}\, \mathrm{d}\varphi_{k'}$ is a solid angle element. Most studies of neutron-star photospheres neglect the dependence of $\varkappa_\omega^{\mathrm{s}}$ on $\hat{\mathbf{k}}'$ and $\hat{\mathbf{k}}$. As shown in [193], the inaccuracy that is introduced by this simplification does not exceed 0.3% for the thermal spectral flux of a neutron star at $\hbar\omega < 1$ keV and reaches a few percent at higher energies.

For simplicity, we neglected the polarization of radiation and a change in frequency at the scattering in Eqn (27). In general, the radiative transfer equation includes the integral of I_ω not only over angles but also over frequencies, and if polarization is taken into account, I_ω is replaced by a vector of Stokes parameters and the scattering cross section is replaced by a matrix. A detailed derivation of the transfer equations for polarized radiation is given, for example, in [192], and solutions of the radiative transfer equation with frequency redistribution are studied in [191].

The condition of hydrostatic equilibrium follows from Eqn (5). Given that $|R - r| \ll R$, $|M - M_r| \ll M$, and $P \ll \rho c^2$ in the photosphere, we have

$$\frac{\mathrm{d}P}{\mathrm{d}y_{\mathrm{col}}} = g - g_{\mathrm{rad}}\,, \quad (28)$$

where (see, e.g., [194])

$$g_{\mathrm{rad}} = \frac{1}{c}\frac{\mathrm{d}}{\mathrm{d}y_{\mathrm{col}}} \int_0^\infty \mathrm{d}\omega \int_{(4\pi)} \mathrm{d}\hat{\mathbf{k}}\, \cos^2\theta_k\, I_\omega(\hat{\mathbf{k}}) \approx \frac{2\pi}{c}\int_0^\infty \mathrm{d}\omega\, \varkappa_\omega \int_0^\pi \cos\theta_k\, I_\omega(\hat{\mathbf{k}})\, \sin\theta_k\, \mathrm{d}\theta_k\,. \quad (29)$$

The last approximate equality becomes exact for isotropic scattering. The quantity g_{rad} accounts for the radiation pressure that counteracts gravity. It becomes appreciable at $T_{\mathrm{eff}} \gtrsim 10^7$K. Therefore, g_{rad} is usually dropped in calculations of the spectra of the cooler isolated neutron stars, but is included in models of relatively hot bursters. The radiative flux of the bursters amply increases during the bursts, thus increasing g_{rad}. The critical value of g_{rad} corresponds to the stability limit, beyond which matter inevitably flows away under the pressure of light. In a hot nonmagnetic atmosphere, where Thomson scattering dominates, the instability appears when the luminosity L_{ph} exceeds the Eddington limit

$$L_{\mathrm{Edd}} = 4\pi c(1+z_{\mathrm{g}})\frac{GMm_{\mathrm{p}}}{\sigma_{\mathrm{T}}} \approx 1.26\times 10^{38}\,(1+z_{\mathrm{g}})\,\frac{M}{M_\odot}\ \mathrm{erg\,s^{-1}}\,, \quad (30)$$

where m_{p} is the proton mass and

$$\sigma_{\mathrm{T}} = \frac{8\pi}{3}\left(\frac{e^2}{m_{\mathrm{e}}c^2}\right)^2 \quad (31)$$

is the Thomson cross section. A temperature-dependent relativistic correction to σ_{T} [195] increases L_{Edd} by approximately 7% at typical temperatures $\sim 3\times 10^7$ K at the bursters' luminosity maximum [151, 194].

Finally, the energy balance equation in the stationary state expresses the fact that the energy acquired by an elementary volume equals the lost energy. The radiative equilibrium assumes that the energy transport through the photosphere is purely radiative, that is, the electron heat conduction and convection as well as other sources and leaks of heat are neglected. Under these conditions, the energy balance equation reduces to

$$\int_0^\infty \mathrm{d}\omega \int_{(4\pi)} I_\omega(\hat{\mathbf{k}})\, \cos\theta_k\, \mathrm{d}\hat{\mathbf{k}} = F_{\mathrm{ph}}\,, \quad (32)$$

where F_{ph} is the local flux on the surface, which is related to T_{s} by Eqn (11).

Radiation is almost isotropic at a large optical depth,

$$\tau_\omega = \int_r^\infty \varkappa_\omega(r')\, \mathrm{d}y_{\mathrm{col}}(r')\,, \quad (33)$$

and therefore we can restrict ourself to the first two terms of the intensity expansion in spherical functions:

$$I_\omega(\hat{\mathbf{k}}) = J_\omega + \frac{3}{4\pi}\,\mathbf{F}_\omega\hat{\mathbf{k}}\,. \quad (34)$$

Here, $J_\omega = (1/4\pi)\int_{(4\pi)} I_\omega(\hat{\mathbf{k}})\, \mathrm{d}\hat{\mathbf{k}}$ is the mean intensity averaged over all directions and $\mathbf{F}_\omega = \int_{(4\pi)} I_\omega(\hat{\mathbf{k}})\, \hat{\mathbf{k}}\, \mathrm{d}\hat{\mathbf{k}}$ is the diffusive flux vector. Then integro-differential equation (27) reduces to a diffusion-type equation for J_ω. If scattering is isotropic, then, in the plane-parallel locally uniform approximation, the stationary diffusion equation has the form

$$\frac{\mathrm{d}^2}{\mathrm{d}\tau_\omega^2}\,\frac{J_\omega}{3} = \frac{\varkappa_\omega^{\mathrm{s}}}{\varkappa_\omega}\,(J_\omega - \mathcal{B}_{\omega,T}) \quad (35)$$

(see [196] for the derivation of the diffusion equation from the radiative transfer equation in a more general case). Sometimes the diffusion approximation is applied to the entire atmosphere, rather than to only its deep layers. In this case, we have to replace $J_\omega/3$ in the left-hand side of Eqn (35) with $f_\omega J_\omega$, where $f_\omega(\tau_\omega)$ is the so-called Eddington factor [104], which is determined by iterations of the radiative-transfer and energy-balance equations with boundary conditions (see [188] for the details).

In modeling burster atmospheres, Eqn (35) is typically used with the Eddington factor in the left-hand side and an additional term in the right-hand side, a differential Kompaneets operator [197] acting on J_ω (see, e.g., [198–201]). In the diffusion approximation, the Kompaneets operator describes the photon frequency redistribution due to the Compton effect, which cannot be neglected at the high temperatures typical of bursters.

To close the system of equations of radiative transfer and hydrostatic balance, we need the EOS and opacities $\varkappa_\omega^{\mathrm{s,a}}$ for all densities and temperatures encountered in the photosphere. In turn, in order to determine the EOS and opacities, it is

necessary to find the ionization distribution for the chemical elements that compose the photosphere. The basis for solving these problems is provided by quantum mechanics of all particle types that make a significant contribution to the EOS or opacities. In nonmagnetic neutron-star photospheres, these particles are only electrons and atomic ions, because molecules do not survive the typical temperatures $T \gtrsim 3 \times 10^5$ K.

We do not discuss the details of the calculations of the EOS and opacities in the absence of a strong magnetic field, because they do not basically differ from the ones for ordinary stellar atmospheres, which have been thoroughly considered, for instance, in review [202]. Detailed databases have been developed for them (see [203] for a review), the most suitable of which for neutron-star photospheres are OPAL [204] and OP [205].[4] In the particular cases where the neutron-star atmosphere consists of hydrogen or helium, all binding energies are smaller than T, and therefore the approximation of an ideal gas of electrons and atomic nuclei is applicable.

Systematic studies of neutron-star photospheres of different chemical compositions, from hydrogen to iron, started from the work by Romani [207]. In the subsequent quarter of a century, nonmagnetic neutron star photospheres were examined in many studies (see [116] for a review). Databases of neutron-star hydrogen photosphere model spectra have been published [188, 208, 209],[5] and a numerical code for their calculation has been released [193].[6] A publicly available database of model spectra for carbon photospheres has recently been published [211].[7] In addition, model spectra were calculated for neutron-star photospheres composed of helium, nitrogen, oxygen, iron (see, e.g., [209, 212–214]), and mixtures of different elements [208, 213].

4.3 Atmospheres of bursters

Burster spectra have been analyzed by many authors (see, e.g., [151] for the references), starting from the pioneering studies [153, 215–217]. These analyses as well as observations show that the X-ray spectra of bursters at high luminosities are close to the so-called diluted blackbody spectrum

$$F_\omega \approx w\mathcal{B}_{\omega,T_{\rm bb}}\,, \tag{36}$$

where $\mathcal{B}_{\omega,T}$ is Planck function (18), the parameter $T_{\rm bb}$ is called the color temperature, the normalization w is a dilution factor, and the ratio $f_{\rm c} = T_{\rm bb}/T_{\rm eff}$ (typically $\sim 3/2$) is called the color correction [151, 216, 217]. The apparent color temperature $T_{\rm bb}^\infty$ is related to $T_{\rm bb}$ by a relation analogous to (6).

If the luminosity reaches the Eddington limit during a thermonuclear burst, the photosphere radius $R_{\rm ph}$ first increases and then returns to the initial value R at the relaxation stage [195]. Based on this model, Kaminker et al. [218] suggested a method for analyzing the Eddington bursts of bursters and for the first time applied it to obtaining constraints of the parameters of the burster MXB 1728–34. Subsequently, this method was amended and modernized by other authors (see [151] for the references).

According to Eqn (9), the bolometric flux is $F_{\rm bol} = L_{\rm ph}^\infty/(4\pi D^2) = \sigma_{\rm SB}(T_{\rm eff}^\infty)^4(R_{\rm ph}^\infty/D)^2$. But approximation (36) implies that $F_{\rm bol} = w\sigma_{\rm SB}(T_{\rm bb}^\infty)^4(R_{\rm ph}^\infty/D)^2$. Therefore, at the late stage of a long burst, when $R_{\rm ph} = R = \text{const}$, $w \propto f_{\rm c}^{-4}$. On the other hand, the dependence of $f_{\rm c}$ on $L_{\rm ph}$ can be obtained from numerical calculations. This possibility is based on the method for studying bursters that was implemented in the series of papers by Suleimanov et al. [151, 200]. The calculations show that $f_{\rm c}$ mainly depends on the ratio $l_{\rm ph} = L_{\rm ph}/L_{\rm Edd}$ and also on the acceleration of gravity g and the chemical composition of the photosphere (mostly on the helium-to-hydrogen fractional abundance, and to a less extent on the content of heavier elements). With the observed spectral normalizations $f_{\rm c}^{-4}(l_{\rm ph})$ approximated by the results of theoretical calculations, we find the chemical composition that provides an agreement between the theory and observations. For this selected composition, we find the color correction that corresponds to the observed one at different values of g, and thus obtain a curve of allowed values in the (M, R) plane. The point at this curve that satisfies the condition $F_{\rm bol} = l_{\rm ph}F_{\rm Edd}$, where $F_{\rm Edd} = L_{\rm Edd}/[4\pi D^2(1+z_{\rm g})^2]$ is the bolometric flux corresponding to Eddington luminosity (30), gives an estimate of the mass and radius of the neutron star, if the distance D is known. If D is unknown, then this analysis allows obtaining constraints on joint values of M, R, and D.

This method was successfully applied to analyzing the long bursts of bursters 4U 1724–307 [151] and GS 1826–24 [219]. In both cases, there was a marked agreement of the observed and calculated dependences $f_{\rm c}(l_{\rm ph})$. In [219], the authors also simulated light curves, that is, the time dependences of $F_{\rm bol}$. As in an earlier study [220], they managed to find the chemical composition of the atmosphere and the accretion rate such that the theoretical light curve of each burst and the intervals between the bursts agree with observations. Thus, they obtained an absolute calibration of the luminosity. A comparison of the theoretical and observed dependences gives an estimate of the ratio $f_{\rm c}/(1+z_{\rm g})$, which does not depend on the distance D, thus providing additional constraints on the neutron-star mass and radius [151, 219]. A possible anisotropy of the emission, which modifies the total flux (for example, because of screening and reflection of part of the radiation by the accretion disk) is equivalent to multiplying D by a constant factor; therefore, it does not affect the D-independent estimates [219].

In [221–223], the authors used a simplified analysis of he spectra of bursters, ignoring the dependence $f_{\rm c}(l_{\rm ph})$, but only assuming that the Eddington luminosity is reached at the 'touchdown point,' determined by the maximum of the color temperature. This assumption is inaccurate, and therefore such a simplified analysis is invalid: it gives considerably lower R values than the method described above. In addition, the authors of [221–223] analyzed 'short' bursts, for which the theory fails to describe the dependence $f_{\rm c}(l_{\rm ph})$, and the usual separation of spectral components becomes ambiguous (see Section 3.3). Therefore, simplified estimates of neutron-star parameters [221–223] are unreliable (see the discussion in [151]).

We must note that the current results for bursters still leave some open questions. First, the estimates for two different sources in [151] and [219] are difficult to reconcile: in the case of the H atmosphere model, the former estimate indicates a relatively large neutron-star radius and hence a stiff EOS, whereas the latter gives a constraint that implies a

[4] The OPAL opacities are included in the MESA project [206], and the OP database is available at http://cdsweb.u-strasbg.fr/topbase/TheOP.html.
[5] NSA, NSAGRAV, and NSATMOS models in the *XSPEC* database [210].
[6] https://github.com/McPHAC/.
[7] CARBATM model in the *XSPEC* database [210].

soft EOS. Second, good agreement between the theory and observations has been achieved only for a limited decaying part of the lightcurves. Third, there is a lack of an explanation for different normalizations of spectra for the bursts that have different recurrence times. In [219], the authors discuss these uncertainties and possible prospects of their resolution with the aid of future observations.

4.4 Photospheres of isolated neutron stars

Nonmagnetic atmospheres of isolated neutron stars differ from accreting neutron star atmospheres, first of all, by a lower effective temperature $T_s \sim 3 \times (10^5 - 10^6)$ K, and possibly also by chemical composition. Examples of spectra of such atmospheres are given in Fig. 3.

If there was absolutely no accretion on a neutron star, the atmosphere would have to consist of iron. The spectrum of such an atmosphere has a maximum in the same wavelength range as the blackbody spectrum, but contains many features caused by bound–bound transitions and photoionization [207, 208, 212, 224]. Absorption lines and photoionization edges are smeared with increasing g, because the photosphere becomes denser, thus increasing the effects leading to line broadening [225] (for example, fluctuating microfields in the plasma [226]).

If the atmosphere consists of hydrogen and helium, the spectrum is smooth, but shifted to higher energies compared with the blackbody spectrum at the same effective temperature [188, 207]. As shown in [188], this shift is caused by the decrease in light-element opacities according to the law $\varkappa_\omega \propto \omega^{-3}$ for $\hbar\omega > k_B T \sim 0.1$ keV, which makes photons with larger energies come from deeper and hotter photosphere layers. The polar diagrams of radiation coming from the atmosphere were also discussed in [188]. Unlike the blackbody radiation, this radiation is strongly anisotropic ($I_\omega(\hat{\mathbf{k}})$ rapidly decreases at large angles θ_k), and the shape of the polar diagram depends on the frequency ω and on the chemical composition of the atmosphere.

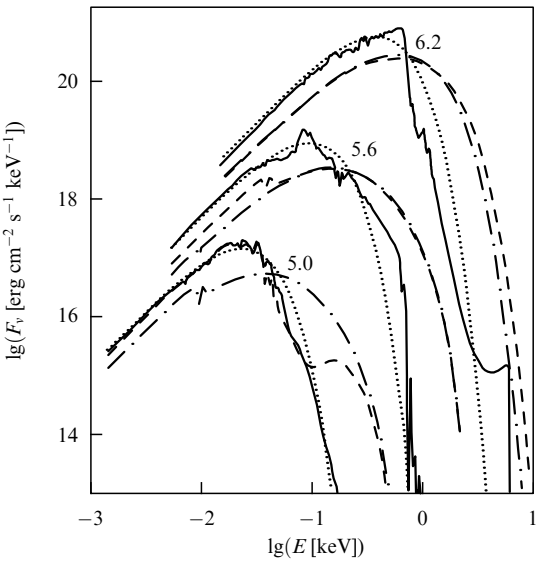

Figure 3. Radiation energy flux densities as functions of the photon energy $E = \hbar\omega$ for a photosphere composed of iron (solid lines), helium (dashed lines), and hydrogen (dotted-dashed lines) compared to the blackbody spectrum (dotted lines) at $g_{14} = 2.43$ for different values of the effective temperature (numbers on the curves correspond to log $T_{\rm eff}$ [K]). (Fig. 3 from [213], courtesy of J Pons and ©AAS.)

The Compton effect on the spectra of isolated neutron stars was taken into account in [227] using the same technique as for bursters. The authors have shown that this effect results in a decrease in the high-energy flux at $\hbar\omega \gg 1$ keV for hydrogen and helium atmospheres. It becomes considerable at high effective temperatures $T_s > 10^6$ K, where the spectral maximum shifts to the energies $E \gtrsim 1$ keV. This effect makes the spectra of hot hydrogen and helium atmospheres closer to the blackbody spectrum with the color correction $f_c \approx 1.6 - 1.9$.

Papers [224, 228] stand apart, being the only ones where non-LTE calculations were done for the spectrum of an iron neutron-star atmosphere. At $T = 2 \times 10^5$ K, the difference from the LTE model is about 10% for the flux in the lines and much less in the continuum [208, 224]. As noted in [208], the difference may be larger at higher temperatures, which indeed turned out to be the case in [228].

A thorough study was performed in [213] in an attempt to describe the observed spectrum of the Walter star RX J1856.5−3754 by nonmagnetic atmosphere models with various chemical compositions. It turned out that the hydrogen atmosphere model that reproduces the X-ray part of the spectrum predicts approximately 30 times larger optical luminosity than observed, whereas an iron-atmosphere model corresponds to too small a radius. This demonstrates once again that a neutron-star radius estimate strongly depends on the assumptions on its atmosphere. Satisfactory results have been obtained for the chemical composition corresponding to the ashes of thermonuclear burning of matter that was accreted on the star at the early stage of its life. This model, as well as other models of atmospheres composed of elements heavier than helium, predicted absorption lines in the X-ray spectrum. But subsequent deep X-ray observations with the space observatories *Chandra* [229] and *XMM-Newton* [83] have not found such lines.

The failure of the interpretation of the Walter star spectrum with nonmagnetic atmosphere models can be explained by the presence of a strong magnetic field. The field is indicated by a nearby nebula glowing in the Hα line [230]. Such nebulae are found near pulsars, which ionize interstellar hydrogen by shock waves arising from the hypersonic pulsar magnetosphere interacting with interstellar medium [52, 231]. Doubts had initially been cast on the pulsar analogy by the absence of observed pulsations of the radiation of this star, but soon such pulsations were discovered [232]. Interpretation of the Walter star spectrum with magnetic atmosphere models is considered in Section 8.1.

The first successful interpretation of an isolated neutron star spectrum based on a nonmagnetic atmosphere model was made in [214]. The authors showed that the observed X-ray spectrum of the CCO in the Cassiopeia A supernova remnant, which appeared around 1680, is well described by a carbon atmosphere model with the effective temperature $T_{\rm eff} \sim 2 \times 10^6$ K. Subsequent observations revealed that $T_{\rm eff}$ appreciably decreases with time [233], which was explained by the heat-carrying neutrino emission outburst caused by the superfluid transition of neutrons [234, 235]. At $t_* \approx 330$ y, this agrees with the cooling theory [97]. An independent analysis [236] confirmed the decrease in the registered flux, but the authors stressed that the statistical significance of this result is not high and that the same observational data allow other interpretations. Recently, a spectrum of one more CCO, residing in supernova remnant HESS J1731–347, was also

satisfactorily described by a nonmagnetic carbon atmosphere model [237].

4.5 Atmospheres of neutron stars in qLMXBs

Many SXTs reside in globular clusters, whose distances are known with accuracies of 5 – 10%. This reduces a major uncertainty that hampers the spectral analysis. As we noted in Section 3, spectra of SXTs in quiescence, called qLMXBs, are probably determined by the neutron-star thermal emission. In early studies, these spectra were interpreted with the Planck function, which overestimated the effective temperature and underestimated the effective radius of the emitting area. It was found in [144, 238, 239] that the nonmagnetic hydrogen atmosphere model allows explaining the SXT spectra as caused by radiation from the entire neutron-star surface with acceptable values of the temperature and radius.

Currently, dozens of qLMXBs in globular clusters are known (they are listed in [240, 241]), and the use of hydrogen atmosphere models for their spectral analysis has become customary. For instance, the analysis of the cooling of KS 1731–260 and other similar objects that was discussed in Section 3.1 was based on the measurements of the effective temperature $T_{\rm eff}$ with the use of the NSA [188] and NSATMOS [209] models.

In many studies (including [130–132]), the neutron-star mass and radius were a priori fixed at $M = 1.4\,M_\odot$ and $R = 10$ km, which imply that $g_{14} = 2.43$. It was shown in [209] that fixing g this way may strongly bias estimates of the neutron-star parameters (which means, in particular, that the estimates of $T_{\rm eff}$ for KS 1731–260 and MXB 1659–29, quoted in Section 3.7, are unreliable). An analysis of the thermal spectrum of qLMXB X7 in the globular cluster 47 Tuc, free of such fixing, gave a 90%-confidence area of M and R estimates, which agrees with relatively stiff EOSs of supranuclear matter [209]. But the estimates obtained in [242] by an analogous analysis for five qLMXBs in globular clusters, although widely scattered, generally better agree with soft EOSs. In [243, 244], the thermal spectra of two qLMXBs were analyzed using hydrogen and helium atmosphere models. It turned out that the former model leads to low estimates of M and R, compatible with the soft EOSs, while the latter yields high values, which require a stiff EOS of superdense matter. Thus, despite the progress achieved in recent years, the estimates of neutron-star masses and radii based on the qLMXB spectral analysis are not yet definitive.

4.6 Photospheres of millisecond pulsars

The magnetic fields of most millisecond pulsars satisfy the weak-field criteria formulated in Section 4.1. Nevertheless, the magnetic field does play a certain role, because the open field line areas ('polar caps') may be heated by deceleration of fast particles (see Section 2.6). Therefore, the nonuniform temperature distribution must be taken into account when calculating the integral spectrum.

Models of rotating neutron stars with hot spots have been presented in many publications (see, e.g., [72, 245, 246] and the references therein), but most of them use the blackbody radiation model. This model is acceptable for a preliminary qualitative description of the spectra and light curves of millisecond pulsars, but a detailed quantitative analysis must take the photosphere into account. We consider the results of such analyses.

The nearest and brightest of the four millisecond pulsars with observed thermal radiation is PSR J0437 – 4715. It belongs to a binary system with a 6-billion-year-old white dwarf. The low effective temperature of the white dwarf (~ 4000 K), as well as the brightness of the pulsar and the relatively low intensity of its nonthermal emission, favors the analysis of the thermal spectrum. Recently, the pulsar thermal radiation has been extracted from the white-dwarf radiation even in the ultraviolet range [247], although the maximum of the pulsar thermal radiation lies in the X-ray range. It was shown in [248] that the thermal X-ray spectrum of PSR J0437 – 4715 can be explained by the emission of two hot polar caps with hydrogen photospheres and a nonuniform temperature distribution, which was presented by the authors as a steplike function with the higher value $T \approx (1-2) \times 10^6$ K in the central circle of the radius 0.2 – 0.4 km and the lower value $T \approx (3-5) \times 10^5$ K in the surrounding broad ring with a radius about several kilometers.

Subsequent observations of the binary system J0437 – 4715 in the spectral ranges from infrared to hard X-rays and their analysis in [102, 249, 250] have generally confirmed the qualitative conclusions in [248]. In [102, 250], in particular, not only the spectrum but also the light curve of this pulsar in the X-ray range was reproduced using the model of a hydrogen atmosphere with a steplike temperature distribution, supplemented with a power-law component. These authors have also explained [251] the power-law spectral component by Compton scattering of thermal polar-cap photons on energetic electrons in the magnetosphere or in the pulsar wind. Hence, all the spectral components may have a thermal origin. Finally, Bogdanov [252] reanalyzed the phase-resolved X-ray spectrum of PSR J0437–4715 using the value $M = (1.76 \pm 0.20)\,M_\odot$ obtained from radio observations [253], the distance $D = 156.3$ pc measured by radio parallax [254], a nonmagnetic hydrogen atmosphere model NSATMOS [209], and a three-level distribution of $T_{\rm eff}$ around the polar caps. As a result, he came to the conclusion that the radius of a neutron star of that mass cannot be smaller than 11 km, which favors the stiff equations of state of supranuclear matter.

The presence of a hydrogen atmosphere helps to explain not only the spectrum but also the relatively large pulsed fraction (30 – 50%) in the thermal radiation of this and the three other millisecond pulsars with observed thermal components of radiation (PSR J0030 + 0451, J2124–3358, and J1024–0719). According to [116, 250], such strong pulsations may indicate that all similar pulsars have hydrogen atmospheres. The measured spectra and light curves of all the four pulsars agree with this assumption [250].

5. Matter in strong magnetic fields

The conditions discussed in Section 4.1 are not satisfied for most of the known isolated neutron stars; therefore, magnetic fields drastically affect radiative transfer in their atmospheres. Before discussing magnetized atmosphere models, it is useful to consider the magnetic field effects on their constituent matter.

5.1 Landau quantization

The motion of charged particles in a magnetic field is quantized in Landau orbitals [255]. This means that only the longitudinal (parallel to **B**) momentum of the particle can change continuously. The motion of a classical charged particle across a magnetic field is restricted to circular

orbits, corresponding to a set of discrete quantum states, analogous to the states of a two-dimensional oscillator.

A complete theoretical description of the quantum mechanics of free electrons in a magnetic field is given in [256]. It is convenient to characterize the magnetic field by its strength in relativistic units b and in atomic units γ:

$$b = \frac{\hbar\omega_c}{m_e c^2} = \frac{B}{B_{QED}} = \frac{B_{12}}{44.14}\,, \tag{37}$$

$$\gamma = \frac{B}{B_0} = 425.44\, B_{12}\,. \tag{38}$$

We have already dealt with the atomic unit B_0 in Section 4.1. The relativistic unit $B_{QED} = m_e^2 c^3/(e\hbar) = B_0/\alpha_f^2$ is the critical (Schwinger) field above which specific QED effects become pronounced. In astrophysics, the magnetic field is called *strong* if $\gamma \gg 1$ and *superstrong* if $b \gtrsim 1$.

In nonrelativistic theory, the distance between Landau levels equals the cyclotron energy $\hbar\omega_c$. In the relativistic theory, Landau-level energies are $E_N = m_e c^2\,(\sqrt{1+2bN}-1)$ $(N = 0, 1, 2, \ldots)$. The wave functions that describe an electron in a magnetic field have the characteristic transverse scale $a_m = (\hbar c/eB)^{1/2} = a_B/\sqrt{\gamma}$, where a_B is the Bohr radius. The momentum projection on the magnetic field remains a good quantum number; therefore, we have the Maxwell distribution for longitudinal momenta in thermodynamic equilibrium. For transverse motion, however, we have the discrete Boltzmann distribution over N.

In practice, the Landau quantization becomes important when the electron cyclotron energy $\hbar\omega_c$ is at least comparable to both the electron Fermi energy ϵ_F and the characteristic thermal energy $k_B T$. If $\hbar\omega_c$ is appreciably larger than both these energies, most electrons reside on the ground Landau level in thermodynamic equilibrium, and the field is called strongly quantizing. For this to be the case, simultaneous conditions $\rho < \rho_B$ and $\zeta_e \gg 1$ must be fulfilled, where

$$\rho_B = \frac{m_i}{\pi^2\sqrt{2}\, a_m^3 Z} = 7045\,\frac{A}{Z}\, B_{12}^{3/2}\ \mathrm{g\ cm^{-3}}\,, \tag{39}$$

$$\zeta_e = \frac{\hbar\omega_c}{k_B T} = 134.34\,\frac{B_{12}}{T_6}\,. \tag{40}$$

In neutron-star atmospheres, these conditions are typically satisfied at $B \gtrsim 10^{11}$ G. In the opposite limit $\zeta_e \ll 1$, the Landau quantization can be neglected. We note that in magnetospheres, which have lower densities, electrons can accumulate on the lowest Landau level even at $B \sim 10^8$ G because of the violation of the LTE conditions (see Section 5.9).

Ions can be treated as nondegenerate and nonrelativistic particles in neutron-star atmospheres. For ions, the parameter ζ_e is replaced by

$$\zeta_i = \frac{\hbar\omega_{ci}}{k_B T} = 0.0737\,\frac{Z}{A}\,\frac{B_{12}}{T_6}\,, \tag{41}$$

where $\omega_{ci} = ZeB/(m_i c)$ is the ion cyclotron frequency and $\hbar\omega_{ci} = 6.35(Z/A)\,B_{12}$ eV is the ion cyclotron energy. In magnetar atmospheres, where $B_{12} \gtrsim 100$ and $T_6 \lesssim 10$, the parameter ζ_i is not small; therefore, the Landau quantization of ion motion should be taken into account.

5.2 Interaction with radiation

The general expression for a differential cross section of absorption of a plane electromagnetic wave by a quantum mechanical system can be written as (see, e.g., [257])

$$\mathrm{d}\sigma = \frac{4\pi^2}{\omega c}\left|\mathbf{e}\,\langle f|\,\mathbf{j}_{\mathrm{eff}}|i\rangle\right|^2 \delta(E_f - E_i - \hbar\omega)\,\mathrm{d}\nu_f\,, \tag{42}$$

where $|i\rangle$ and $|f\rangle$ are the initial and final states of the system, $\mathrm{d}\nu_f$ is the number of final states in the considered energy interval $\mathrm{d}E_f$, $\mathbf{e}$ is the electromagnetic polarization vector, $\mathbf{j}_{\mathrm{eff}} = \sum_i q_i \exp(\mathrm{i}\mathbf{k}\mathbf{r}_i)\,\dot{\mathbf{r}}_i$ is the effective electric current operator, and $\dot{\mathbf{r}}_i$ is the velocity operator acting on a particle with the charge g_i. In calculating the matrix elements $\langle f|\,\mathbf{j}_{\mathrm{eff}}|i\rangle$, it is important to remember that $\dot{\mathbf{r}}_i$ is not proportional to the canonical momentum $\mathbf{p}$ in a magnetic field. For an 'electron + proton' system interacting with radiation in a constant magnetic field, these matrix elements were derived analytically in [258].

In the dipole approximation, the cross section of photon interaction with a plasma particle can be expanded in three components corresponding to the longitudinal, right, and left polarizations with respect to the magnetic field (see, e.g., [189, 259]):

$$\sigma(\omega, \theta_B) = \sum_{\alpha=-1}^{1} \sigma_\alpha(\omega)\left|e_\alpha(\omega, \theta_B)\right|^2. \tag{43}$$

Here, ω is the photon frequency, θ_B is the angle between k and $\mathbf{B}$ (Fig. 1), and $e_0 \equiv e_z$ and $e_{\pm1} \equiv (e_x \pm \mathrm{i}e_y)/\sqrt{2}$ are the components of the decomposition of the electromagnetic polarization vector $\mathbf{e}$ in a cyclic basis in a coordinate system with the z axis directed along $\mathbf{B}$. Representation (43) is convenient because σ_α do not depend on θ_B.

Scattering cross sections in neutron-star photospheres are well known [260–262]. For $\alpha = -1$, the photon–electron scattering has a resonance at the cyclotron frequency ω_c. Outside a narrow frequency interval around ω_c (about the Doppler width), the cross sections for the basic polarizations $\alpha = 0, \pm1$ are written as

$$\sigma_\alpha^{s,e} = \frac{\omega^2}{(\omega + \alpha\omega_c)^2 + \nu_{e,\alpha}^2}\,\sigma_T\,, \tag{44}$$

where σ_T is the nonmagnetic Thomson cross section, Eqn (31), and the effective damping factors $\nu_{e,\alpha}$ are equal to half the total rate of the spontaneous and collisional decay of the electron state with the energy $\hbar\omega$ (see [268]). The ion cross section is similar:

$$\sigma_\alpha^{s,i} = \left(\frac{m_e}{m_i}\right)^2 \frac{\omega^2 Z^4}{(\omega - \alpha\omega_{ci})^2 + \nu_{i,\alpha}^2}\,\sigma_T\,. \tag{45}$$

In contrast to the nonmagnetic case, we cannot neglect the scattering on ions in superstrong fields because $\sigma_{+1}^{s,i}$ has a resonance at the frequency ω_{ci}.

In the absence of a magnetic field, the absorption of a photon by a free electron is possible only upon interaction with a third particle, which takes away the difference of the total electron–photon momentum before and after the absorption. In a quantizing magnetic field, electron transitions between the Landau levels are also possible. In nonrelativistic theory, such transitions occur between equidistant neighboring levels at the frequency ω_c, which corresponds to the dipole approximation. In the relativistic theory, the multipole expansion leads to the appearance of cyclotron harmonics [71]. Absorption cross sections at these harmonics

were derived in [263] in the Born approximation, without taking the magnetic quantization of electron motion into account, and were represented in a compact form in [264].

Including the quantization of electron motion leads to the appearance of cyclotron harmonics in the nonrelativistic theory as well. In [265], also in the Born approximation, photon–electron absorption cross sections were derived for an electron moving in a magnetic field and interacting with a nonmoving point-like charge. This model is applicable at $\omega \gg \omega_{ci}$. In the superstrong field of magnetars, the last condition is unacceptable; therefore, we should consider absorption of a photon by a system of finite-mass charged particles, which yields [266, 267]

$$\sigma_\alpha^{ff}(\omega) = \frac{4\pi e^2}{m_e c} \frac{\omega^2 \nu_\alpha^{ff}(\omega)}{(\omega + \alpha\omega_c)^2(\omega - \alpha\omega_{ci})^2 + \omega^2 \tilde{\nu}_\alpha^2(\omega)}, \quad (46)$$

where ν_α^{ff} is the effective photoabsorption collision frequency and $\tilde{\nu}_\alpha$ is the effective frequency, also including other collisions. We see from (46) that σ_{-1}^{ff} and σ_{+1}^{ff} have a resonance at the respective frequencies ω_c and ω_{ci}. Expressions for the effective collision frequencies ν_α^{ff} and $\tilde{\nu}_\alpha$ in the electron–proton plasma are given in [266]. We can write

$$\nu_\alpha^{ff}(\omega) = \frac{4}{3}\sqrt{\frac{2\pi}{m_e T}} \frac{n_e e^4}{\hbar\omega} \Lambda_\alpha^{ff}, \quad (47)$$

where $\Lambda_\alpha^{ff} = (\pi/\sqrt{3})\, g_\alpha^{ff}$ is the Coulomb logarithm and g_α^{ff} is the Gaunt factor, with $g_{-1}^{ff} = g_{+1}^{ff}$. Without the magnetic field, the Gaunt factor is a smooth function of ω. A calculation with the Landau quantization shows, however, that $\nu_\alpha^{ff}(\omega)$ has peaks at the multiples of the electron and ion cyclotron frequencies for all polarizations α.

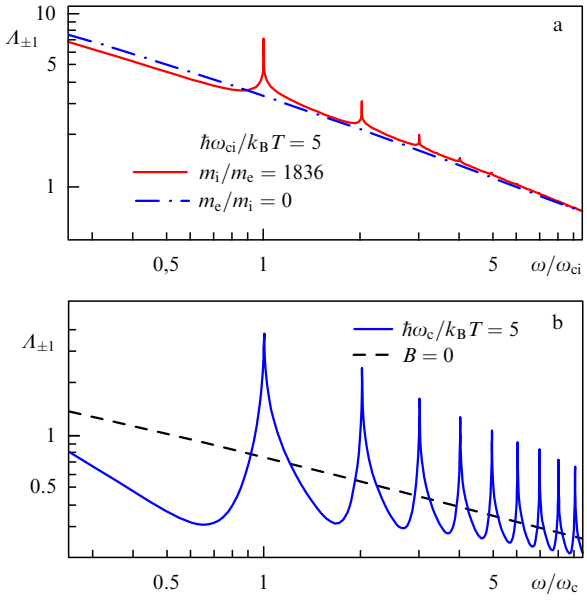

Figure 4. (Color online.) (b) Electron and (a) proton cyclotron harmonics of the Coulomb logarithm for free–free absorption at $\hbar\omega_c = 5k_B T$ and $\hbar\omega_{ci} = 5k_B T$, for photon polarization across a magnetic field. Solid lines show the result of the exact calculation of $\Lambda_1(\omega) = \Lambda_{-1}(\omega)$ in the Born approximation, and the dotted-dashed line in the upper panel shows the infinite-proton-mass approximation (in the lower panel, it effectively coincides with the exact result). For comparison, the dashed line in the lower panel shows the nonmagnetic Coulomb logarithm.

Free–free absorption in a hydrogen plasma with both types (electron and ion) of cyclotron harmonics taken into account was first calculated in [266]; a detailed discussion is given in [267], and a generalization to the case of arbitrary hydrogen-like ions and a discussion of non-Born corrections are presented in [268]. As $\omega_{ci}/\omega \to 0$, the results in Ref. [265] for the electron photoabsorption are reproduced, but we should keep in mind that the ion cyclotron harmonics cannot be obtained by a simple scaling of the electron ones. Such scaling was used in neutron-star atmosphere models starting with [269] until the publication [266], where it was shown to be qualitatively wrong. We can see this in Fig. 4, where the electron and ion cyclotron harmonics are shown on equal scales. In spite of the choice of the same cyclotron-frequency-to-temperature ratio, the cyclotron peaks in the upper panel are much weaker than in the lower panel. The physical reasons for and the consequences of this fact are discussed in detail in [267]. It was also demonstrated in [267] that the ion cyclotron harmonics are so weak that they can be neglected in neutron-star atmospheres.

5.3 Atoms

As was first noticed in [270], atoms with bound states should be much more abundant at $\gamma \gg 1$ than at $\gamma \lesssim 1$ in a neutron-star atmosphere at the same temperature. This difference is caused by the magnetically induced increase in binding energies and the decrease in the sizes of atoms in so-called tightly bound states, which are characterized by electron-charge concentration at short distances to the nucleus. Therefore, it is important that the bound states and bound–bound transitions in a strong magnetic field be taken into account even for light-element atmospheres, which would be almost fully ionized in the nonmagnetic case.

The pioneering work by Loudon, Hasegawa, and Howard [271, 272][8] was at the origin of numerous studies of atoms in strong magnetic fields. In most of these studies, the authors used the model of an atom with an infinitely heavy nucleus (fixed in space). Their results are summarized in a number of reviews (see, e.g., [273, 274]). The model of an infinitely massive nucleus is too crude to describe atoms in the strongly magnetized neutron-star atmospheres, but it is a convenient first approximation. In this section, we therefore keep to this model and postpone going beyond its framework until Section 5.6.

According to the Thomas–Fermi model, the typical size of an atom with a large nuclear charge $Z_n \gg 1$ is proportional to $\gamma^{-2/5}$ in the range $Z_n^{4/3} \ll \gamma \ll Z_n^3$ [275]. At $\gamma \gtrsim Z_n^3$, the usual Thomas–Fermi model of the atom becomes inapplicable [276]. In particular, it cannot describe the difference between the transverse and longitudinal atomic sizes, which becomes huge in such strong fields. In this field range, however, a good starting point is given by the so-called adiabatic approximation, where each electron orbital is represented as a product of a Landau function [256], describing free electron motion in the plane transverse to the field, and a function describing one-dimensional motion of the electron along magnetic field lines in the field of an effective potential similar to the Coulomb potential truncated at zero [277]. At $\gamma \gg Z_n^3$, all electron shells of the atom are strongly compressed in the directions transverse to the field. In the ground state, atomic

[8] Papers [271, 272] and some of the studies cited below were devoted to the Mott exciton in a magnetized solid, which is equivalent to the problem of a hydrogen atom in a strong magnetic field.

sizes along and transverse to **B**, can be estimated as [278]

$$l_\perp \approx \sqrt{2Z_\mathrm{n}-1}\,a_\mathrm{m}, \quad l_\parallel \approx \frac{Z_\mathrm{n}^{-1}a_\mathrm{B}}{\ln\left[\sqrt{\gamma}/(Z_\mathrm{n}\sqrt{2Z_\mathrm{n}-1})\right]}. \quad (48)$$

In this case, the binding energy $E^{(0)}$ of the ground state increases with increasing **B** approximately as $(\ln\gamma)^2$. Here and hereafter, the superscript (0) indicates the approximation of a nonmoving nucleus. At $Z_\mathrm{n} \gg 1$ and $\gamma/Z_\mathrm{n}^3 \to \infty$, the asymptotic estimate is $E^{(0)} \sim -Z_\mathrm{n}\hbar^2/(m_\mathrm{e}l_\parallel^2)$ [278]. But this asymptotic regime is never reached in practice (see Section 5.5).

Quite a large number of studies have been devoted to the simplest atom in a magnetic field, the H atom. Because the electron resides on the ground Landau level $N = 0$ in the hydrogen atom at $B > 10^9$ G, with its spin directed opposite to the field, a bound state is determined by quantum numbers s and v, where $s = 0, 1, 2, \ldots$ corresponds to the electron orbital momentum projection on the magnetic-field direction, $-\hbar s$, and $v = 0, 1, 2, \ldots$ in the adiabatic approximation is equal to the number of wave-function nodes along this direction. The tightly bound atomic states are characterized by the value $v = 0$, while all nonzero values of v correspond to loosely bound states.

Calculations of the hydrogen atom properties beyond the adiabatic approximation have been performed by various methods (variational, discrete-mesh, etc.). At $\gamma \gg 1$, the most natural method of calculations is the expansion of the wave function over the Landau orbitals, which constitute a complete orthogonal functional basis in the plane perpendicular to the magnetic field [279]. Such calculations were done in [279–281] for the bound states and in [282] also for the continuum states, which allowed obtaining the oscillator strengths and the photoionization cross sections. Examples of such cross sections are presented in Fig. 5 for the hydrogen atom at rest in a strong magnetic field for a finite proton mass. The broad peaks correspond to transitions to excited Landau levels $N > 0$, while the narrow peaks and dips near the corresponding partial thresholds with $\hbar\omega \approx N\hbar\omega_\mathrm{c}$ are due to resonances related to autoionization of metastable states.

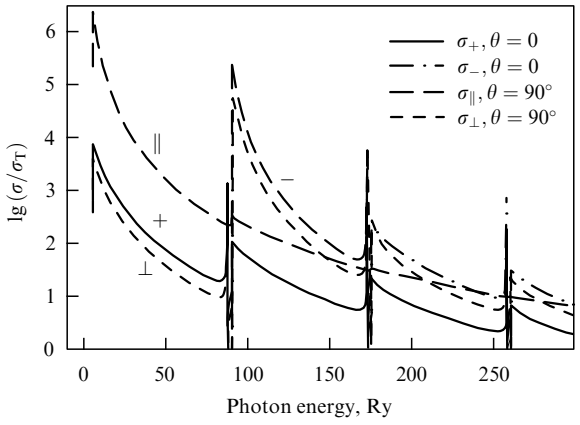

Figure 5. Logarithm of the photoionization cross section, normalized to Thomson cross section (31), $\log(\sigma/\sigma_\mathrm{T})$, as a function of the photon energy $\hbar\omega$ for the ground state of a hydrogen atom at rest in the magnetic field $B = 10^{11}$ G. The curves labeled by '+', '−', and '||' respectively display the cross sections for circular and longitudinal polarizations $\alpha = +1, -1$, and $\alpha = 0$, and the curve labeled '⊥' is for radiation polarized perpendicular to **B**. The wave vector **k** is directed along **B** for $\alpha = \pm 1$ and perpendicular to **B** in the other two cases. (Figure 4 from [282], reproduced with the permission of ©ESO.)

Analytic expressions for atomic characteristics are best suited for astrophysical modeling. However, the asymptotic estimates at $\gamma \gg 1$ do not provide the desired accuracy. For example, the binding energy of the ground-state hydrogen atom at rest, $E_{sv}^{(0)}$ at $s = v = 0$, when calculated in the framework of nonrelativistic quantum mechanics, tends to $(\ln\gamma)^2$ Ry in the limit $\gamma \to \infty$ [271, 277], but this estimate is erroneous by more than a factor of two at any B values that are encountered in neutron stars. With two more terms of the asymptotic expansion included [272], $E_{00}^{(0)} \sim \ln^2(\tilde{\gamma}/\ln^2\tilde{\gamma})$ Ry, where $\tilde{\gamma} \approx 0.28\gamma$. But even this estimate differs from accurate results by 40–80% at $B \sim 10^{12}$–10^{14} G. A possible way to solve this problem consists in constructing analytic approximations to the results of numerical calculations. In [283], we gave accurate fitting formulas for many bound states of the hydrogen atom at $B \lesssim 10^{14}$ G. The energy levels in the infinite-mass approximation were recently revisited by Popov and Karnakov [284], who obtained analytic expressions applicable at $B \gtrsim 10^{11}$ G. Here, we give another approximation for tightly bound levels, valid at *any* B. Temporarily ignoring corrections for vacuum polarization (Section 5.5) and finite nuclear mass (Section 5.6), we represent the binding energy as

$$\frac{E_{s,0}^{(0)}}{\mathrm{Ry}} = \frac{(1+s)^{-2} + (1+s)\,x/a_1 + a_3x^3 + a_4x^4 + a_6x^6}{1 + a_2x^2 + a_5x^3 + a_6x^4}, \quad (49)$$

where $x = \ln(1 + a_1\gamma)$ and a_i are numerical parameters, which we approximate as functions of s:

$$a_1 = \frac{0.862 + 2.5\,s^2}{1 + 0.018\,s^3},$$

$$a_2 = 0.275 + 0.1763\,\delta_{s,0} + \frac{s^{2.5}}{6},$$

$$a_3 = 0.2775 + 0.0202\,s^{2.5},$$

$$a_4 = \frac{0.3157}{(1+2s)^2} - 0.26\,\delta_{s,0},$$

$$a_5 = 0.0431,$$

$$a_6 = \frac{2.075\times10^{-3}}{(1+7s^2)^{0.1}} + 1.062\times10^{-4}\,s^{2.5}.$$

Approximation (49) accurately reproduces the Zeeman shift of the lowest sublevel of each multiplet in the weak-field limit and the correct asymptotic form in the strong-field limit. Its inexactness is confined within 3% for $s < 30$ at $\gamma > 1$ and for $s < 5$ at any γ, and within 0.3% for $s = 0$ at any γ.

Binding energies of loosely bound states ($v \gg 1$) can be evaluated at $\gamma \gtrsim 1$ as

$$E_{s,v}^{(0)} = \frac{1\,\mathrm{Ry}}{(n+\delta)^2}, \quad (50)$$

where

$$n = \frac{v+1}{2}, \quad \delta \approx \frac{1 + s/2}{1 + 2\sqrt{\gamma} + 0.077\gamma} \quad \text{for odd } v;$$

$$n = \frac{v}{2}, \quad \delta \approx \frac{1 + s/8}{0.6 + 1.28\ln(1 + 0.7\gamma^{1/3})} \quad \text{for even } v.$$

As $\gamma \to \infty$, energies (50) tend to those of a field-free H atom (n^{-2} Ry), and therefore the loosely bound states are often

called 'hydrogen-like' (this picture is broken by vacuum polarization; see Section 5.5).

In the approximation of an infinite nuclear mass, the energy of any one-electron ion is related to the hydrogen atom energy as $E(Z_\mathrm{n}, B) = Z_\mathrm{n}^2 E(1, B/Z_\mathrm{n}^2)$ [285]. We see, in particular, that the adiabatic approximation for single-electron ions is applicable at $\gamma \gg Z_\mathrm{n}^2$, which is a weaker condition than for many-electron atoms. Analogous similarity relations also exist for the cross sections of radiative transitions [286]. However, they are violated if we take motion across the magnetic field into account. Even for an atom at rest, the effects of a finite nuclear mass can be important at $s \neq 0$. These effects are considered in Section 5.6.

Binding energies and oscillator strengths of many-electron atoms have been successfully calculated with the use of different methods: variational (see, e.g., [287] and the references therein), density-functional [288–290], Monte Carlo [291, 292], and Hartree–Fock [293, 294]. In the simplest version of the Hartree–Fock method [274, 295, 296], the wave-function basis is constructed from one-electron wave functions in the adiabatic approximation. This method is reliable for calculations of the energies, oscillator strengths, and photoionization cross sections of the helium atom [297]. But for many-electron atoms, the applicability condition of the adiabatic approximation $\gamma \gg Z_\mathrm{n}^3$ is too restrictive. It is overcome in the mesh Hartree–Fock method, where each one-electron orbital is numerically determined as a function of the longitudinal (z) and radial coordinates on a two-dimensional mesh [298] (see also [299] and the references therein), and in the 'twice self-consistent' method [300], where the transverse part of each orbital is presented as a superposition of Landau functions with numerically optimized coefficients. These studies gave a number of important results but were not realized in astrophysical applications. In practice, the optimal method for modeling neutron-star atmospheres containing atoms and ions of elements with $2 < Z_\mathrm{n} \lesssim 10$ proves to be the method by Mori and Hailey [301], where corrections to the adiabatic Hartree approximation are treated by perturbation. This method can provide an acceptable accuracy at moderate computational expenses.

5.4 Molecules and molecular ions

The molecular properties in strong magnetic fields have been studied for almost 40 years, but remain insufficiently known. The best known are the properties of diatomic molecules oriented along the field, especially the H_2 molecule (see [302] and the references therein). Approximate expressions for its binding energy at $\gamma \gtrsim 10^3$, which grows at approximately the same rate $\propto (\ln\gamma)^2$ as the atomic binding energy, were obtained in [303]. In such strong fields, the ground state of this molecule is such that the spins of both electrons are opposite to the magnetic field and the molecular axis is parallel to it, unlike in weak fields, where the ground state is $^1\Sigma_g$. In moderate fields, the behavior of the molecular terms is quite nontrivial. If the molecular axis is parallel to B, the states $^1\Sigma_g$ and $^3\Pi_u$ are metastable for $0.18 < \gamma < 12.3$ and decay into the $^3\Sigma_u$ channel [304]. It turns out, however, that the molecular orientation along **B** is not optimal in such fields: for example, at $\gamma = 1$, the triplet state of a molecule oriented perpendicular to the field has the lowest energy, and at $\gamma = 10$, the ground state is tilted at 37° to **B** [305].

The H_2^+ ion is well studied, including its arbitrary orientations in a magnetic field (see, e.g., [306] and the references therein). The analysis in [307] shows that the abundance of H_2^+ is very small in neutron-star atmospheres, and therefore these ions are unlikely to affect the observed spectra.

Strong magnetic fields stabilize the He_2 molecule and its ions He_2^+, He_2^{2+}, and He_2^{3+}, which do not exist in the absence of the field. The most complete study of their binding energies in neutron-star atmospheres was performed in [308]. The ions HeH^{++} and H_3^{++} and other exotic molecular ions that become stable in strong magnetic fields have also been considered (see [309, 310] and the references therein). Having evaluated the ionization equilibrium by the Khersonskii method [307], one can easily see that the abundance of such ions is extremely small at the densities, temperatures, and magnetic fields characteristic of neutron stars. Therefore, such ions do not affect the thermal spectrum.

There are rather few results on molecules composed of atoms heavier than He. We note paper [311], where the authors applied the density-functional method to calculations of binding energies of various molecules from H_n to Fe_n with n ranging from 1 through 8 at B from 10^{12} G to 2×10^{15} G. Earlier studies of heavy molecules in strong magnetic fields are discussed in [303]. All these studies assumed the model of infinitely massive atomic nuclei.

5.5 Relativistic effects

One can encounter the statement that the use of nonrelativistic quantum mechanics for calculation of atomic and molecular structure is justified only at $B < B_\mathrm{QED}$. But the treatment of the hydrogen atom in strong magnetic fields based on the Dirac equation [312–314] has not revealed any significant differences from the solution of the same problem based on the Schrödinger equation. The reasons for this are clear. We can always expand a wave function over a complete basis of two-dimensional functions, such as the set of Landau functions for all electrons. The Landau functions have the same form in relativistic and nonrelativistic theories [256]. The coefficients of such an expansion are functions of z corresponding to electron motion along **B**. This motion is nonrelativistic for bound electrons, because the maximal binding energy is much smaller than the electron rest energy $m_\mathrm{e}c^2 = 511$ keV. Therefore, the system of equations for the functions of z in question can be solved in the nonrelativistic approximation, which thus provides the accurate wave function.

Nevertheless, there is a specific relativistic effect that is not negligible in superstrong fields. As noted by Heisenberg and Euler [315], the virtual electron–positron pairs that appear in an electromagnetic field, according to the Dirac theory, modify the Maxwell equations. This effect is called vacuum polarization. It has not been observed to date, but it was discussed in many theoretical studies, and reviewed in detail in [316]. A strong electromagnetic field creates a nonzero space charge by acting on virtual pairs. Such a charge, in particular, screens the Coulomb interaction between an electron and the atomic nucleus at distances comparable to the Compton wavelength $\lambda_\mathrm{C} = 2\pi\hbar/(m_\mathrm{e}c) = 2\pi\alpha_\mathrm{f} a_\mathrm{B}$. It was noted in [317, 318] that this screening affects the even atomic levels in a superstrong magnetic field, which squeezes the atom such that its size becomes comparable to λ_C. As a result, instead of the unlimited growth of the binding energies of tightly bound states, as is predicted by the nonrelativistic theory for an unlimited increase in B, these energies ultimately level off. For the same reason, the double degeneracy of the

loosely bound states that follows from Eqn (50) at $\gamma \to \infty$ does not materialize.

This effect was thoroughly studied in [319], with the qualitative conclusions in [317, 318] confirmed and more accurate quantitative estimates obtained. In particular, according to the results in [319] (see also [284]), the effect of the vacuum polarization on the electron binding energies in a nonmoving Coulomb potential can be simulated by replacing the parameter γ with $\gamma^* = \gamma/[1 + \alpha_f^3\gamma/(3\pi)]$. As a result, the binding energy of the hydrogen atom cannot exceed 1.71 keV at any B.

5.6 Effects of a finite nuclear mass

An overwhelming majority of studies of atoms in strong magnetic fields assumed the nuclei to be infinitely massive (fixed in space). For magnetic neutron-star atmospheres, this approximation is a drastic and often undesirable simplification.

We start with an atom whose center of mass is at rest. The nucleus of a finite mass, as any charged particle, undergoes circular oscillations in the plane perpendicular to **B**. In the atom, these oscillations cannot be separated from the electron oscillations; therefore, the longitudinal projections of the orbital momenta of the electrons and the nucleus are not conserved separately: only their difference is conserved. Different atomic quantum numbers correspond to different oscillation energies of the atomic nucleus, as a multiple of its cyclotron energy. As a result, the energy of every level acquires an addition, which is not negligible if the parameter γ is not small compared to the nucleus-to-electron mass ratio. For the hydrogen atom and hydrogen-like ions, $\hbar s$ in (49) now corresponds to the difference between longitudinal projections of orbital momenta of the atomic nucleus and the electron, and the sum $N + s$ plays the role of a nuclear Landau number, with N being the electron Landau number. For bound states in strong magnetic fields, $N = 0$, and hence the nuclear oscillatory addition to the energy is $s\hbar\omega_{ci}$. Thus, the binding energy of a hydrogen atom at rest is

$$E_{sv} = E_{sv}^{(0)}(\gamma^*) - \hbar\omega_{ci}s\,, \tag{51}$$

where $\gamma^* = \gamma/(1 + 4.123 \times 10^{-8}\,\gamma)$ according to Section 5.5. It follows that the number of s values is limited for bound states. In particular, it is easy to verify using Eqns (49) and (51) that all bound states have zero momentum-to-field projection ($s = 0$) at $B > 6 \times 10^{13}$ G.

The account of the finite nuclear mass is more complicated for multielectron atoms. It was shown in [320] that the contribution of the nuclear motion to the binding energy of a nonmoving atom is $\hbar\omega_{ci}S(1 + \delta(\gamma))$, where $(-S)$ is the total magnetic quantum number and $|\delta(\gamma)| \ll 1$.

Astrophysical simulations require taking finite temperatures and hence the thermal motion of particles into account. The theory of motion of a system of point-like charges in a constant magnetic field is reviewed in [321, 322]. The canonical momentum **P** is not conserved in this motion, but a pseudomomentum **K** is conserved. The pseudomomentum of a single charged particle has a one-to-one correspondence to the position of the guiding center in the (xy) plane, perpendicular to the magnetic field, while a pseudomomentum of an atom or ion equals the sum of pseudomomenta of its constituent particles. If the system is electrically neutral as a whole, then all the components of **K** are good quantum numbers. For a charged system (an ion), K^2 is a good quantum number, while K_x and K_y do not commute. The specific effects related to the collective motion of a system of charged particles are especially important in a neutron-star atmosphere at $\gamma \gg 1$. In particular, so-called decentered states may become populated, where an electron is localized mostly in a 'magnetic well' aside from the Coulomb center.

For a hydrogen atom, $\mathbf{K} = \mathbf{P} + (e/2c)\,\mathbf{B} \times \mathbf{R}$, where the vector **R** connects the electron to the proton. Studies of this particular case were initiated in the pioneering work [323–325]. Numerical calculations of the energy spectrum of the hydrogen atom with account of the effects of motion across a strong magnetic field were performed in [326, 327]. Probabilities of various radiative transitions were studied in a series of papers ending with [258].

Figure 6 shows the energies, oscillator strengths, and photoionization cross sections of a hydrogen atom moving in a magnetic field with $\gamma = 1000$. The negative energies in Fig. 6a correspond to bound states. The reference point is taken to be the sum of the zero-point energies of a free electron and proton, $(\hbar\omega_c + \hbar\omega_{ci})/2$. At small transverse pseudomomenta $K_\perp$, the energies of low levels in Fig. 6a exceed the binding energy of the field-free hydrogen atom (1 Ry) by an order of magnitude. However, the total energy increases with increasing $K_\perp$ and can become positive for states with $s \neq 0$ due to the term $\hbar\omega_{ci}s$ in Eqn (51). Such states are metastable; in essence, they are continuum resonances. We note that the transverse atomic velocity is equal to $\partial E/\partial K$; therefore, it is maximal at the inflection points at $K_\perp = K_c$ on the curves in Fig. 6a and decreases with a further increase in $K_\perp$ [327], while the average electron–proton distance continues to increase. The atom goes into a decentered state, where the electron and proton are localized near their guiding centers, separated by the distance $r_* = (a_B^2/\hbar)\,K_\perp/\gamma$.

The dependences of the binding energies on $K_\perp$ are approximately described at $K_\perp \ll K_c$ and $K_\perp \gg K_c$ by the respective expressions

$$E_{sv}^{(<)} = E_{sv}^{(0)} - \frac{K_\perp^2}{2m_{\rm eff}} - \hbar\omega_{ci}s\,, \tag{52}$$

$$E_{sv}^{(>)} = \frac{2\,\mathrm{Ry}}{\sqrt{\hat{r}_*^2 + (2v+1)\,\hat{r}_*^{3/2} + \ldots}} - \hbar\omega_{ci}s\,, \tag{53}$$

where $\hat{r}_* \equiv r_*/a_B$, and $m_{\rm eff}$ is the effective 'transverse mass.' The latter is expressed through the values of $E_{sv}^{(0)}$ for the given and neighboring levels by the perturbation theory [328, 329]. However, for excited states, even a small inaccuracy in $E_{sv}^{(0)}$ may lead to a fatal error in $m_{\rm eff}$. Therefore, in practice, it is more convenient to use the approximation $m_{\rm eff} \approx m_a\,[1 + (\gamma/\gamma_{sv})^{p_{sv}}]$, where γ_{sv} and p_{sv} are dimensionless parameters and m_a is the true mass of the atom. For tightly bound levels, we have $\gamma_{s0} \approx 6 \times 10^3/(1 + 2s)^2$ and $p_{s0} \approx 0.9$. At $B \lesssim 10^{13}$ G, we can approximately describe the energies of states with $v = 0$ at arbitrary $K_\perp$ if we replace the ellipsis in the radicand in Eqn (53) with the expression $\hat{r}_*/(5 + 3s) + (2\,\mathrm{Ry}/E_{sv}^{(0)})^2$, and replace the inflection point K_c with the intersection of $E_{sv}^{(<)}(K_\perp)$ with $E_{sv}^{(>)}(K_\perp)$. In stronger fields or for $v \neq 0$, the transition between the centered and decentered states smears, and we have to resort to more complex fitting formulas [283].

Figure 6b shows oscillator strengths for the main dipole-allowed transitions from the ground state to excited discrete levels as functions of $K_\perp$. Since the atomic wave functions are

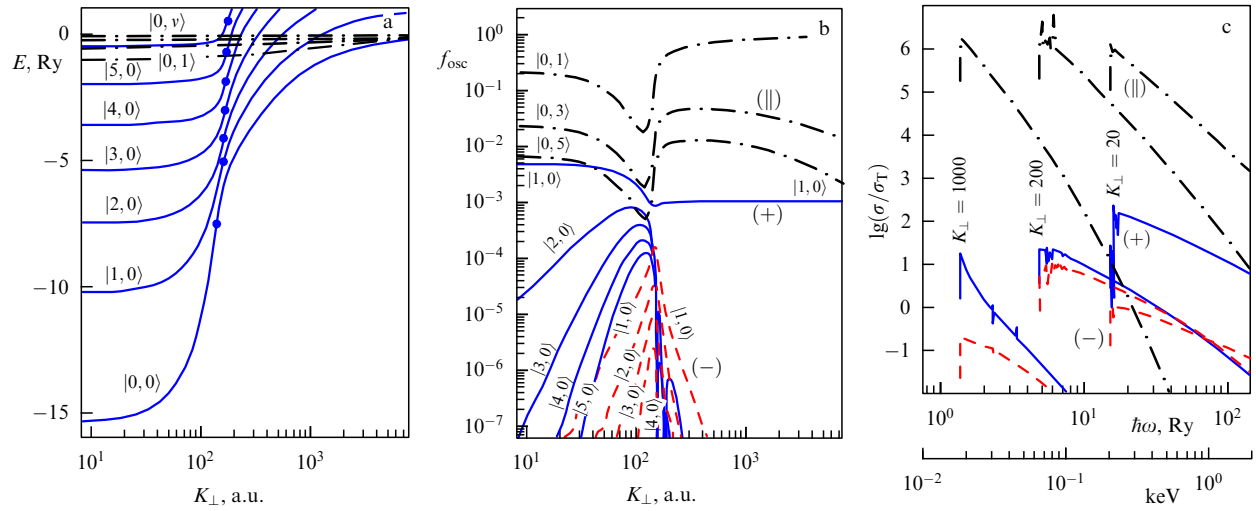

Figure 6. (Color online.) (a) Energies, (b) oscillator strengths, and (c) photoionization cross sections for a hydrogen atom moving in the magnetic field $B = 2.35 \times 10^{12}$ G. The energies of states $|s, 0\rangle$ (solid curves) and $|0, v\rangle$ (dotted-dashed curves) are shown as functions of the transverse pseudomomentum $K_\perp$ (in atomic units). The filled dots on the solid curves are the inflection points at $K_\perp = K_c$. The $K_\perp$-dependence of oscillator strengths (b) is shown for transitions from the ground state to the states $|s, 0\rangle$ under the influence of radiation with polarization $\alpha = +1$ (solid curves) and $\alpha = -1$ (dashed curves), and also for transitions into states $|0, v\rangle$ for $\alpha = 0$ (dotted-dashed curves). (c) Cross sections of photoionization under the influence of radiation with $\alpha = +1$ (solid curves), $\alpha = -1$ (dashed curves), and $\alpha = 0$ (dotted-dashed curves) are shown for the ground state as functions of the photon energy in Ry (upper x-scale) and keV (lower x-scale) at $K_\perp = 20$ a.u. (right curve), $K_\perp = 200$ a.u. (middle curve), and $K_\perp = 1000$ a.u. (left curve of every type).

symmetric with respect to the z-inversion for states with even v, and antisymmetric for odd v, only the transitions that change the parity of v are allowed for the polarization along the field ($\alpha = 0$), and only those preserving the parity are allowed for the orthogonal polarizations ($\alpha = \pm 1$). For an atom at rest, in the dipole approximation, due to the conservation of the z-projection of the total angular momentum, absorption of a photon with polarization $\alpha = 0, \pm 1$ results in changing s by α. This selection rule for a nonmoving atom manifests itself in vanishing oscillator strengths as $K_\perp \to 0$ for $s \neq \alpha$. In an appropriate coordinate system [324, 327], the symmetry is restored as $K_\perp \to \infty$; therefore, the transition with $s = \alpha$ is the only one that also survives in the limit of large pseudomomenta. But in the intermediate region of $K_\perp$, where the transverse atomic velocity is not small, the cylindrical symmetry is broken, and hence transitions to other levels are allowed. For example, the corresponding oscillator strengths in Fig. 6b have maxima at $K_\perp \approx K_c$. Analytic approximations for these oscillator strengths are given in [283].

Figure 6c shows photoionization cross sections for hydrogen in the ground state as functions of the photon energy at three values of $K_\perp$. The leftward shift of the ionization threshold with increasing $K_\perp$ corresponds to a decrease in the binding energy that is shown in Fig. 6a, while the peaks and dips on the curves are caused by resonances at transitions to metastable states $|s, \nu; K\rangle$ with positive energies (see [258] for a detailed discussion).

Quantum mechanical calculations of the characteristics of the He^+ ion that moves in a strong magnetic field are performed in [330, 331]. The basic difference from the case of a neutral atom is that the ion motion is restricted by the field in the transverse plane, and therefore the values of K^2 are quantized [321, 322]. Clearly, the similarity relations for ions with nonmoving nuclei (Section 5.3) do not hold anymore.

Currently, there is no detailed calculation of binding energies, oscillator strengths, or photoionization cross sections for atoms and ions other than H and He^+, arbitrarily moving in a strong magnetic field. For such species, the decentered states are usually neglected and the perturbation theory with respect to $K_\perp$ is typically used [328, 329]. Such an approach was realized, for example, in [297, 301]. This can be sufficient for simulations of relatively cool atmospheres of moderately magnetized neutron stars. Detailed conditions of the applicability of the perturbation theory [328, 329] require calculations, but a rough order-of-magnitude estimate can be obtained by requiring that the mean Lorentz force acting on a bound electron because of the atomic thermal motion be small compared to the Coulomb forces. As a result, for an atom with the mass $m_a = Am_u$, we obtain the condition $k_B T/E_b \ll m_a/(\gamma m_e) \approx 4A/B_{12}$, where E_b is the atomic ionization energy. If $B \lesssim 10^{13}$ G and $T \lesssim 10^6$ K, it is well satisfied for low-lying levels of carbon and heavier atoms.

5.7 Equation of state

A theoretical description of the thermodynamics of partially ionized plasmas can be based on either 'physical' or 'chemical' models (see, e.g., a discussion and the references in [332, 333]). In the chemical model of plasmas, bound states (atoms, molecules, ions) are treated as separate members of the thermodynamic ensemble, while in the physical model, the only members of the ensemble are atomic nuclei and electrons. Each of the models can be thermodynamically self-consistent, but the physical model is more relevant from the microscopic standpoint, because it does not require distinguishing the electrons bound to a given nucleus. Such a distinction becomes very ambiguous at high densities, where several nuclei can attract the same electron with comparable forces. On the other hand, calculations in the framework of the physical model are technically more complicated. As a rule, they are based on a diagram expansion, which requires an increase in the number of terms with a density increase. For this reason, even the most advanced equation of state for nonmagnetic photospheres that is based on the physical model [334] is still restricted to the range $\rho \lesssim 10\, T_6^3$ g cm^{-3}.

Studies of magnetic neutron-star photospheres are typically based on the chemical plasma model. The ionization equilibrium is then evaluated by minimizing the Helmholtz free energy F, given by

$$F = F_{\rm id}^{(\rm e)} + F_{\rm id}^{(\rm i)} + F_{\rm int} + F_{\rm ex}\,, \tag{54}$$

where $F_{\rm id}^{(\rm e)}$ and $F_{\rm id}^{(\rm i)}$ describe the ideal electron and ion gases, $F_{\rm int}$ includes internal degrees of freedom for bound states, and $F_{\rm ex}$ is a nonideal component. All thermodynamic functions that are required for modeling the photosphere with a given chemical composition are expressed through derivatives of F over ρ and T [335].

According to the Bohr–van Leeuwen theorem,[9] a magnetic field does not affect the thermodynamics of classical charged particles. The situation is different in quantum mechanics. The importance of quantum effects depends on the parameters $\zeta_{\rm e}$ in (40) and $\zeta_{\rm i}$ in (41).

We use the equality $F_{\rm id}^{(\rm e)}/V = \mu_{\rm e} n_{\rm e} - P_{\rm id}^{(\rm e)}$ [335], where V is the volume of the system and $\mu_{\rm e}$, $n_{\rm e}$, and $P_{\rm id}^{(\rm e)}$ are the chemical potential, number density, and pressure in the ideal electron gas model. The equation of state is determined by a relation between these quantities, which can be found from the relations (e.g., [1, 90])

$$\left\{ \begin{array}{c} n_{\rm e} \\ P_{\rm id}^{(\rm e)} \end{array} \right\} = \sum_{N,\sigma} \frac{(1+2bN)^{1/4}}{\pi^{3/2} a_{\rm m}^2 \lambda_{\rm e}} \left\{ \begin{array}{c} \partial I_{1/2}(\chi_N, \tau_N) \\ \hline \partial \chi_N \\ k_{\rm B} T I_{1/2}(\chi_N, \tau_N) \end{array} \right\}, \tag{55}$$

where $\lambda_{\rm e} = [2\pi\hbar^2/(m_{\rm e} k_{\rm B} T)]^{1/2}$ is the thermal de Broglie wavelength, $\tau_N = k_{\rm B} T/(m_{\rm e} c^2 \sqrt{1+2bN})$, $\chi_N = \mu_{\rm e}/(k_{\rm B} T) + \tau_0^{-1} - \tau_N^{-1}$,

$$I_{1/2}(\chi_N, \tau_N) \equiv \int_0^\infty \frac{\sqrt{x\,(1+\tau_N x/2)}}{\exp(x-\chi_N)+1}\,{\rm d}x \tag{56}$$

is the Fermi–Dirac integral, and the summation ranges all N and all values of spin projections on the magnetic field, $\hbar\sigma/2$, such that $\sigma = \pm 1$ for positive N and $\sigma = -1$ at $N = 0$.

In a strongly quantizing magnetic field, it is sufficient to keep only the term with $N = 0$ in sums (55). In this case, the electron Fermi momentum is $p_{\rm F} = 2\pi^2 a_{\rm m}^2 \hbar n_{\rm e}$. Therefore, with increasing $n_{\rm e}$ at a fixed B, the degenerate electrons begin to fill the first Landau level when $n_{\rm e}$ reaches $n_B = (\pi^2\sqrt{2}\, a_{\rm m}^3)^{-1}$. This value just corresponds to the density ρ_B in Eqn (39). The ratio of the Fermi momentum $p_{\rm F}$ in the strongly quantizing field to its nonmagnetic value $\hbar(3\pi^2 n_{\rm e})^{1/3}$ is $[4\rho^2/(3\rho_B^2)]^{1/3}$. Therefore, the Fermi energy at a given density $\rho < \sqrt{3/4}\,\rho_B$ decreases with increasing B, that is, a strongly quantizing magnetic field relieves the electron-gas degeneracy. For this reason, strongly magnetized neutron-star photospheres remain mostly nondegenerate, as they were in the absence of the field, despite their densities being orders of magnitude higher than the nonmagnetic photosphere densities.

The free energy of nondegenerate nonrelativistic ions is given by

$$\frac{F_{\rm id}^{(\rm i)}}{N_{\rm i} k_{\rm B} T} = \ln\left(2\pi\,\frac{n_{\rm i}\lambda_{\rm i} a_{\rm m}^2}{Z}\right) + \ln\left[1-\exp(-\zeta_{\rm i})\right] - 1 + \frac{\zeta_{\rm i}}{2} + \ln\left(\frac{\sinh\left[g_{\rm i}\,\zeta_i(2s_{\rm i}+1)/4\right]}{\sinh(g_{\rm i}\,\zeta_{\rm i}/4)}\right), \tag{57}$$

where $\lambda_{\rm i} = [2\pi\hbar^2/(m_{\rm i} k_{\rm B} T)]^{1/2}$ is the thermal de Broglie wavelength for the ions, $s_{\rm i}$ is the spin number, and $g_{\rm i}$ is the spin-related g-factor (for instance, $s_{\rm i} = 1/2$ and $g_{\rm i} = 5.5857$ for a proton). All the terms in (57) have clear physical meanings. As $\zeta_{\rm i} \to 0$, the first and second terms together give $\ln(n_{\rm i}\lambda_{\rm i}^3)$, which corresponds to a three-dimensional Boltzmann gas. The first term corresponds to the one-dimensional Boltzmann gas model at $\zeta_{\rm i} \gg 1$. The second-to-last term in (57) gives the total energy $N_{\rm i}\hbar\omega_{\rm ci}/2$ of zero-point oscillations transverse to the magnetic field. Finally, the last term represents the energy of magnetic moments in a magnetic field.

The nonideal free-energy part $F_{\rm ex}$ contains the Coulomb and exchange contributions of electrons and ions, and the electron–ion polarization energy. In the case of incomplete ionization, $F_{\rm ex}$ also includes interactions of ions and electrons with atoms and molecules. In turn, the interaction between the ions is described differently depending on the phase state of matter. The terms that constitute $F_{\rm ex}$ depend on the magnetic field only if it quantizes the motion of these interacting particles. Here, we do not discuss these terms, but refer the interested reader to [90] and the references therein. This nonideality is negligible in neutron-star atmospheres, but it determines the formation of a condensed surface, which will be considered in Section 5.10.

5.8 Ionization equilibrium

For photosphere simulations, it is necessary to determine the fractions of different bound states, because they affect the spectral features that are caused by bound–bound and bound–free transitions. The solution of this problem is laborious and ambiguous. The main difficulty in the chemical plasma model, namely, the necessity of distinguishing the bound and free electrons and 'attributing' the bound electrons to certain nuclei, becomes especially acute at high densities, where the atomic sizes cannot be neglected anymore compared to their distances. Current approaches to the solution of this problem are based, as a rule, on the concept of so-called occupation probabilities of quantum states. For example, we consider electrons in thermodynamic equilibrium with ions of the Zth chemical element, and let j be the ionization degree of every ion (i.e., the number of electrons removed), κ be its quantum state, and $E_{j,\kappa}$ and $g_\kappa^{(j)}$ be its binding energy and statistical weight. The occupation probability $w_{j,\kappa}$ is an additional statistical weight of the given state under the condition of plasma nonideality, that is, in the case of interaction of the ion (Z, j, κ) with surrounding particles, compared with its weight without such interactions.[10] As first noted by Fermi [337], the occupation probabilities $w_{j,\kappa}$ cannot be arbitrary but should be consistent with $F_{\rm ex}$. Minimizing F with the Landau quantization taken into account leads to a system of ionization–equilibrium equations for $n_j \equiv \sum_\kappa n_{j,\kappa}$ [338, 339],

$$\frac{n_j}{n_{j+1}} = \frac{n_{\rm e}\lambda_{\rm e}^3}{2}\,\frac{\sinh\zeta_j}{\zeta_j}\,\frac{\zeta_{j+1}}{\sinh\zeta_{j+1}}\,\frac{\tanh\zeta_{\rm e}}{\zeta_{\rm e}}\,\frac{\mathcal{Z}_{{\rm int},\,j}}{\mathcal{Z}_{{\rm int},\,j+1}}\,\exp\frac{E_{j,\,\rm ion}}{k_{\rm B} T}\,, \tag{58}$$

where $\mathcal{Z}_{{\rm int},\,j} = \sum_\kappa g_\kappa^{(j)}\, w_{j,\kappa}\, \exp\left[(E_{j,\kappa} - E_{j,\,\rm gr.st})/(k_{\rm B} T)\right]$ is the internal partition function of the jth ion type, $E_{j,\,\rm gr.st}$ is its ground-state binding energy, $E_{j,\,\rm ion} = E_{j,\,\rm gr.st} - E_{j+1,\,\rm gr.st}$ is its

[9] This theorem was proved by different methods in PhD theses by Niels Bohr in 1911 and H-J van Leeuwen in 1919, published by the latter in 1921 [336].

[10] This ratio is not necessarily less than unity; thus, the term 'probability' is not quite correct, but we adhere to the traditional terminology.

ionization energy, and ζ_j is magnetic quantization parameter (41). Equation (58) differs from the usual Saha equation, first, by the terms with ζ_e and ζ_j, which are the partition functions for distributions of free electrons and ions over the Landau levels, and second, by the occupation probabilities $w_{j,\kappa}$ in the expressions for the partition functions $\mathcal{Z}_{\mathrm{int},j}$.

There have been many attempts to find such an approximation for the occupation probabilities that best reproduced the real plasma EOS. They were discussed, for example, by Hummer and Mihalas [340], who proposed an approximation based on the Inglis–Teller criterion [341] for dissolution of spectral lines because of their smearing due to the Stark shifts in plasma microfields. However, the migration of a spectroscopic criterion to thermodynamics is not well grounded. It is necessary to clearly distinguish between the disappearance of the spectral lines of an atom and the complete destruction of this atom with increasing pressure, as was stressed, for instance, in [342–344]. To take this difference into account, in [345] we introduced a concept of optical occupation probabilities $\tilde{w}_{j,\kappa}$, which resemble the Hummer–Mihalas occupation probabilities and should be used for the calculation of spectral opacities, but differ from the thermodynamic occupation probabilities $w_{j,\kappa}$ that are used in the EOS calculations.

Equation (58) has been applied to modeling partially ionized atmospheres of neutron stars, composed of iron, oxygen, and neon [339, 346–348]. The effects related to the finite nuclear masses (Section 5.6) were either ignored or treated in the first order of the perturbation theory. Since quantum mechanical characteristics of an atom in a strong magnetic field depend on the transverse pseudomomentum $K_\perp$, the atomic distribution over $K_\perp$ cannot be written in a closed form, and only the distribution over longitudinal momenta K_z remains Maxwellian. The first complete account of these effects was taken in [349] for hydrogen photospheres. Let $p_{sv}(K_\perp)\,\mathrm{d}^2K_\perp$ be the probability of finding a hydrogen atom in the state $|s,v\rangle$ in the element $\mathrm{d}^2K_\perp$ near $\mathbf{K}_\perp$ in the plane of transverse pseudomomenta. Then the number of atoms in the element d^3K of the pseudomomentum space equals

$$\mathrm{d}N(\mathbf{K}) = N_{sv}\,\frac{\lambda_a}{2\pi\hbar}\exp\left(-\frac{K_z^2}{2m_a k_B T}\right)p_{sv}(K_\perp)\,\mathrm{d}^3K, \qquad (59)$$

where m_a is the mass of the atom, $\lambda_a = [2\pi\hbar^2/(m_a k_B T)]^{1/2}$ is its thermal wavelength, and $N_{sv} = \int \mathrm{d}N_{sv}(\mathbf{K})$ is the total number of atoms with given discrete quantum numbers. The distribution $N_{sv}p_{sv}(K_\perp)$ is not known in advance, but should be calculated in a self-consistent way while minimizing the free energy including the nonideal terms. It is convenient to define deviations from the Maxwell distribution with the use of generalized occupation probabilities $w_{sv}(K_\perp)$. Then the atomic contribution $(F_{\mathrm{id}} + F_{\mathrm{int}})$ to the free energy is [349]

$$k_B T\sum_{sv} N_{sv}\int \ln\left[n_{sv}\lambda_a^3\,\frac{w_{sv}(K_\perp)}{\exp(1)\,\mathcal{Z}_{sv}}\right]p_{sv}(K_\perp)\,\mathrm{d}^2K_\perp, \qquad (60)$$

where

$$\mathcal{Z}_{sv} = \frac{\lambda_a^2}{2\pi\hbar^2}\int_0^\infty w_{sv}(K_\perp)\exp\left(\frac{E_{sv}(K_\perp)}{k_B T}\right)K_\perp\,\mathrm{d}K_\perp. \qquad (61)$$

The nonideal part of the free energy that describes atom–atom and atom–ion interactions and is responsible for the pressure ionization has been calculated in [349] with the use of the hard-sphere model. The plasma model also included hydrogen molecules H_2 and chains H_n, which become stable in strong magnetic fields. For this purpose, approximate formulas of Lai [303] have been used, which do not fully take the motion effects into account; therefore, the results in [349] are reliable only when the molecular fraction is small.

This hydrogen-plasma model underlies thermodynamic calculations of hydrogen photospheres of neutron stars with strong [266] and superstrong [350] magnetic fields.[11] In [308], the same approach was applied with slight modifications to strongly magnetized helium plasmas. One of the modifications was the use of the plasma microfield distribution in [226] to calculate $w(K_\perp)$. Atomic and molecular helium states of different ionization degrees were considered in [308]. The rotovibrational molecular levels were treated by the perturbation theory and the orientation of the molecular axis relative to **B** was taken into account. The $K_\perp$-dependence of the energy $E(K_\perp)$ was described by an analytic fit based on an extrapolation of adiabatic calculations at small $K_\perp$. The motional effects of atomic and molecular ions were not considered.

5.9 Applicability of the LTE approximation

The models of the EOS and ionization balance usually assume that the LTE conditions are satisfied for atoms and ions. In particular, the Boltzmann distribution over the Landau levels is assumed. This assumption does not apply to free electrons in neutron-star atmospheres if the spontaneous radiative decay rate of excited Landau levels,

$$\Gamma_r = \frac{4}{3}\,\frac{e^2\omega_c^2}{m_e c^3} = 3.877\times10^{15}B_{12}^2\ \mathrm{s}^{-1}, \qquad (62)$$

exceeds the rate of their collisional deexcitation.

In a nonquantizing field, the characteristic frequency of electron–ion Coulomb collisions is (see, e.g., [351])

$$\Gamma_c = \frac{4\sqrt{2\pi}\,n_i Z^2 e^4\Lambda_c}{3\sqrt{m_e}\,(k_B T)^{3/2}} = 2.2\times10^{15}\,\frac{Z^2}{A}\,\frac{\rho'\Lambda_c}{T_6^{3/2}}\ \mathrm{s}^{-1}, \qquad (63)$$

where $\rho' \equiv \rho/(\mathrm{g\,cm^{-3}})$, and Λ_c is a Coulomb logarithm, which weakly depends on T and ρ and usually has an order of magnitude of 1 – 10. In a quantizing field, the electrons are deexcited from the first Landau level by electron–ion Coulomb collisions at the rate

$$\Gamma_{10} = \frac{4\sqrt{2\pi}\,n_i Z^2 e^4\tilde{\Lambda}_{10}}{\sqrt{m_e}\,(\hbar\omega_c)^{3/2}} = 4.2\times10^{12}\,\frac{Z^2}{A}\,\frac{\rho'\tilde{\Lambda}_{10}}{B_{12}^{3/2}}\ \mathrm{s}^{-1}$$
$$= 4.9\times10^{13}\,\frac{Z^2}{A}\,\frac{\rho'\Lambda_{10}}{B_{12}\sqrt{T_6}}\ \mathrm{s}^{-1}, \qquad (64)$$

where $\tilde{\Lambda}_{10} = \sqrt{\zeta_e}\,\Lambda_{10}$ is a new Coulomb logarithm, which has an order of unity at $\zeta_e \gg 1$, whereas Λ_{10} has that order at $\zeta_e \ll 1$ [268]. We note that the rate of the inverse process of collisional excitation is $\Gamma_{01} = \Gamma_{10}\exp(-\zeta_e)$. Comparing (62) and (64), we see that in the weak-field ($B \lesssim 10^{10}$ G) photospheres of isolated neutron stars, where typically $\rho \gtrsim 10^{-3}$ g cm^{-3} and $T_6 \approx 1$, the LTE conditions are fulfilled (this may not be the case in the magnetosphere due to the

[11] Some results of these calculations are available at http://www.ioffe.ru/astro/NSG/Hmagnet/.

lower densities). In stronger fields ($B \gtrsim 10^{11}$ G), the LTE is violated, and the fraction of electrons on the excited Landau levels is lower than the Boltzmann value $\exp(-\zeta_e)$. However, this does not entail any consequence for the atmosphere models because $\exp(-\zeta_e)$ is vanishingly small there.

For ions, the spontaneous decay rate of the excited Landau levels Γ_{ri} differs from Γ_r by the factor $Z(Zm_e/m_i)^3 \sim 10^{-10}$. The statistical distribution of ions over the Landau levels has been studied in [268]. The authors showed that the fraction of ions on the first excited Landau level is accurately given by

$$\frac{n_1}{n_0} = \exp(-\zeta_i)\,\frac{1+\epsilon\,(\Gamma_{ri}/\Gamma_{10,i})/\left[1-\exp(-\zeta_i)\right]}{1+\Gamma_{ri}/\Gamma_{10,i}+\epsilon\,(\Gamma_{ri}/\Gamma_{10,i})/\left[\exp(\zeta_i)-1\right]}\,, \tag{65}$$

where $\epsilon = J_\omega/\mathcal{B}_{\omega,T}$ at $\omega = \omega_{ci}$, and $\Gamma_{10,i}$ is the collisional frequency of the first level, which differs from Eqn (64) by the factor $\sqrt{m_i/m_e}$ and the value of the Coulomb logarithm. The parameter ϵ is small in the outer layers of the photospheres and therefore the distribution over the levels is determined by the ratio $\Gamma_{ri}/\Gamma_{10,i}$. If $\Gamma_{ri}/\Gamma_{10,i} \ll 1$, then the Boltzmann distribution is recovered, that is, the LTE approximation holds; otherwise, the excited levels are underpopulated. According to [268],

$$\frac{\Gamma_{10,i}}{\Gamma_{ri}} \sim \frac{\rho'}{(B_{12}/300)^{7/2}}\,. \tag{66}$$

In the atmospheres and on the radiating surfaces of ordinary neutron stars, this ratio is large because the denominator is small, and for magnetars with $B \lesssim 10^{15}$ G, the ratio is large because ρ' is large [see (22)]. Moreover, as shown in [268], even in the outer atmospheres of magnetars, where $\Gamma_{ri}/\Gamma_{10,i} \ll 1$, deviations from the LTE should not affect the spectral modeling. The reason is that absorption coefficients are mainly determined by second-order quantum transitions that do not change the Landau number N. Therefore, the depletion of the upper states is unimportant, and hence the Kirchhoff law, which holds at the LTE, remains approximately valid also in this case.

5.10 Condensed surface

It was suggested in [352] that a strong magnetic field can stabilize polymer chains directed along the field lines and that the dipole–dipole attraction of these chains may result in a condensed phase. Later studies have shown that such chains indeed appear in the fields $B \sim 10^{12}-10^{13}$ G, but only for chemical elements lighter than oxygen, and they polymerize into a condensed phase either in superstrong fields or at relatively low temperatures, the sublimation energy being much smaller than those assumed in [352] (see [353] and the references therein).

From the thermodynamics standpoint, the magnetic condensation is nothing but the plasma phase transition caused by a strong electrostatic attraction between the ionized plasma particles. This attraction makes a negative contribution to the pressure P_{ex}, which is not counterbalanced at low temperatures (at $\Gamma_{Coul} \gtrsim 1$) until the electrons become degenerate with increasing density. In the absence of a magnetic field, such phase transitions have been studied theoretically since the 1930s (see [354] for a review). In this case, the temperature of the outer layers of a neutron star $T \gtrsim (10^5-10^6)$ K exceeds the critical temperature T_{crit} for the plasma phase transition. However, we have seen in Section 5.7 that a quantizing magnetic field lifts the electron degeneracy. As a result, T_{crit} increases with increasing B, which may enable such a phase transition.

The condensed-surface density was estimated in [303] as

$$\rho_s \approx 561\,\eta\,AZ^{-3/5}B_{12}^{6/5}\ \mathrm{g\,cm^{-3}}\,, \tag{67}$$

where η is an unknown factor of the order of unity. In the ion sphere model [355], the electrons are replaced by a uniform negative background and the potential energy per ion is estimated as the electrostatic energy of the ionic interaction with the negative background contained in a sphere of the radius $a_i = (4\pi n_i/3)^{-1/3}$. By equating $|P_{ex}|$ to the pressure of degenerate electrons P_e, we obtain Eqn (67) with $\eta = 1$. This estimate disregards the ion correlation effects, the electron–gas polarizability, and the bound-state formation. Taking the electron polarization into account by different versions of the Thomas–Fermi method yields different results: for example, the zero-temperature Thomas–Fermi data for magnetized iron at 10^{10} G $\leqslant B \leqslant 10^{13}$ G [356] can be described by Eqn (67) with $\eta \approx 0.2+0.01/B_{12}^{0.56}$, and in a finite-temperature Thomas–Fermi model [357], there is no phase transition at all.

At $1 \lesssim B_{12} \lesssim 10^3$, the EOS of partially ionized, strongly magnetized hydrogen [349] that was described in Section 5.8 predicts a phase transition with the critical temperature $T_{crit} \approx 3\times10^5\,B_{12}^{0.39}$ K and the critical density $\rho_{crit} \approx 143 B_{12}^{1.18}$ g cm^{-3}, which corresponds to $\eta \approx 1/4$. With decreasing the temperature below T_{crit}, the condensed-phase density increases and tends asymptotically to that in Eqn (67) with $\eta \approx 1/2$, while the density of the gaseous phase rapidly decreases, and the atmosphere becomes optically thin. The same qualitative results were derived in [358] from calculations of the density of saturated vapor above the condensed surface, but the T_{crit} values obtained were in the range $1/4-1/3$ of the above estimate. The quantitative differences may be caused by the less accurate approximate treatment of the molecular contribution in [349], on the one hand, and by the less accurate account of the effects of atomic motion across the magnetic field in [358], on the other hand.

The condensation energy was discussed in [353] within the density functional method. In [359], the equilibrium density of a saturated vapor of the atoms and polymer chains of helium, carbon, and iron above the respective condensed surfaces was calculated for $1 \lesssim B_{12} \leqslant 10^3$. By equating this density to ρ_s, T_{crit} was found at several B values. Unlike previous authors, Medin and Lai [353, 359] self-consistently took the electron band structure in the condensed phase into account. But they did not include the effects of atomic and molecular motion across the magnetic field in the gaseous phase and rather roughly included the excited-state contribution. They calculated the condensed-surface density assuming that the linear atomic chains, being unchanged as such, form a rectangular lattice in the plane perpendicular to **B**. As shown in [90], such estimated values of ρ_s can be described by Eqn (67) with $\eta = 0.517 + 0.24/B_{12}^{1/5} \pm 0.011$ for carbon and $\eta = 0.55 \pm 0.11$ for iron, and the critical temperature can be evaluated as $T_{crit} \sim 5\times10^4\,Z^{1/4}\,B_{12}^{3/4}$ K. For comparison, in the fully ionized plasma model, $T_{crit} \approx 2.5\times10^5\,Z^{0.85}\,B_{12}^{0.4}$ K and $\eta = [1+1.1\,(T/T_{crit})^5]^{-1}$. Hopefully, the existing uncertainty in estimates of ρ_s and T_{crit} may be diminished by analyzing future neutron-star observations.

When the magnetic field increases from 10^{12} G to 10^{15} G, the cohesive energy calculated in [359] for the condensed surface varies monotonically from 0.07 keV to 5 keV for

helium, from 0.05 keV to 20 keV for carbon, and from 0.6 keV to 70 keV for iron. The power-law interpolation gives order-of-magnitude estimates between these limits. The electron work function changes in the same B range from 100 eV to (600 ± 50) eV. With the calculated energy values, the authors of [359] determined the conditions of electron and ion emission in the vacuum gap above the polar cap of a pulsar and the conditions of gap formation, and calculated the pulsar death lines on the $\mathcal{P}-\dot{\mathcal{P}}$ plane.

6. Magnetic atmospheres

6.1 Radiative transfer in normal modes

Propagation of electromagnetic waves in magnetized plasmas has been the subject of many studies, the book by Ginzburg [189] being the most complete of them. At a radiation frequency ω much larger than the electron plasma frequency $\omega_{\rm pe} = (4\pi e^2 n_{\rm e}/m_{\rm e}^*)^{1/2}$, where $m_{\rm e}^* \equiv m_{\rm e}[1 + p_{\rm F}^2/(m_{\rm e}c)^2]^{1/2}$ is the effective dynamic mass of an electron on the Fermi surface, the waves propagate in the form of two polarization modes, extraordinary (hereafter denoted by the subscript or superscript $j = 1$ or X) and ordinary ($j = 2$ or O). They have different polarization vectors $\mathbf{e}^j$ and different absorption and scattering coefficients, which depend on the angle θ_B (Fig. 1). The modes interact with one another via scattering. A physical analysis of the polarization modes in application to neutron stars was performed in [260]. The radiative transfer problem was set up in terms of these modes in [360]. In strongly magnetized neutron-star atmospheres, at any frequencies outside narrow frequency ranges near resonances, strong Faraday depolarization was shown to occur. In this case, it is sufficient to consider the specific intensities of the two normal modes instead of the four components of the Stokes vector. The radiative transfer equation for these specific intensities is a direct generalization of Eqn (27) [261]:

$$\cos\theta_k \, \frac{{\rm d}I_{\omega,j}(\hat{\mathbf{k}})}{{\rm d}y_{\rm col}} = \varkappa_{\omega,j}(\hat{\mathbf{k}})\, I_{\omega,j}(\hat{\mathbf{k}}) - \frac{1}{2}\,\varkappa^{\rm a}_{\omega,j}(\hat{\mathbf{k}})\, \mathcal{B}_{\omega,T} - \sum_{j'=1}^{2} \int_{(4\pi)} \varkappa^{\rm s}_{\omega,j'j}(\hat{\mathbf{k}}', \hat{\mathbf{k}})\, I_{\omega,j'}(\hat{\mathbf{k}}')\, {\rm d}\hat{\mathbf{k}}' , \tag{68}$$

where

$$\varkappa_{\omega,j}(\hat{\mathbf{k}}) \equiv \varkappa^{\rm a}_{\omega,j}(\hat{\mathbf{k}}) + \sum_{j'=1}^{2} \int_{(4\pi)} \varkappa^{\rm s}_{\omega,j'j}(\hat{\mathbf{k}}', \hat{\mathbf{k}})\, {\rm d}\hat{\mathbf{k}}' .$$

The dependence of the opacities $\varkappa$ on the ray directions $(\hat{\mathbf{k}}, \hat{\mathbf{k}}')$ is affected by the magnetic-field direction. Therefore, the emission of a magnetized atmosphere, unlike the nonmagnetic one, depends not only on the angle θ_k that determines the ray inclination to the stellar surface but also on the angles θ_n and φ_k in Fig. 1. For the hydrostatic and energy balance, we can keep Eqns (28), (29), and (32), if we set $I_\omega = \sum_{j=1}^{2} I_{\omega,j}$ by definition.

The diffusion equation for the normal modes in these approximations was derived in [261, 361]. For a plane-parallel photosphere, it is [116]

$$\frac{\rm d}{{\rm d}y_{\rm col}}\, D_{\omega,j}\, \frac{\rm d}{{\rm d}y_{\rm col}}\, J_{\omega,j} = \bar{\varkappa}^{\rm a}_{\omega,j} \left[J_{\omega,j} - \frac{\mathcal{B}_{\omega,T}}{2} \right] + \bar{\varkappa}^{\rm s}_{\omega,12} [J_{\omega,j} - J_{\omega,3-j}] , \tag{69}$$

where

$$J_{\omega,j} = \frac{1}{4\pi} \int_{(4\pi)} I_{\omega,j}(\hat{\mathbf{k}})\, {\rm d}\hat{\mathbf{k}} ,$$

$$\bar{\varkappa}^{\rm a}_{\omega,j} = \frac{1}{4\pi} \int_{(4\pi)} \varkappa^{\rm a}_{\omega,j}\, {\rm d}\hat{\mathbf{k}} ,$$

$$\bar{\varkappa}^{\rm s}_{\omega,12} = \frac{1}{4\pi} \int_{(4\pi)} {\rm d}\hat{\mathbf{k}}' \int_{(4\pi)} {\rm d}\hat{\mathbf{k}}\, \varkappa^{\rm s}_{\omega,12}(\hat{\mathbf{k}}', \hat{\mathbf{k}}) ,$$

and the effective diffusion coefficient is

$$D_{\omega,j} = \frac{1}{3\varkappa^{\rm eff}_{\omega,j}} = \frac{\cos^2\theta_n}{3\varkappa^{\parallel}_{\omega,j}} + \frac{\sin^2\theta_n}{3\varkappa^{\perp}_{\omega,j}} , \tag{70}$$

where θ_n is the angle between $\mathbf{B}$ and the intensity gradient and

$$\begin{Bmatrix} (\varkappa_j^{\parallel})^{-1} \\ (\varkappa_j^{\perp})^{-1} \end{Bmatrix} = \frac{3}{4} \int_0^{\pi} \begin{Bmatrix} 2\cos^2\theta_B \\ \sin^2\theta_B \end{Bmatrix} \frac{\sin\theta_B\, {\rm d}\theta_B}{\varkappa_j(\theta_B)} . \tag{71}$$

The effective opacity for nonpolarized radiation is $\varkappa^{\rm eff} = 2/(3D_{\omega,1} + 3D_{\omega,2})$. Diffusion approximation (69) serves as a starting point in an iterative method [362], which allows solving system (68) more accurately.

6.2 Plasma polarizability

In the Cartesian coordinate system with the z axis directed along $\mathbf{B}$, the plasma dielectric tensor is [189]

$$\boldsymbol{\varepsilon} = \mathbf{I} + 4\pi\chi = \begin{pmatrix} \varepsilon_\perp & {\rm i}\varepsilon_\wedge & 0 \\ -{\rm i}\varepsilon_\wedge & \varepsilon_\perp & 0 \\ 0 & 0 & \varepsilon_{\parallel} \end{pmatrix} , \tag{72}$$

where $\mathbf{I}$ is the unit tensor, $\chi = \chi^{\rm H} + {\rm i}\chi^{\rm A}$ is the complex polarizability tensor of plasma, and $\chi^{\rm H}$ and $\chi^{\rm A}$ are its Hermitian and anti-Hermitian parts. Under the assumption that the electrons and ions lose their regular velocity acquired in an electromagnetic wave by collisions with an effective frequency $\nu_{\rm eff}$ independent of the velocities, the cyclic components of the polarizability tensor are ([189], § 10)

$$\chi_\alpha = -\frac{1}{4\pi}\, \frac{\omega_{\rm pe}^2}{(\omega + \alpha\omega_{\rm c})\,(\omega - \alpha\omega_{\rm ci}) + {\rm i}\omega\nu_{\rm eff}} \tag{73}$$

($\alpha = 0, \pm 1$). A more rigorous kinetic theory leads to results that cannot be described by Eqn (73) with the same frequency $\nu_{\rm eff}$ for the Hermitian and anti-Hermitian components $\chi_\alpha^{\rm H}$ and $\chi_\alpha^{\rm A}$ ([189], § 6).

The anti-Hermitian part of the polarizability tensor determines the opacities: $\varkappa_\alpha(\omega) = 4\pi\omega\chi_\alpha^{\rm A}(\omega)/(\rho c)$. Then the Kramers–Kronig relation gives [363, 364]

$$\chi_\alpha^{\rm H}(\omega) = \frac{c\rho}{4\pi^2\omega} \left\{ \int_0^{\omega} \left[\varkappa_\alpha(\omega + \omega') - \varkappa_\alpha(\omega - \omega') \right] \frac{{\rm d}\omega'}{\omega'} + \int_{2\omega}^{\infty} \frac{\varkappa_\alpha(\omega')}{\omega' - \omega}\, {\rm d}\omega' - \int_0^{\infty} \frac{\varkappa_{-\alpha}(\omega')}{\omega' + \omega}\, {\rm d}\omega' \right\} . \tag{74}$$

Thus, we can calculate the polarizability tensor $\boldsymbol{\chi}$ from the opacities $\varkappa_\alpha(\omega)$. This has been done in [363] for a gas of neutral hydrogen atoms and in [364] for partially ionized hydrogen plasmas.

Figure 7 shows the cyclic components of absorption coefficients, $\mu_\alpha = \rho\varkappa_\alpha$ in the top panel, and the corresponding polarizability components $\chi_\alpha^{\rm H}$ in the middle and bottom

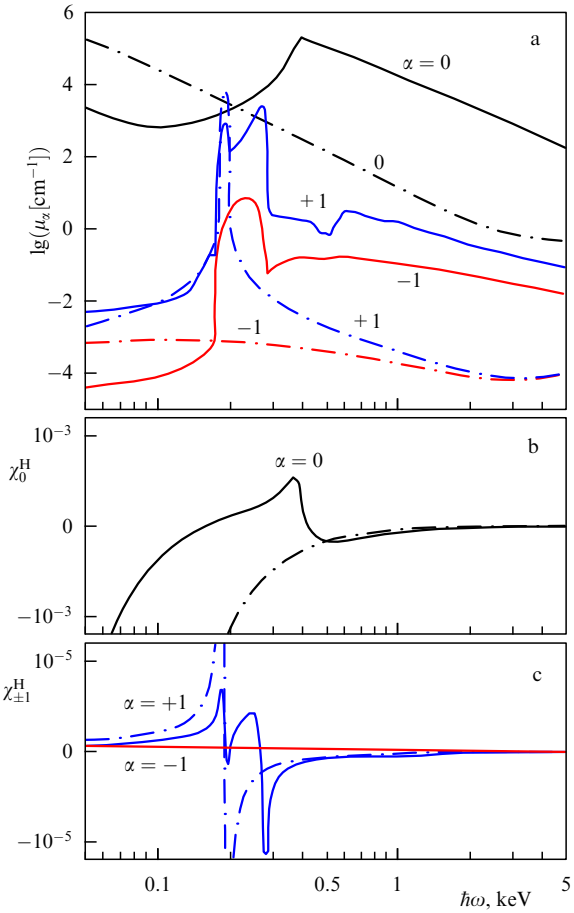

Figure 7. (a) Absorption coefficients and polarizability coefficients (b) χ_0^{H} and (c) $\chi_{\pm1}^{\mathrm{H}}$ in partially ionized (solid curves) and fully ionized (dotted-dashed curves) plasma models with $B = 3\times10^{13}$ G, $\rho = 1$ g cm^{-3}, and $T = 3.16\times10^5$ K.

panels for a partially ionized hydrogen plasma with $B = 3\times10^{13}$ G, $\rho = 1$ g cm^{-3}, and $T = 3.16\times10^5$ K. In this case, the neutral fraction is 89%. For comparison, we show the results of an analogous calculation for the fully ionized plasma model. In addition to the proton cyclotron resonance at $\hbar\omega = 0.19$ keV that is present in both models, the absorption coefficients show rather pronounced features due to atomic transitions in the partially ionized plasma model. Most remarkable are the absorption features due to bound–bound transitions at $\hbar\omega \approx 0.2-0.3$ keV for μ_{+1} and the photoionization jump (partly smeared by the magnetic broadening) at $\hbar\omega = 0.4$ keV for μ_0. These features have clear imprints on the behavior of χ_{+1}^{H} amd χ_0^{H}.

6.3 Vacuum polarization

In certain ranges of the density ρ and frequency ω, normal-mode properties are dramatically affected by a specific QED effect called vacuum polarization (its other manifestation has already been considered in Section 5.5). The influence of vacuum polarization on neutron-star emission was first evaluated in [365, 366] and studied in detail in [367]. If the vacuum polarization is weak, it can be linearly added to the plasma polarization. Then the complex dielectric tensor can be written as $\boldsymbol{\varepsilon}' = \mathbf{I} + 4\pi\chi + 4\pi\chi^{\mathrm{vac}}$, where

$$\boldsymbol{\chi}^{\mathrm{vac}} = (4\pi)^{-1}\,\mathrm{diag}\,(\bar{a}, \bar{a}, \bar{a}+\bar{q}) \tag{75}$$

is the vacuum polarizability tensor and diag (...) is a diagonal matrix. The magnetic susceptibility of the vacuum is determined by the expression

$$\boldsymbol{\mu}^{-1} = \mathbf{I} + \mathrm{diag}\,(\bar{a}, \bar{a}, \bar{a}+\bar{m})\,. \tag{76}$$

The vacuum polarizability coefficients $\bar{a}$, $\bar{q}$, and $\bar{m}$ that enter Eqns (75) and (76) were obtained explicitly at $b \ll 1$ in [368], and were expressed in terms of special functions in the limits $b \ll 1$ and $b \gg 1$ in [369]. Numerical calculations were presented in [370]. Finally, in [364], we found simple but accurate expressions

$$\bar{a} = -\frac{2\alpha_{\mathrm{f}}}{9\pi}\ln\left(1 + \frac{b^2}{5}\,\frac{1+0.25487\,b^{3/4}}{1+0.75\,b^{5/4}}\right), \tag{77}$$

$$\bar{q} = \frac{7\alpha_{\mathrm{f}}}{45\pi}\,b^2\,\frac{1+1.2\,b}{1+1.33\,b+0.56\,b^2}\,, \tag{78}$$

$$\bar{m} = -\frac{\alpha_{\mathrm{f}}}{3\pi}\,\frac{b^2}{3.75+2.7\,b^{5/4}+b^2}\,. \tag{79}$$

Coefficients (77)–(79) are not small at $B \gtrsim 10^{16}$ G; therefore, the vacuum refraction coefficients substantially differ from unity. In such strong fields, the vacuum that surrounds a neutron star acts as a lens, distorting its radiation [371–373]. At smaller B, the vacuum polarization results in a resonance, which is manifested in the coincidence of the normal-mode polarization vectors at a certain frequency, depending on the plasma density. In photospheres with $B \gtrsim 10^{13}$ G, this resonance falls in the range $\sim 0.1-1$ keV and affects the thermal spectrum.

6.4 Polarization vectors of normal modes

The polarization vectors $\mathbf{e}^j$ for fully ionized plasmas were obtained in [374]. Their convenient expressions in terms of the coefficients $\varepsilon_\perp$, $\varepsilon_\parallel$, $\varepsilon_\wedge$, $\bar{a}$, $\bar{q}$, and $\bar{m}$, including the contributions of electrons, ions, and vacuum polarization, were presented in [375]. In a Cartesian coordinate system (xyz) with the z axis directed along the wave vector $\mathbf{k}$ and with $\mathbf{B}$ in the plane xz, we have

$$\mathbf{e}^j = \begin{pmatrix} e_x^j \\ e_y^j \\ e_z^j \end{pmatrix} = \frac{1}{\sqrt{1+K_j^2+K_{z,j}^2}}\begin{pmatrix} \mathrm{i}K_j \\ 1 \\ \mathrm{i}K_{z,j} \end{pmatrix}, \tag{80}$$

where

$$K_j = \beta\left\{1 + (-1)^j\left[1 + \frac{1}{\beta^2} + \frac{\bar{m}}{1+\bar{a}}\,\frac{\sin^2\theta_B}{\beta^2}\right]^{1/2}\right\}, \tag{81}$$

$$K_{z,j} = -\frac{(\varepsilon'_\perp - \varepsilon'_\parallel)\,K_j\cos\theta_B + \varepsilon_\wedge}{\varepsilon'_\perp\sin^2\theta_B + \varepsilon'_\parallel\cos^2\theta_B}\,\sin\theta_B\,, \tag{82}$$

$$\beta = \frac{\varepsilon'_\parallel - \varepsilon'_\perp + \varepsilon_\wedge^2/\varepsilon'_\perp + \varepsilon'_\parallel\bar{m}/(1+\bar{a})}{2\varepsilon_\wedge}\,\frac{\varepsilon'_\perp}{\varepsilon'_\parallel}\,\frac{\sin^2\theta_B}{\cos\theta_B}\,, \tag{83}$$

$\varepsilon'_\perp = \varepsilon_\perp + \bar{a}$, and $\varepsilon'_\parallel = \varepsilon_\parallel + \bar{a} + \bar{q}$. If the plasma and vacuum polarizabilities are as usual small ($|\chi_\alpha^{\mathrm{H}}| \ll (4\pi)^{-1}$ and $|\bar{a}|, \bar{q}, |\bar{m}| \ll 1$), then

$$\beta \approx \frac{2\chi_0^{\mathrm{H}} - \chi_{+1}^{\mathrm{H}} - \chi_{-1}^{\mathrm{H}} + (\bar{q}+\bar{m})/(2\pi)}{2\,(\chi_{+1}^{\mathrm{H}} - \chi_{-1}^{\mathrm{H}})}\,\frac{\sin^2\theta_B}{\cos\theta_B}\,. \tag{84}$$

6.5 Opacities

In the approximation of isotropic scattering, at a given frequency ω, the opacities can be represented in the form

$$\varkappa_j^{\rm a} = \sum_{\alpha=-1}^{1} \left|e_{j,\alpha}(\theta_B)\right|^2 \frac{\sigma_\alpha^{\rm a}}{m_{\rm i}}\,, \tag{85}$$

$$\varkappa_{jj'}^{\rm s} = \frac{3}{4} \sum_{\alpha=-1}^{1} \left|e_{j,\alpha}(\theta_B)\right|^2 \frac{\sigma_\alpha^{\rm s}}{m_{\rm i}} \int_0^\pi \left|e_{j',\alpha}(\theta'_B)\right|^2 \sin\theta'_B\,{\rm d}\theta'_B\,, \tag{86}$$

where σ_α are the cross sections for the three basic polarizations according to Eqn (43). The partial cross sections $\sigma_\alpha^{\rm a,s}$ include contributions of the photon interaction processes with free electrons or ions (free–free transitions), as well as with bound states of atoms and ions (bound–bound and bound–free transitions). This implies, in particular, averaging the photon and atom absorption cross sections over all values of $K_\perp$. Since the distribution over $K_\perp$ is continuous for the atoms and discrete for the ions, such averaging for atoms reduces to an integration over $K_\perp$, analogous to Eqn (61), whereas for ions, it implies summation with an appropriate statistical weight. To date, such a calculation has been realized for atoms of hydrogen [266, 350] and helium [308].

Figure 8 shows opacities for the two normal modes propagating at the angle $\theta_B = 10^\circ$ to the magnetic field under the same physical conditions as in Fig. 7. We can clearly distinguish the features reflecting the peaks at the ion cyclotron frequency and the resonant atomic frequencies, and the line crossings related to the behavior of the plasma polarizability as a function of frequency. For comparison, we also show opacities for the fully ionized plasma model under the same conditions. They are missing features related to atomic resonances, and their values are underestimated by orders of magnitude in a wide frequency range.

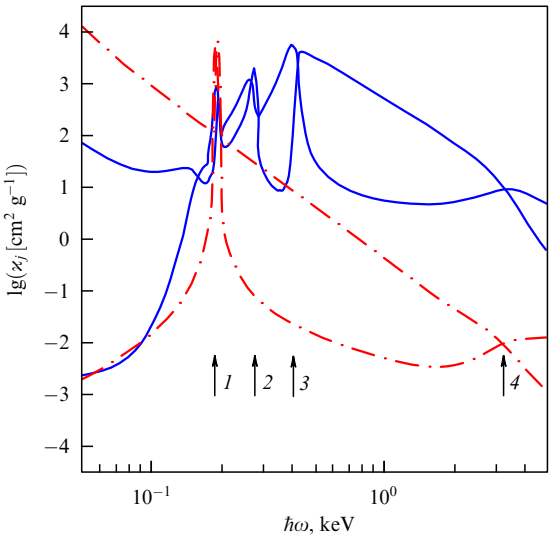

Figure 8. (Color online.) Logarithm of spectral opacities ($\lg \varkappa_j$) for two normal modes, propagating at the angle $\theta_B = 10^\circ$ to the magnetic field lines in a hydrogen plasma with $B = 3\times10^{13}$ G, $T = 3.16\times10^5$ K and $\rho = 1$ g cm^{-3}. Solid curves: partially ionized plasma model; dotted-dashed curves: fully ionized plasma model. The lower (upper) curve of each type corresponds to an extraordinary (ordinary) wave. The arrows indicate the features at resonant frequencies: *1* — ion cyclotron resonance $\omega = \omega_{\rm ci}$; *2* — energy threshold for the transition between the lowest two levels $\hbar\omega = |E_{0,0}^{(0)} - E_{1,0}^{(0)}|$; *3* — ground-state binding energy $\hbar\omega = |E_{0,0}^{(0)}|$; *4* — vacuum resonance.

6.6 Spectra of magnetic photospheres

Shibanov and coworkers [376] were the first to perform detailed calculations of radiation spectra formed in strongly magnetized neutron-star photospheres, using the fully ionized plasma model, and created a database of magnetic hydrogen spectra [269].[12] They have shown that the spectra of magnetic hydrogen and helium atmospheres are softer than the respective nonmagnetic spectra, but harder than the blackbody spectrum with the same temperature. In addition to the spectral energy distribution, these authors have also studied the polar diagram and polarization of the outgoing emission, which proved to be quite nontrivial because of the energy redistribution between the normal modes. The thermal radiation of a magnetized photosphere is strongly polarized, and the polarization sharply changes at the cyclotron resonance with increasing frequency. In contrast to isotropic blackbody radiation, the radiation of a magnetic photosphere consists of a narrow pencil beam $< 5^\circ$ along the magnetic field and a broad fan beam with typical angles of $\sim 20^\circ - 60^\circ$ [377] (see also [378]). These calculations have thus fully confirmed the previous analysis in [11].

Later, analogous calculations were performed by other research groups [375, 378, 379]. They paid special attention to manifestations of the ion cyclotron resonance in observed spectra in the presence of superstrong magnetic fields, which was prompted by the discovery of candidate magnetars. It was shown in [380] that vacuum polarization in superstrong fields leads to a conversion of the normal modes, when a photon related to one mode transforms, with some probability, into a photon of another mode while crossing a surface with a certain critical density. That density is related to the photon energy as

$$\rho = 0.00964\,\frac{A}{Z}\left(\frac{\hbar\omega}{\rm keV}\right)^2 \frac{B_{12}^2}{f_B^2}\ {\rm g\ cm^{-3}}\,, \tag{87}$$

where $f_B^2 = \alpha_{\rm f} b^2/[15\pi(\bar{q}+\bar{m})]$, while $\bar{q}$ and $\bar{m}$ are given in Eqns (78) and (79); f_B weakly depends on B with $f_B \approx 1$ at $B \lesssim 10^{14}$ G. The energy $\hbar\omega$ in Eqn (87) corresponds to the line crossing in Fig. 8, indicated by arrow *4*. It follows from Eqn (87) that in the field $B \sim 10^{14}$ G, this energy coincides with the ion cyclotron energy at the density where the atmosphere is optically thin for the extraordinary mode, but optically thick for the ordinary mode. Under such conditions, the mode conversion strongly suppresses the ion cyclotron feature in the emission spectrum.

In the first computations of partially ionized photospheres of neutron stars with magnetic fields $B \sim 10^{12}$–10^{13} G that were presented in [339, 346], the properties of atoms in magnetic fields were calculated by the adiabatic Hartree–Fock method (Section 5.3). The atomic motion was either ignored [346] or treated approximately by the perturbation theory [339].

In [364], a hydrogen photosphere model was constructed beyond the adiabatic approximation framework, taking full account of the partial ionization and the atomic motion effects in strong magnetic fields. Figure 9 gives an example of the radiation spectrum leaving such a photosphere with $B = 10^{13}$ G. We see a narrow absorption line at the proton cyclotron energy $E = 0.063$ keV and features at higher energies related to atomic transitions. For comparison, a spectrum calculated in the fully ionized plasma model and the

[12] Model NSA in the *XSPEC* database [210].

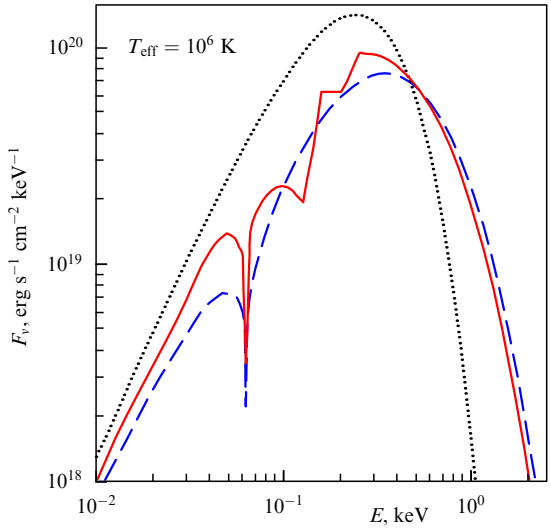

Figure 9. Local spectrum of a hydrogen photosphere with $B = 10^{13}$ G (the field is normal to the surface) and $T_{\rm eff} = 10^6$ K. The solid line represents a self-consistent model of a partially ionized photosphere, the dashed line represents the fully ionized atmosphere model, and the dots show the blackbody spectrum. (Figure provided by W Ho.)

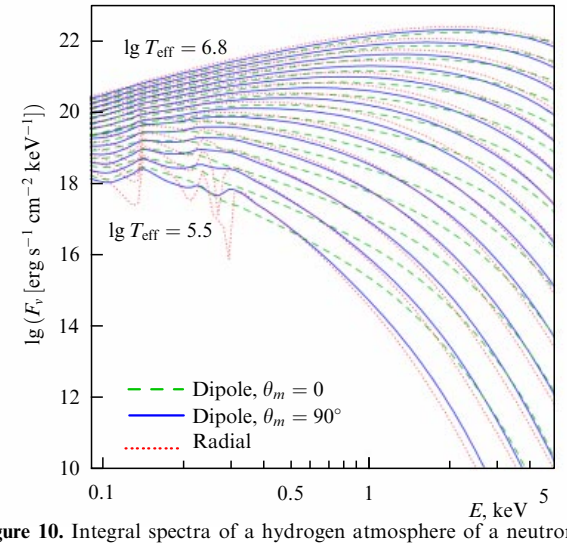

Figure 10. Integral spectra of a hydrogen atmosphere of a neutron star with different effective temperatures $T_{\rm eff}$ (lg $T_{\rm eff}$ [K] from 5.5 to 6.8 with the step 0.1). The dashed and solid lines respectively represent the model with a dipole field of the strength $B_{\rm p} = 10^{13}$ G at the pole and oriented along and across the line of sight. For comparison, the dotted curve shows the model with a constant field $B = 10^{13}$ G, normal to the surface.

Planck spectrum are shown. The comparison shows that the two photospheric models have similar spectral shapes, but the model that allows the partial ionization has additional features. The spectral maximum of both models is shifted to higher energies relative to the Planck maximum. This demonstrates that an attempt to interpret the hydrogen spectra with the blackbody model would strongly overestimate the effective temperature, while the fully ionized photosphere model yields a more realistic temperature but does not reproduce the spectral features caused by atomic transitions.

The magnetic fields and temperatures of neutron stars vary from one surface point to another. To reproduce the radiation spectrum that comes to an observer, we can use Eqn (15). The problem is complicated because the surface distributions of the magnetic field and the temperature are not known in advance. As a fiducial model, relativistic dipole model (16), (17) is conventionally used, while the temperature distribution, consistent with the magnetic-field distribution, is found from calculations of heat transport in neutron-star envelopes (see, e.g., [84]). Results of such calculations, performed in [381], are shown in Fig. 10. We see that the spectral features are strongly smeared by averaging over the surface, and the spectrum depends on the magnetic axis orientation θ_m. When the star rotates, this dependence leads to pulsations of the measured spectrum.

Model spectra of neutron-star photospheres composed of the atoms and ions of elements with $Z_{\rm n} \lesssim 10$ were calculated in [347, 348]. The quantum mechanical properties of the atoms and ions were calculated by the method in [301] and the atomic motion effects were treated by the perturbation theory (Section 5.6). The equation of state and ionization equilibrium were determined by the methods described in Section 5.8, the plasma polarizability was calculated by Eqn (74), and the opacities were treated according to Section 6.5. As an example, Fig. 11 demonstrates local spectra of a carbon photosphere with the magnetic field $B = 2 \times 10^{12}$ G, normal to the surface, and the field $B = 10^{12}$ G parallel to the surface, which approximately (without either relativistic corrections

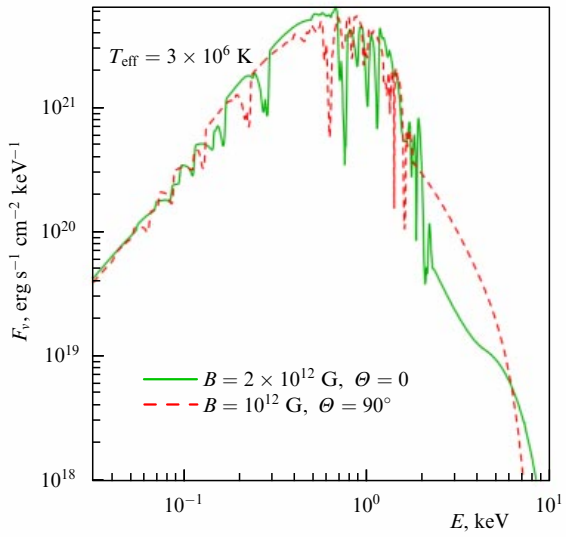

Figure 11. (Color online.) Local spectra at the magnetic pole (solid curve) and the equator (dashed curve) for a neutron star with a carbon atmosphere, the dipole field with the polar strength $B_{\rm p} = 2 \times 10^{12}$ G (neglecting the relativistic corrections), and a uniform effective temperature 3×10^6 K. (Figure 20 from [348], reproduced with permission of the authors and ©Oxford University Press.)

or temperature nonuniformity) corresponds to the local spectra at the magnetic pole and the equator of a star with a dipole magnetic field. Analogously to the case of a hydrogen photosphere, the integration over the surface between the pole and equator should smear the spectral features between the two limiting curves shown in the figure.

The calculations described in this section lie at the base of the database of the spectra of partially ionized, strongly magnetized neutron-star photospheres composed of hydrogen [381] and heavier elements up to neon [348].[13]

[13] NSMAX and NSMAXG models [382] in the *XSPEC* database [210].

7. Spectra of neutron stars with condensed surfaces

7.1 Radiation of a naked neutron star

As we have seen in Section 5.10, stars with a very low effective temperature with a superstrong magnetic field can have a liquid or solid condensed surface. In this case, thermal emission can escape directly from the metallic surface without transformation in a gaseous atmosphere, and then the spectrum is determined by the emission properties of this surface. The formation of thermal spectra at a condensed surface of a strongly magnetized neutron star depends on its reflection properties, which were considered in [115, 383–388]. The first studies [383, 384] provided order-of-magnitude estimates. A method of detailed calculation of the reflectivity was proposed in [385] and was then used with some modifications in [115, 385–388]. It is as follows. First, the normal-mode polarization vectors $\mathbf{e}_{1,2}^{(\mathrm{t})}$ in the medium under the surface, Eqns (80)–(82), and the complex refraction coefficients are expressed as functions of the angles θ_k and φ_k that determine the direction of a reflected ray (Fig. 1), using the standard dispersion equation for the transmitted wave and Snell's law. Second, the complex electric factors of the incident, reflected, and transmitted waves are expanded over the respective basic polarization vectors $\mathbf{e}_{1,2}^{(\mathrm{i,r,t})}$. Then the Maxwell boundary conditions yield a system of equations for the coefficients of these expansions. These reflected-wave expansion coefficients form the reflection matrix $\{r_{\omega,jj'}\}$ and determine the surface reflectivity for each incident-wave polarization, $r_{\omega,j}=\sum_{j'} r_{\omega,jj'}$. Then the total emissivity is $\varepsilon_\omega = 1-(r_{\omega,1}+r_{\omega,2})/2$.

Early work assumed that the ions are firmly fixed at the crystalline lattice sites in the metal. In [386–388], the authors considered not only this model but also the opposite limit of free ions. It is assumed in [386] that the real reflectivity of the surface lies between the limits given by these two models, although this problem has not yet been definitively solved.

Figure 12 shows examples of the emissivity ε_ω, normalized to the blackbody emissivity, as a function of the photon energy $E=\hbar\omega$, according to the free- and fixed-ion models, for different values of the angles θ_n, θ_m, and φ_k that are defined in Fig. 1. The characteristic energies $E_{\mathrm{ci}}=\hbar\omega_{\mathrm{ci}}$, $E_{\mathrm{pe}}=\hbar\omega_{\mathrm{pe}}$, and $E_{\mathrm{C}}=E_{\mathrm{ci}}+E_{\mathrm{pe}}^2/(\hbar\omega_{\mathrm{c}})$ are marked. The spectral features near these energies are explained in [386]. For instance, the emissivity suppression at $E_{\mathrm{ci}}\lesssim E\lesssim E_{\mathrm{C}}$ is due to the strong damping of one of the two normal modes in the plasma in this energy range. In the fixed-ion mode, $\omega_{\mathrm{ci}}\to 0$; therefore, there is no kink in the spectrum at $E\approx E_{\mathrm{ci}}$ in this model. The results almost coincide in the two alternative models at $E\gg E_{\mathrm{ci}}$, but strongly differ at $E\lesssim E_{\mathrm{ci}}$, which may be important for magnetar spectra. Near the electron plasma energy $E_{\mathrm{pe}}=\hbar\omega_{\mathrm{pe}}$, there is a resonant absorption, depending on the directions of the incident wave and the magnetic field.

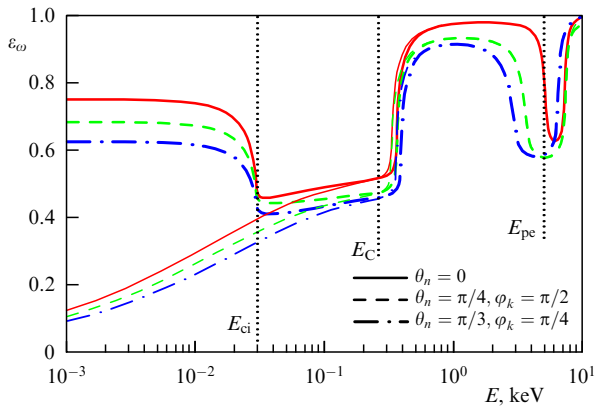

Figure 12. (Color online.) Emissivity of a condensed iron surface at $B=10^{13}$ G and $T=10^6$ K, averaged over polarizations, shown as a function of energy of a photon emitted at the angle $\theta_k=45°$, for different magnetic-field inclination angles θ_n and azimuthal angles φ_k. The thick and thin curves are obtained, respectively, in the models of free and fixed ions. Vertical dotted lines mark positions of the characteristic energies: the ion cyclotron energy ($E_{\mathrm{ci}}=\hbar\omega_{\mathrm{ci}}$), the electron plasma energy ($E_{\mathrm{pe}}=\hbar\omega_{\mathrm{pe}}$), and the hybrid energy (E_{C}).

The local flux density of radiation from a condensed surface is equal to the Planck function $\mathcal{B}_{\omega,T}$, Eqn (18), times the normalized emissivity ε_ω. Since ε_ω depends on the frequency ω and on the angles θ_n, θ_k, and φ_k (see Fig. 1), thermal radiation depends on the frequency and angles in a nontrivial way. In Fig. 12, the emissivity is averaged over polarizations. But $r_{\omega,1}\neq r_{\omega,2}$, and therefore the thermal emission of a condensed surface is polarized, the polarization depending in an equally nontrivial way on the frequency and angles. For example, the linear polarization degree can reach tens of percent near the frequencies ω_{ci} and ω_{pe}, which makes the polarization diagnostics of neutron stars with condensed surfaces promising. Both the intensity and the polarization degree can be evaluated using analytic expressions that were constructed in [388] for the reflectivity matrix of a condensed iron surface with $B=10^{12}-10^{14}$ G.

7.2 Thin and layered atmospheres

It was suggested in [389] that some neutron stars can have a hydrogen atmosphere of a finite thickness above the solid iron surface. If the optical depth of such an atmosphere is small for some wavelengths and large for others, this should lead to a peculiar spectrum, different from the spectra of thick atmospheres. Such spectra were calculated in [390–392] using simplified boundary conditions for the radiative transfer equation at the inner boundary of the atmosphere. More accurate boundary conditions were suggested in [388], where the authors took into account that an extraordinary or ordinary wave incident from outside on the interface gives rise to reflected waves of both polarizations, whose intensities add to the respective intensities of the waves emitted by the condensed surface:

$$I_{\omega,j}(\theta_k,\varphi)=\sum_{j'=1,2} r_{\omega,jj'}(\theta_k,\varphi)\,I_{\omega,j'}(\pi-\theta_k,\varphi) + \frac{1}{2}\left[1-r_{\omega,j}(\theta_k,\varphi)\right]\mathcal{B}_{\omega,T}\,. \tag{88}$$

In [388], the reflectivity matrix was calculated and fitted for linear polarizations, and then converted into the reflectivity matrix $\{r_{\omega,jj'}\}$ for normal modes pertinent to Eqn (88), using an approximate relation valid for a sufficiently rarefied photosphere.

In Fig. 13, we show local spectra of radiation emitted by hydrogen atmospheres of different thicknesses over the iron neutron-star surface with the magnetic field $B=4\times10^{13}$ G normal to the surface with the effective temperature $T_{\mathrm{s}}=1.2\times10^6$ K. The narrow absorption line corresponds to the proton cyclotron resonance in the atmosphere. The feature to the right of it is related to atomic transitions ($\mathrm{H}_{\mathrm{b-b}}$).

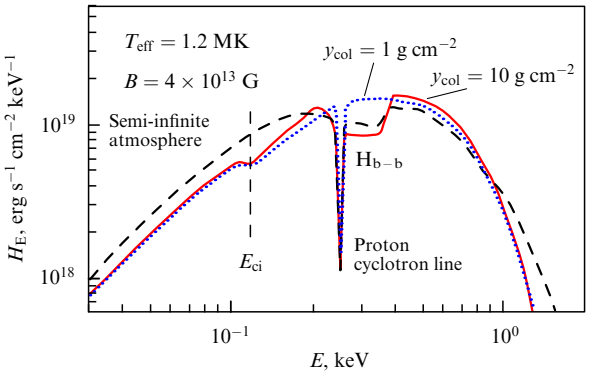

Figure 13. (Color online.) Comparison of the radiation spectrum of a neutron star with a partially ionized thick hydrogen photosphere (dashed line) with the spectra that are formed at hydrogen column densities of 1 g cm^{-2} (dots) and 10 g cm^{-2} (solid line) over the iron surface of the star (Fig. 12 from [388], provided by V F Suleimanov, reproduced with permission of the author and ©ESO.)

It has a large width because of the motion effects (Section 5.6). This feature is formed mainly at depths of ~ 2 g cm^{-2}, which is why it is almost invisible in the spectrum of the thinnest atmosphere that has the column density of 1 g cm^{-2}. The kink at $E_{\rm ci} = 0.12$ keV corresponds to the ion cyclotron energy of iron; therefore, it is absent for the pure hydrogen atmosphere. The spectrum of the moderately deep atmosphere (10 g cm^{-2}) reveals all three features. At high energies ($E \gtrsim 1$ keV), the spectrum is determined by the condensed-surface emission, because both finite atmospheres are almost transparent at such energies. The spectrum of a pure hydrogen atmosphere is harder in this spectral range (cf. Section 6.6).

The origin of thin atmospheres remains hazy. Three possible scenarios were discussed in [390]. The first is the accretion from the interstellar medium. But its rate should be very low in order to accumulate the hydrogen mass $4\pi R^2 y_{\rm col} \sim 10^{-20} M_\odot$ in $\sim 10^6$ years. Another scenario assumes diffusive nuclear burning of the hydrogen layer, which occurred soon after the formation of the neutron star [112]. But this process is too fast at the early cooling epoch, when the star is relatively hot, and would have rapidly consumed all the hydrogen on the surface [393]. The third possibility is a self-regulating mechanism that is driven by nuclear spallation in collisions with ultrarelativistic particles in regions of open field lines, which leads to the creation of protons and alpha particles. Estimate (23) for the penetration depth of the magnetospheric accelerated particles indicates that this process is capable of creating a hydrogen layer of the necessary thickness, $y_{\rm col} \sim 1$ g cm^{-2}.

It is natural to also consider an atmosphere having a helium layer beneath the hydrogen layer. Indeed, all three scenarios assume that a hydrogen–helium mixture appears originally on the surface, and the strong gravity quickly separates these two elements. Such a "sandwich atmosphere" was considered in [391], where the authors showed that its spectrum can have two or three absorption lines in the range $E \sim (0.2-1)$ keV at $B \sim 10^{14}$ G.

8. Theoretical interpretation of observed spectra

As we have seen in Section 4, theoretical models of nonmagnetic atmospheres are successfully applied to analyses of the spectra of many neutron stars with relatively weak magnetic fields $B \lesssim 10^9$ G. There are only a few such examples for stars with strong magnetic fields. They are discussed in this section. At the end of the section, we give a general compilation of modern estimates of the masses and radii of neutron stars with weak and strong magnetic fields, based on the photosphere models.

8.1 RX J1856.5–3754

As we have discussed in Section 4.4, there is no satisfactory description of the spectrum of the "Walter star" RX J1856.5–3754 based on nonmagnetic atmosphere models. Simple models of magnetic atmospheres have also failed to solve this problem. It was necessary to simultaneously explain the shape of the spectrum in the X-ray and optical ranges that reveal substantially different color temperatures $T_{\rm bb}^{\infty}$, and the complete absence of absorption lines or other spectral features, which was confirmed at a high significance level. To solve this problem, the model of a partially ionized hydrogen atmosphere of finite thickness above a condensed iron surface with a strong magnetic field was used in [390, 394]. It was possible to reproduce the measured spectrum of RX J1856.5–3754 in the entire range from X-rays to optical within observational error bars. The best agreement between the theoretical and observed spectra was achieved at the atmosphere column density $y_{\rm col} = 1.2$ g cm^{-2}, $B \sim (3-4) \times 10^{12}$ G, $T_{\rm eff}^{\infty} = (4.34 \pm 0.03) \times 10^5$ K, $z_{\rm g} = 0.25 \pm 0.05$, and $R_\infty = 17.2^{+0.5}_{-0.1}\, D_{140}$ km. Here, the errors are given at the 1σ significance level, and $D_{140} \equiv D/(140$ ps). We note that a fit of the observed X-ray spectrum with the Planck function yields a 70% higher temperature and 29% the magnitude of the radius of the emitting surface. Such a huge difference exposes the importance of a correct physical interpretation of an observed spectrum for evaluating neutron-star parameters.

From these estimates, with expressions (6)–(8) and Eqn (3), we obtain $T_{\rm eff} = (5.4 \pm 1.1) \times 10^5$ K, $R = 13.8^{+0.9}_{-0.6}\, D_{140}$ km, and $M = 1.68^{+0.22}_{-0.15}\, D_{140}\, M_\odot$. Forgetting the factor D_{140} for a moment, we might conclude that this radius is too large for such a mass. But the distance to the star is not known very accurately. The value $D = 140$ pc was adopted in [390] from [395] and lies between alternative estimates $D \approx 117$ pc [396] and $D \approx (160-170)$ pc [397, 398]. More recently, a better estimate of the distance was obtained: $D = 123^{+11}_{-15}$ pc [399]. With the last estimate, we obtain $R = 12.1^{+1.3}_{-1.6}$ km and $M = 1.48^{+0.16}_{-0.19}\, M_\odot$, which removes all the contradictions. Nevertheless, the given interpretation of the spectrum is not indisputable because it does not agree with the magnetic-field estimate $B \approx 1.5 \times 10^{13}$ G that has been obtained for this star from Eqn (1) in [400].

Using the same thin-atmosphere model, Ho [394] analyzed the light curve of RX J1856.5–3754 and obtained constraints on the angles α and ζ (Fig. 1). It turns out that the light curve can be explained if one of these angles is small ($< 6°$) while the other angle lies between 20° and 45°. In this case, the radio emission around the magnetic poles does not cross the line of sight. As noted in [394], this may explain the nondetection of this star as a radio pulsar [165].

8.2 RBS 1223

The spectrum of the X-ray source RBS 1223 was analyzed in [401] similarly to the analysis of RX J1856.5–3754 described in Section 8.1. Both sources belong to the class of XDINSs, but unlike the Walter star, RBS 1223 reveals a complex structure of the X-ray spectrum. It can be described by a

wide absorption line centered around $\hbar\omega = 0.3$ keV, superposed on the Planck spectrum, with the line parameters depending on the stellar rotation phase. Using all 2003–2007 *XMM-Newton* observations of this star, the authors of [401] obtained a set of X-ray spectra for different rotation phases. They tried to interpret these spectra with different models, assuming magnetic fields $B \sim 10^{13} - 10^{14}$ G, different atmosphere compositions, the possible presence of a condensed surface, and a finite atmosphere. Different surface temperature distributions were described by a self-consistent parametric model in [46].

As a result, the authors of [401] managed to describe the observed spectrum and its rotational phase dependence with the use of the model of an iron surface covered by a partially ionized hydrogen atmosphere with $y_{\rm col} \approx 1 - 10$ g cm^{-2}, with mutually consistent asymmetric bipolar distributions of the magnetic field and the temperature, with the polar values $B_{\rm p1} = B_{\rm p2} = (8.6 \pm 0.02) \times 10^{13}$ G, $T_{\rm p1} = 1.22^{+0.02}_{-0.05}$ MK, and $T_{\rm p2} = 1.15 \pm 0.04$ MK. The magnetic field and temperature proved to be rather smoothly distributed over the surface. When compared to the theoretical model in [46], this implies the absence of a superstrong toroidal component of the crustal magnetic field. The integral effective temperature is $T_{\rm eff} \approx 0.7$ MK. The gravitational redshift is estimated to be $z_{\rm g} = 0.16^{+0.03}_{-0.01}$, which converts to $(M/M_\odot)/R_6 = 0.87^{+0.13}_{-0.05}$ and suggests a stiff EOS of the neutron-star matter.

We must note that paper [401] preceded [388], which was discussed in Section 7. For this reason, the authors of [401] used rough approximations for the iron-surface emissivity, published previously, and simplified boundary conditions for the radiative transfer equations. An analysis of the same spectra with the use of improved results for the emissivity and more accurate boundary conditions, described in Section 7, remains to be done.

8.3 1E 1207.4–5209

The discovery of absorption lines in the spectrum of CCO 1E 1207.4–5209 at energies $E \sim 0.7\,N$ keV ($N = 1, 2, \ldots$) immediately gave rise to the natural assumption that they are caused by cyclotron harmonics [172]. As we have seen in Section 5.2, such harmonics can only be electronic, because ion harmonics are unobservable. Therefore, this interpretation implies that $B \approx 7 \times 10^{10}$ G. It was shown in [173] that only the first and second lines in the spectrum of 1E 1207.4–5209 are statistically significant, but some authors also take the third and fourth lines into account. This hypothesis was developed in [264], where the authors include both types of the electron cyclotron harmonics that were discussed in Section 5.2: quantum oscillations of the Gaunt factor and relativistic thermal harmonics. It is possible that a similar explanation of the shape of the spectrum may also be applied to CCO PSR J0821–4300 [167].

Mori et al. [347, 348] have critically analyzed the earlier hypotheses about the origin of the absorption lines in the spectrum of 1E 1207.4–5209 and suggested their own explanation. They analyzed and rejected such interpretations as the lines of molecular hydrogen ions, helium ions, and cyclotron lines and harmonics. One of the arguments against the last interpretation is that the fundamental cyclotron line should have a much larger depth in the atmosphere spectrum than actually observed. Another argument is that the cyclotron lines and harmonics have small widths at a fixed B; therefore, their observed width in the integral spectrum is determined by the B distribution. Thus, their width should be the same, in contradiction to observations [347]. These arguments were neglected in [264]. It has to be noted that in [347], as well as in [264], the authors studied the cyclotron harmonics in spectra of fully ionized plasmas. The effect of partial ionization on the model spectrum remains unexplored.

As an alternative, Mori et al. [347, 348] suggested models of atmospheres composed of mid-Z elements. An example of such a spectrum is shown in Fig. 11. Its convolution with the telescope point-spread function smears the line groups, producing wide and shallow suppressions of the spectral flux, similar to the observed ones. Integration of the local spectrum over the stellar surface, whose necessity we mentioned in Section 6.6, should lead to an additional smearing of the spectral features. The authors of [348] found that an oxygen atmosphere with the magnetic field $B = 10^{12}$ G provides a spectrum similar to the observed one. However, the constraint $B < 3.3 \times 10^{11}$ G obtained in [166] disagrees with this model, instead favoring the cyclotron interpretation of the lines.

Unlike in the cases of RX J1856.5–3754 and RBS 1223 that were considered above, there are no published results of a detailed fitting of the observed spectrum of 1E 1207.4–5209 with a theoretical model. Thus, the applicability of any of them remains hypothetical.

8.4 PSR J1119–6127

Recently, the partially ionized, strongly magnetized hydrogen photosphere model [381] has been successfully applied to interpret the observations of pulsar J1119–6127 [146], for which estimate (1) gives an atypically high field $B = 4 \times 10^{13}$ G. In the X-ray range, it emits pulsed radiation, which apparently has a mostly thermal nature. At fixed $D = 8.4$ kpc and $R = 13$ km, the bolometric flux gives an estimate of the mean effective temperature $T_{\rm eff} = 1.1$ MK. But it was difficult to explain the large pulsed fraction ($48 \pm 12\%$) by thermal emission. The authors of [146] managed to reproduce the X-ray light curve of this pulsar by assuming that one of its magnetic poles is surrounded by a heated area, which occupies 1/3 of the surface, is covered by hydrogen, and is heated to 1.5 MK, while the temperature of the opposite polar cap is below 0.9 MK.

8.5 Masses and radii: the results

The table presents modern estimates of neutron-star masses and radii, obtained from analyses of their thermal spectra with the atmosphere models. The estimates that fixed the surface gravity in advance are not listed here, because they are strongly biased, as shown, for example, in [209].

In most cases, the determination of the neutron-star radii remains unreliable. Estimates are typically done at a fixed distance D. An evaluation of R is also often performed for a fixed mass M. In most cases, this is stipulated by the fact that a joint evaluation of R and M (and all the more, R, M, and D) from the currently available thermal spectra leaves uncertainties that are too large and barely constrains M and D. A comparison of the results obtained for the same objects with different assumptions concerning D values readily shows that the choice of D can drastically affect the R estimate. In addition, the estimate of R is strongly affected by assumptions on the photosphere composition, as we can see, for example, from a comparison of the results obtained by assuming hydrogen and helium photospheres for qLMXBs in globular clusters M28 [243] and M13 [244].

Table. Estimates of neutron-star masses and radii based on atmosphere models.

Object	R, km	M, $M_\odot$	D, kpc	Ref.	Notes
qLMXB X7 in 47 Tuc	$14.5^{+1.8}_{-1.6}$	1.4 [a]	4.85 [a]	[209]	[b]
qLMXB XTE 1701 – 462	10.5 ± 2.5 [c]	1.4 [a]	8.8 [a]	[136]	[b]
qLMXB EXO 0748 – 676	$13.7^{+1.0}_{-2.7}$	$1.8^{+0.4}_{-0.6}$	7.1 [a]	[134]	[b]
Same object	$11.8^{+0.7}_{-2.2} - 15.2^{+1.5}_{-3.0}$	$1.5^{+0.5}_{-0.5} - 2.1^{+0.4}_{-0.8}$	5.9 – 8.3	[134]	[d], [e]
qLMXB in M28	$10.5^{+2.0}_{-2.9}$	$1.25^{+0.54}_{-0.63}$	5.5 [a]	[242]	[b]
Same object	9^{+3}_{-3*}	$1.4^{+0.4}_{-0.9*}$	5.5 [a]	[243]	[b]
Same object	14^{+3}_{-8*}	$2.0^{+0.5}_{-1.5*}$	5.5 [a]	[243]	[e]
qLMXB in NGC 6397	$6.6^{+1.2}_{-1.1}$	$0.84^{+0.30}_{-0.28}$	2.02 [a]	[242]	[b]
qLMXB in M13	$10.1^{+3.7}_{-2.8}$	$1.27^{+0.71}_{-0.63}$	6.5 [a]	[242]	[b]
Same object	$10.6^{+2.1}_{-2.2}$	1.4 [a]	7.7 [a]	[244]	[b]
Same object	$14.6^{+3.5}_{-3.1}$	1.4 [a]	7.7 [a]	[244]	[e]
qLMXB in ω Cen	$20.1^{+7.4}_{-7.2}$	$1.8^{+1.0}_{-1.1}$	4.8 [a]	[242]	[b]
qLMXB in NGC 6304	$9.4^{+4.9}_{-3.4}$	$1.16^{+0.90}_{-0.56*}$	6.22 [a]	[242]	[b]
CCO in Cas A	$15.6^{+1.3}_{-2.7}$	1.4 [a]	3.4 [a]	[214]	[f]
Same object	8 – 17	1.5 – 2.4	3.3 – 3.7	[214]	[d], [f]
CCO in HESS J1731	$12.6^{+2.1}_{-5.3} - 15.6^{+3.6}_{-5.3}$	$1.5^{+0.4}_{-0.6} - 2.2^{+0.3}_{-0.9}$	3.2 – 4.5	[237]	[d], [f]
Burster 4U 1724 – 307	14.7 ± 0.8	1.9 ± 0.4	5.3 – 7.7	[151]	[b]
Same object	18 ± 3.5	$1.05^{+0.55}_{-0.4}$	5.3 – 7.7	[151]	[e]
Burster GS 1826 – 24	< 8.2	< 1.3	< 4.3 [g]	[219]	[b]
Same object	< 19.8	< 2.8	< 9.7 [g]	[219]	[e]
PSR J0437 – 4715	> 11.1 (3σ)	1.76 [a]	0.1563 [a]	[252]	[b]; see Sect. 4.6
XDINS RX J1856	$12.1^{+1.3}_{-1.6}$	$1.48^{+0.16}_{-0.19}$	$0.123^{+0.011}_{-0.015}$ [h]	[390]	[c], [i], [j]; see Sect. 8.1
XDINS RBS 1223	16^{+1}_{-2}	1.4 [a]	$0.380^{+0.015}_{-0.030}$	[401]	[c], [i], [k]; see Sect. 8.2

Notes: Errors are listed at significance level 90%, unless otherwise stated. An asterisk next to a value of an error signifies that a hard limit of a model was reached. [a] The parameter is fixed. [b] Nonmagnetic H atmosphere. [c] Errors at the significance level 1σ (68%). [d] Results for selected limiting D from a range of possible values. [e] Nonmagnetic He atmosphere. [f] Nonmagnetic C atmosphere. [g] Constraint on $D\xi_b^{1/2}$ is given, where ξ_b is the anisotropy factor. [h] D is adopted from [396]. [i] Partially ionized thin H atmosphere over the iron surface. [j] $y_{col} = 1.2$ g cm^{-2}, $B \sim (3-4) \times 10^{12}$ G. [k] $y_{col} \sim 1$ g cm^{-2}, mutually consistent distributions of the magnetic field $B \approx 8 \times 10^{13}$ G and the temperature $T_s \approx 0.7$ MK.

9. Conclusions

We have considered the main features of neutron-star atmospheres and radiating surfaces and outlined the current state of the theory of the formation of their spectra. The observations of bursters and neutron stars in low-mass X-ray binaries are well described by nonmagnetic atmosphere models and yield ever improving information on the key parameters, such as neutron-star masses, radii, and temperatures. The interpretation of observations is entering a qualitatively new phase, unbound from the blackbody spectrum or the "canonical model" of neutron stars. Absorption lines have been discovered in the thermal spectra of strongly magnetized neutron stars. The next stage is their detailed theoretical description, which provides information on the surface composition, temperature, and magnetic field distributions. Indirectly, it yields information on heat transport and electrical conductivity in the crust, neutrino emission, nucleon superfluidity, and proton superconductivity in the core. To clarify this information, it remains to solve a number of problems related to the theory of magnetic atmospheres and radiating surfaces. We mention just a few of them.

First, calculations of the quantum mechanical properties of atoms and molecules in strong magnetic fields beyond the adiabatic approximation have so far been performed only for atoms with $Z_n \lesssim 10$ and for one- and two-electron molecules and molecular ions. The thermal motion effect on these properties has been rigorously treated only for the hydrogen atom and the helium ion, and approximately for heavier atoms. It is urgent that the finite nuclear mass effects be treated for heavier atoms, molecules, and their ions, including not only binding energies and characteristic sizes but also cross sections of interaction with radiation. This should underlie computations of photospheric ionization equilibrium and opacities, following the technique that is already established for hydrogen photospheres. In magnetar photospheres, we can anticipate the presence of a substantial

fraction of exotic molecules, including polymer chains. The properties of such molecules and their ions are poorly known. In particular, virtually unknown are their radiative cross sections, which are needed for photosphere modeling.

Second, the emissivities of condensed magnetized surfaces have been calculated in the framework of the two extreme models of free and fixed ions. It will be useful to do similar calculations using a more realistic description of ionic bonding in a magnetized condensed matter. This should be particularly important in the frequency range $\omega \lesssim \omega_{\rm ci}$, which is observable for the thermal spectrum in superstrong magnetic fields.

Third, the radiative transfer theory currently used for neutron-star photospheres implies that the electron plasma frequency is much smaller than the photon frequencies. In superstrong magnetic fields, this condition is violated in a substantial frequency range. Hence, the theory of magnetar spectra requires a more general treatment of radiative transfer in a magnetic field.

In conclusion, I thank my colleagues with whom I had the pleasure to work on some of the problems described in this review: V G Bezchastnov, G Chabrier, W C G Ho, D Lai, Z Medin, G G Pavlov, Yu A Shibanov, V F Suleimanov, M van Adelsberg, J Ventura, and K Werner. My special thanks go to Vasily Beskin, Wynn Ho, Alexander Kaminker, Igor Malov, Dmitry Nagirner, Yuri Shibanov, and Valery Suleimanov for the useful remarks on preliminary versions of this article. This study was partially supported by the Russian Ministry of Education and Science (Agreement 8409, 2012), the Russian Foundation for Basic Research (Grant 11-02-00253), the Program for Support of the Leading Scientific Schools of the Russian Federation (Grant NSh–294.2014.2), and PNPS (CNRS/INSU, France).

References

1. Haensel P, Potekhin A Y, Yakovlev D G *Neutron Stars 1*: *Equation of State and Structure* (New York: Springer, 2007)
2. Fortov V E *Phys. Usp.* **52** 615 (2009); *Usp. Fiz. Nauk* **179** 653 (2009)
3. Potekhin A Y *Phys. Usp.* **53** 1235 (2010); *Usp. Fiz. Nauk* **180** 1279 (2010)
4. Haensel P, Zdunik J L, Douchin F *Astron. Astrophys.* **385** 301 (2002)
5. Demorest P B et al. *Nature* **467** 1081 (2010)
6. Antoniadis J et al. *Science* **340** 448 (2013)
7. Zhang W, Woosley S E, Heger A *Astrophys. J.* **679** 639 (2008)
8. Pejcha O, Thompson T A, Kochanek C S *Mon. Not. R. Astron. Soc.* **424** 1570 (2012)
9. Kramer M, Stairs I H *Annu. Rev. Astron. Astrophys.* **46** 541 (2008)
10. Lattimer J M *Annu. Rev. Nucl. Part. Sci.* **62** 485 (2012)
11. Gnedin Yu N, Sunyaev R A *Astron. Astrophys.* **36** 379 (1974)
12. Trümper J et al. *Astrophys. J.* **219** L105 (1978)
13. Coburn W et al. *Astrophys. J.* **580** 394 (2002)
14. Rodes-Roca J J et al. *Astron. Astrophys.* **508** 395 (2009)
15. Pottschmidt K et al. *AIP Conf. Proc.* **1427** 60 (2012)
16. Boldin P A, Tsygankov S S, Lutovinov A A *Astron. Lett.* **39** 375 (2013); *Pis'ma Astron. Zh.* **39** 423 (2013)
17. Baushev A N, Bisnovatyi-Kogan G S *Astron. Rep.* **43** 241 (1999); *Astron. Zh.* **76** 283 (1999)
18. Araya-Góchez R A, Harding A K *Astrophys. J.* **544** 1067 (2000)
19. Terada Y et al. *Astrophys. J.* **648** L139 (2006)
20. Becker P A et al. *Astron. Astrophys.* **544** A123 (2012)
21. Poutanen J et al. *Astrophys. J.* **777** 115 (2013)
22. Nishimura O *Astrophys. J.* **781** 30 (2014)
23. Deutsch A J *Ann. d'Astrophys.* **18** 1 (1955)
24. Manchester R N, Taylor J H *Pulsars* (San Francisco: W.H. Freeman, 1977); Translated into Russian: *Pul'sary* (Translation Ed. A D Kuz'min) (Moscow: Mir, 1980)
25. Beskin V S *Phys. Usp.* **42** 1071 (1999); *Usp. Fiz. Nauk* **169** 1169 (1999)
26. Michel F C *Adv. Space Res.* **33** 542 (2004)
27. Spitkovsky A, in *High-Energy Emission from Pulsars and Their Systems* (Astrophysics and Space Science Proceedings, Eds N Rea, D F Torres) (Berlin: Springer-Verlag, 2011) p. 139
28. Beskin V S, Istomin Ya N, Philippov A A *Phys. Usp.* **56** 164 (2013); *Usp. Fiz. Nauk* **183** 179 (2013)
29. Pétri J *Mon. Not. R. Astron. Soc.* **424** 605 (2012)
30. Tchekhovskoy A, Spitkovsky A, Li J G *Mon. Not. R. Astron Soc.* **435** L1 (2013)
31. Timokhin A N, Arons J *Mon. Not. R. Astron. Soc.* **429** 20 (2013)
32. Beskin V S, Gurevich A V, Istomin Ya N *Sov. Phys. JETP* **58** 235 (1983); *Zh. Eksp. Teor. Fiz.* **85** 401 (1983)
33. Beskin V S, Gurevich A V, Istomin Ya N *Physics of the Pulsar Magnetosphere* (Cambridge: Cambridge Univ. Press, 1993)
34. Spitkovsky A *Astrophys. J.* **648** 51 (2006)
35. Manchester R N et al. *Astron. J.* **129** 1993 (2005); ATNF Pulsar Catalogue, http://www.atnf.csiro.au/research/pulsar/psrcat/
36. Bisnovatyi-Kogan G S *Phys. Usp.* **49** 53 (2006); *Usp. Fiz. Nauk* **176** 59 (2006)
37. Lorimer D R *Living Rev. Relativity* **11** 8 (2008); http://www.livingreviews.org/lrr-2008-8
38. Duncan R C, Thompson C *Astrophys. J.* **392** L9 (1992)
39. Popov S B, Prokhorov M E *Astrofizika Odinochnykh Neitronnykh Zvezd*: *Radiotikhie Neitronnye Zvezdy i Magnitary* (Astrophysics of Isolated Neutron Stars: Radioquiet Neutron Stars and Magnetars) (Moscow: SAI MSU, 2002); astro-ph/0205298
40. Mereghetti S *Astron. Astrophys. Rev.* **15** 225 (2008)
41. Mereghetti S *Braz. J. Phys.* **43** 356 (2013)
42. Rea N, in *Neutron Stars and Pulsars*: *Challenges and Opportunities after 80 Years* (Proc. IAU Symp. 291, Ed. J van Leeuwen) (Cambridge: Cambridge Univ. Press, 2013) p. 11
43. Dall'Osso S, Shore S N, Stella L *Mon. Not. R. Aston. Soc.* **398** 1869 (2009)
44. Ardeljan N V, Bisnovatyi-Kogan G S, Moiseenko S G *Mon. Not. R. Aston. Soc.* **359** 333 (2005)
45. Geppert U, Küker M, Page D *Astron. Astrophys.* **457** 937 (2006)
46. Pérez-Azorín J F, Miralles J A, Pons J A *Astron. Astrophys.* **451** 1009 (2006)
47. Akgün T et al. *Mon. Not. R. Astron. Soc.* **433** 2445 (2013)
48. Gavriil F P, Kaspi V M, Woods P M *Nature* **419** 142 (2002)
49. Kaspi V M *Proc. Natl. Acad. Sci. USA* **107** 7147 (2010)
50. Rea N et al. *Astrophys. J.* **781** L17 (2014)
51. Rea N et al. *Astrophys. J.* **770** 65 (2013)
52. Kaspi V M, Roberts M S E, Harding A K, in *Compact Stellar X-Ray Sources* (Cambridge Astrophysics Series, No. 39, Eds W Lewin, M van der Klis) (Cambridge: Cambridge Univ. Press, 2006) p. 279
53. Marsden D et al. *Astrophys. J.* **550** 397 (2001)
54. Ertan Ü et al. *Astrophys. Space Sci.* **308** 73 (2007)
55. Trümper J et al. *Astrophys. J.* **764** 49 (2013)
56. Bisnovatyi-Kogan G S, Ikhsanov N R *Astron. Rep.* **58** 217 (2014); *Astron. Zh.* **91** 275 (2014)
57. Malov I F, Machabeli G Z *Anomal'nye Pul'sary* (Anomalous Pulsars) (Moscow: Nauka, 2009)
58. Malov I F *Astron. Rep.* **54** 925 (2010); *Astron. Zh.* **87** 1004 (2010)
59. Boshkayev K et al. *Astron. Astrophys.* **555** A151 (2013)
60. Chandrasekhar S, Fermi E *Astrophys. J.* **118** 116 (1953)
61. Lai D, Shapiro E E *Astrophys. J.* **383** 745 (1991)
62. Bocquet M et al. *Astron. Astrophys.* **301** 757 (1995)
63. Cardall C, Prakash M, Lattimer J M *Astrophys. J.* **554** 322 (2001)
64. Kiuchi K, Kotake K *Mon. Not. R. Astron. Soc.* **385** 1327 (2008)
65. Frieben J, Rezzolla L *Mon. Not. R. Astron. Soc.* **427** 3406 (2012)
66. Shabad A E, Usov V V *Phys. Rev. D* **73** 125021 (2006)
67. Pechenick K R, Ftaclas C, Cohen J M *Astrophys. J.* **274** 846 (1983)
68. Page D *Astrophys. J.* **442** 273 (1995)
69. Pavlov G G, Zavlin V E *Astrophys. J.* **529** 1011 (2000)
70. Beloborodov A M *Astrophys. J.* **566** L85 (2002)
71. Zheleznyakov V V *Radiation in Astrophysical Plasmas* (Dordrecht: Kluwer, 1996); *Izluchenie v Astrofizicheskoi Plazme* (Moscow: Yanus-K, 1997)
72. Poutanen J, Gierliński M *Mon. Not. R. Astron. Soc.* **343** 1301 (2003)

73. Poutanen J, Beloborodov A M *Mon. Not. R. Astron. Soc.* **373** 836 (2006)
74. Ginzburg V L, Ozernoi L M *Sov. Phys. JETP* **20** 689 (1965); *Zh. Eksp. Teor. Fiz.* **47** 1030 (1964)
75. Muslimov A G, Tsygan A I *Sov. Astron.* **30** 567 (1986); *Astron. Zh.* **63** 958 (1986)
76. Pétri J *Mon. Not. R. Astron. Soc.* **433** 986 (2013)
77. Wilms J, Allen A, McCray R *Astron. J.* **542** 914 (2000)
78. Romanova M M et al. *Mon. Not. R. Astron. Soc.* **421** 63 (2012)
79. La Palombara N et al. *Astron. Astrophys.* **539** A82 (2012)
80. Harding A K, Lai D *Rep. Prog. Phys.* **69** 2631 (2006)
81. Medin Z, Lai D *Mon. Not. R. Astron. Soc.* **406** 1379 (2010)
82. Beloborodov A M *Astrophys. J.* **762** 13 (2013)
83. Burwitz V et al. *Astron. Astrophys.* **399** 1109 (2003)
84. Potekhin A Y et al. *Astrophys. J.* **594** 404 (2003)
85. Pons J, Miralles J A, Geppert U *Astron. Astrophys.* **496** 207 (2009)
86. Lorenz C P, Ravenhall D G, Pethick C J *Phys. Rev. Lett.* **70** 379 (1993)
87. Pethick C J, Potekhin A Y *Phys. Lett. B* **427** 7 (1998)
88. Pearson J M, Goriely S, Chamel N *Phys. Rev. C* **83** 065810 (2011)
89. Potekhin A Y, Chabrier G *Phys. Rev. E* **62** 8554 (2000)
90. Potekhin A Y, Chabrier G *Astron. Astrophys.* **550** A43 (2013)
91. Alcock C, Illarionov A *Astrophys. J.* **235** 534 (1980)
92. Hameury J M, Heyvaerts J, Bonazzola S *Astron. Astrophys.* **121** 259 (1983)
93. Brown E F, Bildsten L, Chang P *Astrophys. J.* **574** 920 (2002)
94. Chang P, Bildsten L, Arras P *Astrophys. J.* **723** 719 (2010)
95. Beznogov M V, Yakovlev D G *Phys. Rev. Lett.* **111** 161101 (2013)
96. Gudmundsson E H, Pethick C J, Epstein R I *Astrophys. J.* **272** 286 (1983)
97. Yakovlev D G, Pethick C J *Annu. Rev. Astron. Astrophys.* **42** 169 (2004)
98. Ventura J, Potekhin A Y, in *The Neutron Star — Black Hole Connection. Proc. of the NATO Advanced Study Institute, Elounda, Crete, Greece, 7–18 June 1999* (NATO Science Series C, Vol. 567, Eds C Kouveliotou, E P J van den Heuvel, J Ventura) (Dordrecht: Kluwer Acad. Publ., 2001) p. 393
99. Sobolev V V *Course in Theoretical Astrophysics* (Springfield: NASA, 1969); Translated from Russian: *Kurs Teoreticheskoi Astrofiziki* 2nd ed. (Moscow: Nauka, 1975)
100. Shibanov Yu A et al., in *The Many Faces of Neutron Stars* (NATO Science Series C, Vol. 515, Eds R Buccheri, J van Paradijs, M A Alpar) (Dordrecht: Kluwer Acad. Publ., 1998) p. 553
101. Tsai Y-S *Rev. Mod. Phys.* **46** 815 (1974)
102. Bogdanov S, Rybicki G B, Grindlay J E *Astrophys. J.* **670** 668 (2007)
103. Rosseland S *Mon. Not. R. Astron. Soc.* **84** 525 (1924)
104. Mihalas D *Stellar Atmospheres* 2nd ed. (San Francicso: W.H. Freeman, 1978); Translated into Russian: *Zvezdnye Atmosfery* Vols 1, 2 (Translation Ed. V V Ivanov) (Moscow: Mir, 1982)
105. Potekhin A Y, Chabrier G, Yakovlev D G *Astrophys. Space Sci.* **308** 353 (2007); corrected version: astro-ph/0611014, v3
106. Kotov Yu D, Kel'ner S R, Bogovalov S V *Sov. Astron. Lett.* **12** 168 (1986); *Pis'ma Astron. Zh.* **12** 402 (1986)
107. Shklovskii I S *Supernovae* (London: Wiley, 1968); *Sverkhnovye Zvezdy i Svyazannye s Nimi Problemy* 2nd ed. (Moscow: Nauka, 1976)
108. Shvartsman V F *Sov. Astron.* **15** 342 (1971); *Astron. Zh.* **48** 438 (1971)
109. Blaes O M et al. *Astrophys. J.* **199** 634 (1992)
110. Lipunov V M *Astrophysics of Neutron Stars* (Berlin: Springer-Verlag, 1992); Translated from Russian: *Astrofizika Neitronnykh Zvezd* (Moscow: Nauka, 1987)
111. Chiu H-Y, Salpeter E E *Phys. Rev. Lett.* **12** 413 (1964)
112. Chang P, Bildsten L *Astrophys. J.* **585** 464 (2003)
113. Rosen L C *Astrophys. Space Sci.* **1** 372 (1968)
114. Jones P *Mon. Not. R. Astron. Soc.* **184** 807 (1978)
115. Turolla R, Zane S, Drake J J *Astrophys. J.* **603** 265 (2004)
116. Zavlin V E, in *Neutron Stars and Pulsars* (Astrophysics and Space Science Library, Vol. 357, Ed. W Becker) (Berlin: Springer, 2009) p. 181
117. Haensel P, Zdunik J L *Astron. Astrophys.* **227** 431 (1990)
118. Haensel P, Zdunik J L *Astron. Astrophys.* **480** 459 (2008)
119. Bisnovatyi-Kogan G S, Chechetkin V M *Astrophys. Space Sci.* **26** 25 (1974)
120. Bisnovatyi-Kogan G S, Chechetkin V M *Sov. Phys. Usp.* **22** 89 (1979); *Usp. Fiz. Nauk* **127** 263 (1979)
121. Yakovlev D G et al. *Astron. Astrophys.* **417** 169 (2004)
122. Levenfish K P, Haensel P *Astrophys. Space Sci.* **308** 457 (2007)
123. Ho W C G *Mon. Not. R. Astron. Soc.* **418** L99 (2011)
124. Wijnands R, Degenaar N, Page D *Mon. Not. R. Astron. Soc.* **432** 2366 (2013)
125. Brown E F, Bildsten L, Rutledge R E *Astrophys. J.* **504** L95 (1998)
126. Syunyaev R et al. *Sov. Astron. Lett.* **16** 59 (1990); *Pis'ma Astron. Zh.* **16** 136 (1990)
127. Wijnands R et al. *Astrophys. J.* **560** L159 (2001)
128. Shternin P S et al. *Mon. Not. R. Astron. Soc.* **382** L43 (2007)
129. Jones P B *Mon. Not. R. Astron. Soc.* **351** 956 (2004)
130. Cackett E M et al. *Mon. Not. R. Astron. Soc.* **372** 479 (2006)
131. Cackett E M et al. *Astrophys. J.* **722** L137 (2010)
132. Cackett E M et al. *Astrophys. J.* **687** L87 (2008)
133. Cackett E M et al. *Astrophys. J.* **774** 131 (2013)
134. Díaz Trigo M et al. *Astron. Astrophys.* **528** A150 (2011)
135. Degenaar N, Wijnands R, Miller J M *Astrophys. J.* **767** L31 (2013)
136. Fridriksson J K et al. *Astrophys. J.* **736** 162 (2011)
137. Page D, Reddy S *Phys. Rev. Lett.* **111** 241102 (2013)
138. Turlione A, Aguilera D N, Pons J A, arXiv:1309.3909
139. Degenaar N et al. *Astrophys. J.* **775** 48 (2013)
140. Heinke C O et al. *Astrophys. J.* **691** 1035 (2009)
141. Coti Zelati F et al. *Mon. Not. R. Astron. Soc.* **438** 2634 (2014)
142. Cackett E M et al. *Astrophys. J.* **720** 1325 (2010)
143. Degenaar N, Wijnands R *Mon. Not. R. Astron. Soc.* **422** 581 (2012)
144. Rutledge R E et al. *Astrophys. J.* **577** 346 (2002)
145. Becker W, Trümper J *Astron. Astrophys.* **326** 682 (1997)
146. Ng C-Y et al. *Astrophys. J.* **761** 65 (2012)
147. Shapiro S L, Teukolsky S A *Black Holes, White Dwarfs, and Neutron Stars*: *The Physics of Compact Objects* (New York: Wiley, 1983); Translated into Russian: *Chernye Dyry, Belye Karliki i Neitronnye Zvezdy* Pt. 2 (Translation Ed. Ya A Smorodinsky) (Moscow: Mir, 1985)
148. Van Paradijs J *Nature* **274** 650 (1978)
149. Strohmayer T, Bildsten L, in *Compact Stellar X-Ray Sources* (Cambridge Astrophysics Series, No. 39, Eds W Lewin, M van der Klis) (Cambridge: Cambridge Univ. Press, 2006) p. 113
150. Hoffman J A, Marshall H L, Lewin W H G *Nature* **271** 630 (1978)
151. Suleimanov V F et al. *Astrophys. J.* **742** 122 (2011)
152. Basko M M, Sunyaev R A *Mon. Not. R. Astron. Soc.* **175** 395 (1976)
153. Lapidus I I, Syunyaev R A, Titarchuk L G *Astrophysics* **23** 663 (1985); *Astrofizika* **23** 503 (1985)
154. Inogamov N A, Sunyaev R A *Astron. Lett.* **25** 269 (1999); *Pis'ma Astron. Zh.* **25** 323 (1999)
155. Inogamov N A, Sunyaev R A *Astron. Lett.* **36** 848 (2010); *Pis'ma Astron. Zh.* **36** 896 (2010)
156. Gilfanov M, Revnivtsev M, Molkov S *Astron. Astrophys.* **410** 217 (2003)
157. Revnivtsev M G, Suleimanov V F, Poutanen J *Mon. Not. R. Astron. Soc.* **434** 2355 (2013)
158. Malofeev V M, Malov O I, Teplykh D A *Asrophys. Space Sci.* **308** 211 (2007)
159. Teplykh D et al. *AIP Conf. Proc.* **1357** 201 (2011)
160. De Luca A *AIP Conf. Proc.* **983** 311 (2008)
161. Harding A K *Frontiers Phys.* **8** 679 (2013)
162. Haberl F *Astrophys. Space Sci.* **308** 181 (2007)
163. Turolla R, in *Neutron Stars and Pulsars* (Astrophysics and Space Science Library, Vol. 357, Ed. W Becker) (Berlin: Springer, 2009) p. 141
164. Kondratiev V I et al. *Astrophys. J.* **702** 692 (2009); *Astrophys. J.* **708** 910 (2010), Erratum
165. Kaplan D L, van Kerkwijk M H *Astrophys. J.* **740** L30 (2011)
166. Halpern J P, Gotthelf E V *Astrophys. J.* **709** 436 (2010)
167. Gotthelf E V, Halpern J P, Alford J *Astrophys. J.* **765** 58 (2013)
168. Shabaltas N, Lai D *Astrophys. J.* **748** 148 (2012)
169. Rutledge R E, Fox D B, Shevchuk A H *Astrophys. J.* **672** 1137 (2008)
170. Halpern J P, Bogdanov S, Gotthelf E V *Astrophys. J.* **778** 120 (2013)
171. Sanwal D et al. *Astrophys. J.* **574** L61 (2002)
172. Bignami G F et al. *Nature* **423** 725 (2003)

173. Mori K, Chonko J C, Hailey, C J *Astrophys. J.* **631** 1082 (2005)
174. Haberl F et al. *Astron. Astrophys.* **420** 635 (2004)
175. Hambaryan V et al. *Astron. Astrophys.* **497** L9 (2009)
176. Schwope A D et al. *Astrophys. Space Sci.* **308** 619 (2007)
177. Cropper M et al. *Astrophys. Space Sci.* **308** 161 (2007)
178. Kaplan D, van Kerkwijk M *Astrophys. J.* **692** L62 (2009)
179. Schwope A D et al. *Astron. Astrophys.* **499** 267 (2009)
180. van Kerkwijk M H et al. *Astrophys. J.* **608** 432 (2004)
181. Haberl F et al. *Astron. Astrophys.* **419** 1077 (2004)
182. Walter F M, Wolk S J, Neuhäuser R *Nature* **379** 233 (1996)
183. Burwitz V et al. *Astron. Astrophys.* **399** 1109 (2001)
184. Tiengo A et al. *Nature* **500** 312 (2013)
185. Strohmayer T E, Ibrahim A I *Astrophys. J.* **537** L111 (2000)
186. Ibrahim A I et al. *Astrophys. J.* **574** L51 (2002)
187. Kargaltsev O et al. *Science* **337** 946 (2012)
188. Zavlin V E, Pavlov G G, Shibanov Yu A *Astron. Astrophys.* **315** 141 (1996)
189. Ginzburg V L *The Propagation of Electromagnetic Waves in Plasmas* 2nd ed. (Oxford: Pergamon Press, 1970); Translated from Russian: *Rasprostranenie Elektromagnitnykh Voln v Plazme* 2nd ed. (Moscow: Nauka, 1967)
190. Donati J-F, Landstreet J D *Annu. Rev. Astron. Astrophys.* **47** 333 (2009)
191. Ivanov V V *Transfer of Radiation in Spectral Lines* (Washington, DC: National Bureau of Standards, 1973); Translated from Russian: *Perenos Izlucheniya i Spektry Nebesnykh Tel* (Moscow: Nauka, 1969)
192. Chandrasekhar S *Radiative Transfer* (Oxford: Clarendon Press, 1950); Translated into Russian: *Perenos Luchistoi Energii* (Translation Ed. E S Kuznetsov) (Moscow: IL, 1953)
193. Haakonsen C B et al. *Astrophys. J.* **749** 52 (2012)
194. Suleimanov V, Poutanen J, Werner K *Astron. Astrophys.* **545** A120 (2012)
195. Paczyński B *Astrophys. J.* **267** 315 (1983)
196. Ishimaru A *Wave Propagation and Scattering in Random Media* Vol. 1 *Single Scattering and Transport Theory* (New York: Academic Press, 1978); Translated into Russian: *Rasprostranenie i Rasseyanie Voln v Sluchaino-neodnorodnykh Sredakh* Vol. 1 *Odnokratnoe Rasseyanie i Teoriya Perenosa* (Translation Ed. V I Tatarskii) (Moscow: Mir, 1981)
197. Kompaneets A S *Sov. Phys. JETP* **4** 730 (1957); *Zh. Eksp. Teor. Fiz.* **31** 876 (1956)
198. Zavlin V E, Shibanov Yu A *Sov. Astron.* **35** 499 (1991); *Astron. Zh.* **68** 999 (1991)
199. Grebenev S A, Sunyaev R A *Astron. Lett.* **28** 150 (2002); *Pis'ma Astron. Zh.* **28** 175 (2002)
200. Suleimanov V F, Poutanen J *Mon. Not. R. Astron. Soc.* **369** 2036 (2006)
201. Suleimanov V F, Poutanen J, Werner K *Astron. Astrophys.* **527** A139 (2011)
202. Carson T R *Annu. Rev. Astron. Astrophys.* **14** 95 (1976)
203. Rogers F J, Iglesias C A *Space Sci. Rev.* **85** 61 (1998)
204. Iglesias C A, Rogers F J *Astrophys. J.* **464** 943 (1996)
205. Seaton M J *Mon. Not. R. Astron. Soc.* **362** L1 (2005)
206. Paxton B et al. *Astrophys. J. Suppl.* **208** 4 (2013); MESA, http://mesa.sourceforge.net/
207. Romani R W *Astrophys. J.* **313** 718 (1987)
208. Gänsicke B T, Braje T M, Romani R W *Astron. Astrophys.* **386** 1001 (2002)
209. Heinke C O et al. *Astrophys. J.* **644** 1090 (2006)
210. Arnaud K A *ASP Conf. Ser.* **101** 17 (1996); XSPEC: An X-Ray Spectral Fitting Package, http://starchild.gsfc.nasa.gov/xanadu/xspec/
211. Suleimanov V F et al. *Astrophys. J. Suppl.* **210** 13 (2014)
212. Rajagopal M, Romani R W *Astrophys. J.* **461** 327 (1996)
213. Pons J A et al. *Astrophys. J.* **564** 981 (2002)
214. Ho W C G, Heinke C O *Nature* **462** 71 (2009)
215. London R A, Howard W M, Taam R E *Astrophys. J.* **287** L27 (1984)
216. London R A, Taam R E, Howard W M *Astrophys. J.* **306** 170 (1986)
217. Lapidus I I, Syunyaev R A, Titarchuk L G *Sov. Astron. Lett.* **12** 383 (1986); *Pis'ma Astron. Zh.* **12** 918 (1986)
218. Kaminker A D et al. *Astron. Astrophys.* **220** 117 (1989)
219. Zamfir M, Cumming A, Galloway D K *Astrophys. J.* **749** 69 (2012)
220. Heger A et al. *Astrophys. J.* **671** L141 (2007)
221. Özel F, Baym G, Güver T *Phys. Rev. D* **82** 101301(R) (2010)
222. Özel F *Rep. Prog. Phys.* **76** 016901 (2013)
223. Güver T, Özel F *Astrophys. J.* **765** L1 (2013)
224. Werner K, Deetjen J, in *Pulsar Astronomy – 2000 and Beyond* (ASP Conference Series, Vol. 202, Eds M Kramer, N Wex, R Wielebinski) (San Francisco: ASP, 2000) p. 623
225. Sobelman I I, Vainshtein L A, Yukov E A *Excitation of Atoms and Broadening of Spectral Lines* (Berlin: Springer-Verlag, 1981); Translated from Russian: Vainshtein L A, Sobelman I I, Yukov E A *Vozbuzhdenie Atomov i Ushirenie Spektral'nykh Linii* (Moscow: Nauka, 1979)
226. Potekhin A Y, Chabrier G, Chabrier D *Phys. Rev. E* **65** 036412 (2002)
227. Suleimanov V F, Werner K *Astron. Astrophys.* **466** 661 (2007)
228. Rauch T, Suleimanov V, Werner K *Astron. Astrophys.* **490** 1127 (2008)
229. Drake J J et al. *Astrophys. J.* **572** 996 (2002)
230. van Kerkwijk M H, Kulkarni S R *Astron. Astrophys.* **380** 221 (2001)
231. Gaensler B M, Slane P O *Annu. Rev. Astron. Astrophys.* **44** 17 (2006)
232. Tiengo A, Mereghetti S *Astrophys. J.* **657** L101 (2007)
233. Heinke C O, Ho W C G *Astrophys. J.* **719** L167 (2010)
234. Page D et al. *Phys. Rev. Lett.* **106** 081101 (2011)
235. Shternin P S et al. *Mon. Not. R. Astron. Soc.* **412** L108 (2011)
236. Posselt B et al. *Astrophys. J.* **779** 186 (2013)
237. Klochkov D et al. *Astron. Astrophys.* **556** A41 (2013)
238. Rutledge R E et al. *Astrophys. J.* **514** 945 (1999)
239. Rutledge R E et al. *Astrophys. J.* **580** 413 (2002)
240. Heinke C O et al. *Astrophys. J.* **598** 501 (2003)
241. Guillot S et al. *Mon. Not. R. Astron. Soc.* **392** 665 (2009)
242. Guillot S et al. *Astrophys. J.* **772** 7 (2013)
243. Servillat M et al. *Mon. Not. R. Astron. Soc.* **423** 1556 (2012)
244. Catuneanu A et al. *Astrophys. J.* **764** 145 (2013)
245. Cadeau C et al. *Astrophys. J.* **654** 458 (2007)
246. Garasyov M A, Derishev E V, Kocharovsky Vl V *Radiophys. Quantum Electron.* **54** 304 (2011); *Izv. Vyssh. Uchebn. Zaved. Radiofiz.* **54** 335 (2011)
247. Durant M et al. *Astrophys. J.* **746** 6 (2012)
248. Zavlin V E, Pavlov G G *Astron. Astrophys.* **329** 583 (1998)
249. Zavlin V E et al. *Astrophys. J.* **569** 894 (2002)
250. Bogdanov S, Grindlay J E, Rybicki G B *Astrophys. J.* **689** 407 (2008)
251. Bogdanov S, Grindlay J E, Rybicki G B *Astrophys. J.* **648** L55 (2006)
252. Bogdanov S *Astrophys. J.* **762** 96 (2013)
253. Verbiest J P W et al. *Astrophys. J.* **679** 675 (2008)
254. Deller A T et al. *Astrophys. J.* **685** L67 (2008)
255. Landau L *Z. Phys.* **64** 629 (1930); Translated into Russian: *Sobranie Trudov* Vol. 1 (Moscow: Nauka, 1969) p. 47
256. Sokolov A A, Ternov I M *Radiation from Relativistic Electrons* (New York: American Institute of Physics, 1986); Translated from Russian: *Relyativistskii Elektron* (Moscow: Nauka, 1974)
257. Armstrong B H, Nicholls R W *Emission, Absorption, and Transfer of Radiation in Heated Atmospheres* (Oxford: Pergamon Press, 1972)
258. Potekhin A Y, Pavlov G G *Astrophys. J.* **483** 414 (1997)
259. Ventura J, Nagel W, Mészáros P *Astrophys. J.* **233** L125 (1979)
260. Ventura J *Phys. Rev. D* **19** 1684 (1979)
261. Kaminker A D, Pavlov G G, Shibanov Yu A *Astrophys. Space Sci.* **86** 249 (1982)
262. Mészáros P *High-Energy Radiation from Magnetized Neutron Stars* (Chicago: Univ. of Chicago Press, 1992)
263. Pavlov G G, Shibanov Yu A, Yakovlev D G *Astrophys. Space Sci.* **73** 33 (1980)
264. Suleimanov V F, Pavlov G G, Werner K *Astrophys. J.* **751** 15 (2012)
265. Pavlov G G, Panov A N *Sov. Phys. JETP* **44** 300 (1976); *Zh. Eksp. Teor. Fiz.* **71** 572 (1976)
266. Potekhin A Y, Chabrier G *Astrophys. J.* **585** 955 (2003)
267. Potekhin A Y *Astron. Astrophys.* **518** A24 (2010)
268. Potekhin A Y, Lai D *Mon. Not. R. Astron. Soc.* **376** 793 (2007)
269. Pavlov G G et al., in *The Lives of the Neutron Stars* (NATO ASI Series C, Vol. 450, Eds M A Alpar, Ü Kiziloğlu, J van Paradijs) (Dordrecht: Kluwer Acad. Publ., 1995) p. 71
270. Cohen R, Lodenquai J, Ruderman M *Phys. Rev. Lett.* **25** 467 (1970)
271. Loudon R *Am. J. Phys.* **27** 649 (1959)
272. Hasegawa H, Howard R E *J. Phys. Chem. Solids* **21** 179 (1961)

273. Garstang R H *Rep. Prog. Phys.* **40** 105 (1977)
274. Ruder H et al. *Atoms in Strong Magnetic Fields* (Berlin: Springer-Verlag, 1994)
275. Kadomtsev B B *Sov. Phys. JETP* **31** 945 (1970); *Zh. Eksp. Teor. Fiz.* **58** 1765 (1970)
276. Lieb E H, Solovej J P, Yngvason J *Phys. Rev. Lett.* **69** 749 (1992)
277. Haines L K, Roberts D H *Am. J. Phys.* **37** 1145 (1969)
278. Kadomtsev B B, Kudryavtsev V S *JETP Lett.* **13** 42 (1971); *Pis'ma Zh. Eksp. Teor. Fiz.* **13** 61 (1971)
279. Simola J, Virtamo J *J. Phys. B At. Mol. Phys.* **11** 3309 (1978)
280. Rosner W et al. *J. Phys. B At. Mol. Phys.* **17** 29 (1984)
281. Forster H et al. *J. Phys. B At. Mol. Phys.* **17** 1301 (1984)
282. Potekhin A Y, Pavlov G G, Ventura J *Astron. Astrophys.* **317** 618 (1997)
283. Potekhin A Y *J. Phys. B At. Mol. Opt. Phys.* **31** 49 (1998)
284. Popov V S, Karnakov B M *JETP* **114** 1 (2012); *Zh. Eksp. Teor. Fiz.* **141** 5 (2012)
285. Surmelian G L, O'Connel R F *Astrophys. J.* **190** 741 (1974)
286. Wunner G et al. *Mon. Not. R. Astron. Soc.* **198** 769 (1982)
287. Al-Hujaj O-A, Schmelcher P *Phys. Rev. A* **70** 023411 (2004)
288. Jones P B *Mon. Not. R. Astron. Soc.* **216** 503 (1985)
289. Relovsky B M, Ruder H *Phys. Rev. A* **53** 4068 (1996)
290. Braun M *Phys. Rev. A* **65** 033415 (2002)
291. Jones M D, Ortiz G, Ceperley D M *Phys. Rev. E* **55** 6202 (1997)
292. Bücheler S et al. *Phys. Rev. A* **76** 032501 (2007)
293. Fock V A *Fundamentals of Quantum Mechanics* (Moscow: Mir Publ., 1978); Translated from Russian *Nachala Kvantovoi Mekhaniki* 2nd ed. (Moscow: Nauka, 1976)
294. Froese Fischer C *The Hartree–Fock Method for Atoms: A Numerical Approach* (New York: Wiley, 1977)
295. Miller M C, Neuhauser D *Mon. Not. R. Astron. Soc.* **253** 107 (1991)
296. Engel D, Klews M, Wunner G *Comput. Phys. Commun.* **180** 302 (2009)
297. Medin Z, Lai D, Potekhin A Y *Mon. Not. R. Astron. Soc.* **383** 161 (2008)
298. Ivanov M V *Opt. Spectrosc.* **70** 148 (1991); *Opt. Spektosk.* **70** 259 (1991); *J. Phys. B At. Mol. Opt. Phys.* **27** 4513 (1994)
299. Ivanov M V, Schmelcher P *Phys. Rev. A* **61** 022505 (2000)
300. Schimeczek C, Engel D, Wunner G *Comput. Phys. Commun.* **183** 1502 (2012)
301. Mori K, Hailey C J *Astrophys. J.* **564** 914 (2002)
302. Schmelcher P, Detmer T, Cederbaum L S *Phys. Rev. A* **64** 023410 (2001)
303. Lai D *Rev. Mod. Phys.* **73** 629 (2001)
304. Detmer T, Schmelcher P, Cederbaum L S *Phys. Rev. A* **57** 1767 (1998)
305. Kubo A *J. Phys. Chem. A* **111** 5572 (2007)
306. Kappes U, Schmelcher P *Phys. Rev. A* **53** 3869 (1996)
307. Khersonskii V K *Sov. Astron.* **31** 646 (1987); *Astron. Zh.* **64** 1233 (1987)
308. Mori K, Heyl J *Mon. Not. R. Astron. Soc.* **376** 895 (2007)
309. Turbiner A V *Astrophys. Space Sci.* **308** 267 (2007)
310. Turbiner A V, López Vieyra J C, Guevara N L *Phys. Rev. A* **81** 042503 (2010)
311. Medin Z, Lai D *Phys. Rev. A* **74** 062507 (2006)
312. Lindgren K A U, Virtamo J T *J. Phys. B At. Mol. Phys.* **12** 3465 (1979)
313. Chen Z, Goldman S P *Phys. Rev. A* **45** 1722 (1992)
314. Nakashima H, Nakatsuji H *Astrophys. J.* **725** 528 (2010)
315. Heisenberg W, Euler H *Z. Phys.* **98** 714 (1936)
316. Schubert C *Nucl. Phys. B* **585** 407 (2000)
317. Shabad A E, Usov V V *Phys. Rev. Lett.* **98** 180403 (2007)
318. Shabad A E, Usov V V *Phys. Rev. D* **77** 025001 (2008)
319. Machet B, Vysotsky M I *Phys. Rev. D* **83** 025022 (2011)
320. Al-Hujaj O-A, Schmelcher P *Phys. Rev. A* **67** 023403 (2003)
321. Johnson B R, Hirschfelder J O, Yang K-H *Rev. Mod. Phys.* **55** 109 (1983)
322. Baye D, Vincke M *Phys. Rev. A* **42** 391 (1990)
323. Gor'kov L P, Dzyaloshinskii I E *Sov. Phys. JETP* **26** 449 (1968); *Zh. Eksp. Teor. Fiz.* **53** 717 (1967)
324. Burkova L A et al. *Sov. Phys. JETP* **44** 276 (1976); *Zh. Eksp. Teor. Fiz.* **71** 526 (1976)
325. Ipatova I P, Maslov A Yu, Subashiev A V *Sov. Phys. JETP* **60** 1037 (1984); *Zh. Eksp. Teor. Fiz.* **87** 1804 (1984)
326. Vincke M, Le Dourneuf M, Baye D *J. Phys. B At. Mol. Opt. Phys.* **25** 2787 (1992)
327. Potekhin A Y *J. Phys. B At. Mol. Opt. Phys.* **27** 1073 (1994)
328. Vincke M, Baye D *J. Phys. B At. Mol. Opt. Phys.* **21** 2407 (1988)
329. Pavlov G G, Mészáros P *Astrophys. J.* **416** 752 (1993)
330. Bezchastnov V G, Pavlov G G, Ventura J *Phys. Rev. A* **58** 180 (1998)
331. Pavlov G G, Bezchastnov V G *Astrophys. J.* **635** L61 (2005)
332. Däppen W *Rev. Mexicana Astron. Astrofis.* **23** 141 (1992)
333. Rogers F J *Phys. Plasmas* **7** 51 (2000)
334. Rogers F J, Swenson F J, Iglesias C A *Astrophys. J.* **456** 902 (1996)
335. Landau L D, Lifshitz E M *Statistical Physics* Pt. 1 (Oxford: Butterworth-Heinemann, 1980); Translated from Russian: *Statisticheskaya Fizika* Pt. 1 (Moscow: Nauka, 1976)
336. Van Leeuwen H-J *J. Physique Radium VI* **2** 361 (1921)
337. Fermi E *Z. Phys.* **26** 54 (1924)
338. Khersonskii V K *Sov. Astron.* **31** 225 (1987); *Astron. Zh.* **64** 433 (1987)
339. Rajagopal M, Romani R, Miller M C *Astrophys. J.* **479** 347 (1997)
340. Hummer D G, Mihalas D *Astrophys. J.* **331** 794 (1988)
341. Inglis D R, Teller E *Astrophys. J.* **90** 439 (1939)
342. Ecker G, Kröll W *Phys. Fluids* **6** 62 (1963)
343. Rogers F J *Astrophys. J.* **310** 723 (1986)
344. Stehlé C, Jacquemot S *Astron. Astrophys.* **271** 348 (1993)
345. Potekhin A Y *Phys. Plasmas* **3** 4156 (1996)
346. Miller M C *Mon. Not. R. Astron. Soc.* **255** 129 (1992)
347. Mori K, Hailey C J *Astrophys. J.* **648** 1139 (2006)
348. Mori K, Ho W C G *Mon. Not. R. Astron. Soc.* **377** 905 (2007)
349. Potekhin A Y, Chabrier G, Shibanov Yu A *Phys. Rev. E* **60** 2193 (1999); *Phys. Rev. E* **63** 019901 (2000), Erratum
350. Potekhin A Y, Chabrier G *Astrophys. J.* **600** 317 (2004)
351. Callen J D *Fundamentals of Plasma Physics* (Madison: Univ. of Wisconsin, 2006); http://homepages.cae.wisc.edu/~callen/book.html
352. Ruderman M *Phys. Rev. Lett.* **27** 1306 (1971)
353. Medin Z, Lai D *Phys. Rev. A* **74** 062508 (2006)
354. Ebeling W, Norman G *J. Stat. Phys.* **110** 861 (2003)
355. Salpeter E E *Astrophys. J.* **134** 669 (1961)
356. Rögnvaldsson Ö E et al. *Astrophys. J.* **416** 276 (1993)
357. Thorolfsson A et al. *Astrophys. J.* **502** 847 (1998)
358. Lai D, Salpeter E E *Astrophys. J.* **491** 270 (1997)
359. Medin Z, Lai D *Mon. Not. R. Astron. Soc.* **382** 1833 (2007)
360. Gnedin Yu N, Pavlov G G *Sov. Phys. JETP* **38** 903 (1974); *Zh. Eksp. Teor. Fiz.* **65** 1806 (1973)
361. Nagel W *Astrophys. J.* **236** 904 (1980)
362. Shibanov Yu A, Zavlin V E *Astron. Lett.* **21** 3 (1995); *Pis'ma Astron. Zh.* **21** 5 (1995)
363. Bulik T, Pavlov G G *Astrophys. J.* **469** 373 (1996)
364. Potekhin A Y et al. *Astrophys. J.* **612** 1034 (2004)
365. Novick R et al. *Astrophys. J.* **215** L117 (1977)
366. Gnedin Yu N, Pavlov G G, Shibanov Yu A *Sov. Astron. Lett.* **4** 117 (1978); *Pis'ma Astron. Zh.* **4** 214 (1978)
367. Pavlov G G, Gnedin Yu N *Sov. Sci. Rev. E Astrophys. Space Phys.* **3** 197 (1984)
368. Adler S L *Ann. Physics* **67** 599 (1971)
369. Heyl J S, Hernquist L *Phys. Rev. D* **55** 2449 (1997)
370. Kohri K, Yamada S *Phys. Rev. D* **65** 043006 (2002)
371. Shaviv N J, Heyl J S, Lithwick Y *Mon. Not. R. Astron. Soc.* **306** 333 (1999)
372. Heyl J S, Shaviv N J *Phys. Rev. D* **66** 023002 (2002)
373. Van Adelsberg M, Perna R *Mon. Not. R. Astron. Soc.* **399** 1523 (2009)
374. Shafranov V D, in *Reviews of Plasma Physics* Vol. 3 (Ed. M A Leontovich) (New York: Consultants Bureau, 1967) p. 1; Translated from Russian: *Voprosy Teorii Plazmy* Iss. 3 (Ed. M A Leontovich) (Moscow: Gosatomizdat, 1963) p. 3
375. Ho W C G, Lai D *Mon. Not. R. Astron. Soc.* **338** 233 (2003)
376. Shibanov Yu A et al. *Astron. Astrophys.* **266** 313 (1992)
377. Zavlin V E et al. *Astron. Astrophys.* **297** 441 (1995)
378. Van Adelsberg M, Lai D *Mon. Not. R. Astron. Soc.* **373** 1495 (2006)
379. Zane S et al. *Astrophys. J.* **560** 384 (2001)
380. Lai D, Ho W C G *Astrophys. J.* **566** 373 (2002)

381. Ho W C G, Potekhin A Y, Chabrier G *Astrophys. J. Suppl.* **178** 102 (2008)
382. Ho W C G, in *Magnetic Fields Throughout Stellar Evolution* (Proc. IAU Symp. 302, Eds M Jardine, P Petit, H C Spruit) (Cambridge: Cambridge Univ. Press, 2014); arXiv:1311.5583
383. Itoh N *Mon. Not. R. Astron. Soc.* **173** 1P (1975)
384. Lenzen R, Trümper J *Nature* **271** 216 (1978)
385. Brinkmann W *Astron. Astrophys.* **82** 352 (1980)
386. Van Adelsberg M et al. *Astrophys. J.* **628** 902 (2005)
387. Pérez-Azorin J F, Miralles J A, Pons J A *Mon. Not. R. Astron. Soc.* **433** 275 (2005)
388. Potekhin A Y et al. *Astron. Astrophys.* **546** A121 (2012)
389. Motch C, Zavlin V E, Haberl F *Astron. Astrophys.* **408** 323 (2003)
390. Ho W C G et al. *Mon. Not. R. Astron. Soc.* **375** 821 (2007)
391. Suleimanov V, Potekhin A Y, Werner K *Astron. Astrophys.* **500** 891 (2009)
392. Suleimanov V et al. *Astron. Astrophys.* **522** A111 (2010)
393. Chang P, Bildsten L *Astrophys. J.* **605** 830 (2004)
394. Ho W C G *Mon. Not. R. Astron. Soc.* **380** 71 (2007)
395. Kaplan D L, Van Kerkwijk M H, Anderson J *Astrophys. J.* **571** 447 (2002)
396. Walter F M, Lattimer J M *Astrophys. J.* **576** L145 (2002)
397. Van Kerkwijk M H, Kaplan D L *Astrophys. Space Sci.* **308** 191 (2007)
398. Kaplan D L, Van Kerkwijk M H, Anderson J *Astrophys. J.* **660** 1428 (2007)
399. Walter F M et al. *Astrophys. J.* **724** 669 (2010)
400. Van Kerkwijk M H, Kaplan D L *Astrophys. J.* **673** L163 (2008)
401. Hambaryan V et al. *Astron. Astrophys.* **534** A74 (2011)